

THESIS

A NEW ALGORITHM FOR RETRIEVAL OF TROPOSPHERIC WET PATH DELAY OVER
INLAND WATER BODIES AND COASTAL ZONES USING BRIGHTNESS
TEMPERATURE DEFLECTION RATIOS

Submitted by

Kyle L. Gilliam

Department of Electrical and Computer Engineering

In partial fulfillment of the requirements

For the Degree of Master of Science

Colorado State University

Fort Collins, Colorado

Spring 2013

Master's Committee:

Advisor: Steven C. Reising

Branislav Notaros

Christian Kummerow

Copyright by Kyle L. Gilliam 2013

All Rights Reserved

ABSTRACT

A NEW ALGORITHM FOR RETRIEVAL OF TROPOSPHERIC WET PATH DELAY OVER INLAND WATER BODIES AND COASTAL ZONES USING BRIGHTNESS TEMPERATURE DEFLECTION RATIOS

As part of former and current sea-surface altimetry missions, brightness temperatures measured by nadir-viewing 18-34 GHz microwave radiometers are used to determine apparent path delay due to variations in index of refraction caused by changes in the humidity of the troposphere. This tropospheric wet-path delay can be retrieved from these measurements with sufficient accuracy over open oceans. However, in coastal zones and over inland water the highly variable radiometric emission from land surfaces at microwave frequencies has prevented accurate retrieval of wet-path delay using conventional algorithms. To extend wet path delay corrections into the coastal zone (within 25 km of land) and to inland water bodies, a new method is proposed to correct for tropospheric wet-path delay by using higher-frequency radiometer channels from approximately 50-170 GHz to provide sufficiently small fields of view on the surface. A new approach is introduced based on the variability of observations in several millimeter-wave radiometer channels on small spatial scales due to surface emissivity in contrast to the larger-scale variability in atmospheric absorption. The new technique is based on the measurement of deflection ratios among several radiometric bands to estimate the transmissivity of the atmosphere due to water vapor. To this end, the Brightness Temperature Deflection Ratio (BTDR) method is developed starting from a radiative transfer model for a downward-looking microwave radiometer, and is extended to pairs of frequency channels to retrieve the wet path delay. Then a mapping between the wet transmissivity and wet-path delay is performed using atmospheric absorption models. A frequency selection study is presented to determine the suitability of frequency sets for accurate retrieval of tropospheric wet-path delay, and comparisons are made to frequency sets based on currently-available microwave radiometers.

Statistical noise analysis results are presented for a number of frequency sets. Additionally, this thesis demonstrates a method of identifying contrasting surface pixels using edge detection algorithms to identify contrasting scenes in brightness temperature images for retrieval with the BTDR method. Finally, retrievals are demonstrated from brightness temperatures measured by Special Sensor Microwave Imager/Sounder (SSMIS) instruments on three satellites for coastal and inland water scenes. For validation, these retrievals are qualitatively compared to independently-derived total precipitable water products from SSMIS, the Tropical Rainfall Measurement Mission (TRMM) Microwave Imager (TMI) and the Advanced Microwave Sounding Radiometer for Earth Observing System (EOS) (AMSR-E). Finally, a quantitative method for analyzing the data consistency of the retrieval is presented as an estimate of the error in the retrieved wet path delay. From these comparisons, one can see that the BTDR method shows promise for retrieving wet path delays over inland water and coastal regions. Finally, several additional future uses for the algorithm are described.

ACKNOWLEDGEMENTS

I would first like to thank Prof. Steven C. Reising for his guidance and support as my advisor for this project. Additionally, I would like to thank Dr. Xavier Bosch-Lluis for his technical expertise in the field of remote sensing. Furthermore, I would like to thank Dr. Alan Tanner from the Jet Propulsion Laboratory for developing the initial concepts of the Brightness Temperature Deflection Ratio Algorithm as well as providing his expertise in the area.

I would like to thank the team at NASA's Jet Propulsion Laboratory for their cooperation and guidance as well as their insightful commentary provided on the work described in this Master's thesis. Of the team, I would specifically like to thank Dr. Shannon Brown for providing guidance on retrieval algorithms.

I would like to thank the Precipitation Research Group at Colorado State University for their cooperation in providing independently-derived total precipitable water products for comparison with the retrievals presented in this thesis. In particular, I would like to thank Prof. Christian Kummerow, Dr. Wes Berg, Ms. Janice Bytheway, and Dr. Nereida Rodriguez-Alvarez for their willingness to help and provide data acquisition and answers to questions concerning their products.

Additionally, I would like to thank the other current and former students in the Microwave Systems Laboratory for their help and support with this work. Specifically, they are Alexander Lee, Swaroop Sahoo, Darrin Albers, Scott Nelson, Thaddeus Johnson, and Torie Hadel. Furthermore, I would like to thank Joseph Hardin for his statistical and mathematical advice.

Finally, thanks are due to my friends and family for their patience and support.

TABLE OF CONTENTS

Chapter 1: Background Information	1
1.1: Scientific Motivation.....	1
1.2: Planck Blackbody Radiation and Brightness Temperature.....	3
1.3: Radiative Transfer Theory	8
1.4: Brightness Temperatures as Measured by Downward Looking Radiometers	11
1.5: Microwave and Millimeter-wave Radiometry	15
1.6. Existing Coastal Retrieval Algorithms.....	18
Chapter 2: Brightness Temperature Deflection Ratio Algorithm	20
2.1 Theoretical Introduction to BTDR Algorithm	20
2.2 Atmospheric Absorption Models	26
2.3 Edge Detection Algorithms	28
2.4 Software Implementation	31
Chapter 3: Wet Path Delay Retrieval: Simulation Results	36
3.1: Determining the Number of Contributing Channels.....	36
3.2: Frequency Channel Selection.....	45
3.3: Stability and Sensitivity Analysis	47
3.4: General Noise Analysis.....	52
3.5: Radiometer Noise Analysis.....	59
Chapter 4: Wet Path Delay Retrieval: Results from Measured Data.....	64
4.1: Sources of Retrieval Noise.....	64

4.2: HAMSR Retrieval Results	67
4.3: SSMIS Retrieval Results.....	73
4.3.1: Inland Water Retrievals.....	79
4.3.2: Coastal Retrievals.....	81
4.4 Error Analysis	85
4.4.1: Data Consistency Analysis Method.....	85
4.4.2: Analysis of Individual Coastlines of SSMIS Derived Wet Path Delays	89
4.4.3: Analysis of Aggregate SSMIS Derived Wet Path Delay Retrievals	93
Chapter 5: Closing Remarks	97
5.1: Summary	97
5.2: Conclusions	99
5.3: Future Work	100
REFERENCES	108
LIST OF ABBREVIATIONS.....	113

LIST OF TABLES

Table 2-1: Description of input parameters used to perform simulated wet path delay retrievals	34
Table 3-1: Description of simulation parameters for BTDR initialization	37
Table 3-2: Description of the 5 simulated atmospheres used to determine the relationships of the eigenvalues of the brightness temperature differences and the brightness temperature deflection ratios. The analysis of these cases is shown in Fig. 4 and 5.	43
Table 4-1: Description of the frequency channels available from the HAMSR instrument from [23]. The W_1 and W_2 entries are weighting factors for the lower and upper sidebands, respectively.	68
Table 4-2: Comparison of the BTDR retrievals using HAMSR measured brightness temperatures and the converted total precipitable water predictions from NOAA NOMADS	72
Table 4-3: Description of the frequency channels on the SSMIS instrument from [24].	74
Table 4-4: Comparison of the time of measurement, with a resolution of 5 minutes, in UTC for each of the 3 instruments used for different areas on January 1, 2011	78

LIST OF FIGURES

<p>Fig. 1-1: Spectral brightness on a logarithmic plot for a frequency range of 10 MHz to 1000 THz according to the Planck law for spectral brightness at (a) four different absolute temperatures with varying frequency and (b) five frequencies in the microwave and millimeter-wave regions with varying temperature. These frequency regions are shown between the black vertical markers at 0 and 2.5 on the log scale in part (a).</p>	5
<p>Fig. 1-2: Illustration of a small cylindrical volume in space</p>	8
<p>Fig. 1-3: Comparison of various opacities for both oxygen and water vapor (given with units of cm wet path delay).</p>	12
<p>Fig. 1-4: Radiative transfer model for a downward-looking radiometer</p>	14
<p>Fig. 1-5: System diagram of a total power radiometer</p>	15
<p>Fig. 1-6: System diagram of a Dicke radiometer</p>	16
<p>Fig. 1-7: System diagram of a noise-injection radiometer.....</p>	18
<p>Fig. 2-1: Histogram of possible z values based on the definition of z from Eq. 2-4, assuming no frequency dependence.....</p>	24
<p>Fig. 2-2: Illustration of the concept of an edge using (a) black and white and (b) grey scaled pixels.....</p>	29
<p>Fig. 2-3: (a) Original image and (b) Sobel gradient detected edges of original image.....</p>	30
<p>Fig. 2-4: (a) Original image and (b) Canny gradient detected edges of original image</p>	31
<p>Fig. 2-5: Data flow diagram of the main portion of the code</p>	32
<p>Fig. 3-1: Comparison of the normalized eigenvalues, denoted by λ, for antenna scene temperatures. The * in the figures corresponds to the frequency channel that is allowed to change and is represented by the x-axis. The atmosphere and surface parameters for these simulations are as follows: $T_m = 290$ K, $T_n = 285$ K, $e_m = 0.95$, $T_{atm} = 277.26$ K, and e_n taking values based upon the water emissivity model from [17]......</p>	38

Fig. 3-2: Comparison of the eigenvalues, denoted by λ , of simulated deflection ratios. The * in the title of each figure corresponds to the frequency channel that is allowed to change and is represented by the x-axis. The atmosphere and surface parameters for these simulations are as follows: $T_m = 290$ K, $T_n = 285$ K, $e_m = 0.95$, $T_{atm} = 277.26$ K, and e_n taking values based upon the water emissivity model from [17]..... 41

Fig. 3-3: Comparison of the eigenvalues of a) the brightness temperature differences and b) the deflection ratios of the 70, 90, 130 GHz frequency set for the 5 atmospheres shown in Table 3-2. 43

Fig. 3-4: Comparison of the eigenvalues of a) the brightness temperature differences and b) the deflection ratios of the 52.8, 91.665, 150 GHz frequency set for the 5 atmospheres shown in Table 3-2. 44

Fig. 3-6: Diagram of frequency selection criteria for 0.01 cm simulated retrieval error..... 47

Fig. 3-7: 52.8 91.655 150 GHz cost function contours with constant simulation parameters $T_m=285$ K, and e_m is frequency dependent and calculated using [17], where the actual transmissivity for each case is $Y_{Wf_1}=0.9597$. The parameters which vary are: (a) $T_n=290$ K, $e_n=0.95$, $T_{atm}=277.27$ K, (b) $T_n=290$ K, $e_n=0.95$, $T_{atm}=277.27$ K (c) $T_n=270$ K, $e_n=0.95$, $T_{atm}=260$ K (d) $T_n=290$ K, $e_n=0.85$, $T_{atm}=277.27$ K..... 49

Fig. 3-8: Cost function contours for a) 50, 52, and 113 GHz, b) 79, 150, and 167 GHz, c) 47, 126, and 153 GHz, and d) 52, 128, and 168 GHz with simulation parameters $T_m=285$ K, $T_n=290$ K, $e_n=0.95$, $T_{atm}=277.27$ K. The water emissivity, e_m , is based on the frequency dependent model from [17] and values are not shown. The simulated transmissivity values for the contours are a) $Y_{Wf_1}=0.96333$, b) $Y_{Wf_1} = 0.91568$, c) $Y_{Wf_1}=0.9669$, and $Y_{Wf_1}=0.96207$. The difference in simulated transmissivity values is due different frequency channel choices for f_1 51

Fig. 3-9: Histograms of wet path delay error assuming $\sigma_{noise} = 0.1$ K for the a) 70, 90, and 130 GHz, b) 50, 52, and 113 GHz; c) 52.8, 91.665, and 150 GHz; and d) 52, 128, and 168 GHz sets. 54

Fig. 3-10: Histograms of wet path delay error assuming $\sigma_{noise} = 0.5$ K for the a) 70, 90, and 130 GHz; b) 50, 52, and 113 GHz; c) 52.8, 91.665, and 150 GHz; and d) 52, 128, and 168 GHz frequency set. 55

Fig. 3-11: Comparison of the a) retrieval bias and b) retrieval uncertainty for the 70, 90, and 130 GHz; 50, 52, and 113 GHz; 52.8, 91.665, and 150 GHz; and 52, 128, and 168 GHz sets with $\sigma_{noise} = 0.1$ K with respect to the actual wet path delay for the simulated atmosphere..... 57

Fig. 3-12: Comparison of the a) retrieval bias and b) retrieval uncertainty for the 70, 90, and 130 GHz; 50, 52, and 113 GHz; 52.8, 91.665, and 150 GHz; and 52, 128, and 168 GHz sets with $\sigma_{noise} = 0.5$ K with respect to the actual wet path delay for the simulated atmosphere..... 58

Fig. 3-13: Radiometric resolution with respect to bandwidth for $T_{sys}=2000$ K and $t=0.02$ s..... 60

Fig. 3-14: Comparison of the mean squared error of both the mean and standard deviation of the retrieval error for the 70, 90, and 130 and 50, 52, 113 and GHz sets 61

Fig. 3-15: Comparison of HAMSR and SSMIS retrievals using the BTDR method. The frequency set used for HAMSR was 50, 52, and 113 GHz and the set for SSMIS was 52.8, 91.655, and 150 GHz. The measurement bias can be seen in (a) and the measurement uncertainty in (b)..... 62

Fig. 4-1: Illustration of image processing errors due to detection of edges. The boundary for the water (shown by A) and the land (shown by B) is blurred due to the high concentration of water vapor in the atmosphere. 65

Fig. 4-2: Illustration of image processing errors due to grid and coastline alignment. In this image, if the retrieval is taken along the line labeled A, the assumptions of the land/water pixels mentioned in Chapter 2 is violated. If the retrieval is taken along the line labeled B, the assumptions of the model are valid and a retrieval can be performed..... 66

Fig. 4-3: Illustration of the ground track of HAMSR aboard the NASA Global Hawk unmanned aircraft over the Saint John’s River. 69

Fig. 4-4: Brightness temperature measurements taken by HAMSR over the St. John’s River in Florida for September 1, 2010. 70

Fig. 4-5: Map of NOMADS predicted total precipitable water values for September 1, 2010; the date of the HAMSR based BTDR retrievals..... 71

Fig. 4-6: Illustration of (a) horizontally retrieved pixels, (b) vertically retrieved pixels, and (c) the combination of the horizontal and vertical pixels..... 76

Fig. 4-7: Comparison of BTDR method wet path delay retrievals (shown along the shorelines of the Caspian and Aral Seas) to wet path delays derived from total precipitable water (shown in water) retrieved from (b) TMI, (c) AMSR-E, (d) SSMIS. The general area of the retrieval is shown in (a)..... 80

Fig. 4-8: Comparison of BTDR method wet path delay retrievals (shown along the shorelines of the Arabian Sea) to wet path delays derived from total precipitable water (shown in open water) retrieved from (b) TMI, (c) AMSR-E, (d) SSMIS. The general area of the retrieval is shown in (a). 82

Fig. 4-9 Comparison of BTDR method wet path delay retrievals (shown along the shorelines of the Chile and Argentina) to wet path delays derived from total precipitable water (shown in open water) retrieved from (b) TMI, (c) AMSR-E, (d) SSMIS. The general area of the retrieval is shown in (a)..... 84

Fig. 4-10: Diagram showing the spatial frequency analysis concept for performing data consistency analysis on the coastlines identified using the BTDR retrieval algorithm. The ω axis is given in radians. 86

Fig. 4-11: Image showing retrieval noise with respect to cutoff frequency for several coastlines. 87

Fig. 4-12: Effect of cutoff frequency choice on mean retrieval uncertainty for the coastlines examined in Fig. 4-11 88

Fig. 4-13: Shown in (a) is a map showing three land water boundaries for which the retrieval consistency analysis was performed for the Caspian Sea Region. Data series of the coastlines are shown in (b), (c), and (d) and indicated on the map in (a)..... 90

Fig. 4-14: Shown in (a) is a map showing three land water boundaries for which the retrieval consistency analysis was performed for the Arabian Sea Region. Data series of the coastlines are shown in (b), (c), and (d) and indicated on the map in (a)..... 92

Fig. 4-15: Comparison of the RMS error of the retrievals with respect to the retrieval locations 93

Fig. 4-16: Aggregate plot of the RMS error of the wet path delay for all identified coast and shorelines for the 3 SSMIS data sets of the F16, F17, and F18 satellites with respect to the wet path delay range of each coast/shoreline. 94

Fig. 4-17: Aggregate plot of the RMS error of the wet path delay for all identified coasts and shorelines for the 3 SSMIS data sets of the F16, F17, and F18 satellites with respect to the length, in km, of each coast/shoreline..... 95

Fig. 5-1: Brightness temperature imagery for a portion of the Pacific Ocean measured by the 91.655 GHz SSMIS channel 103

Fig. 5-2: Retrieval results for a portion of the Pacific Ocean using (a) the BTDR method and (b) the GPROF 2010 algorithm. Shown in (c) is an overlay of the two retrievals for comparison.. 104

Fig. 5-3: Map of the (a) retrieved wet path delays using the BTDR algorithm and (b) geography of the retrieval area to aid in feature identification..... 106

Chapter 1: Background Information

In this section, scientific motivation and general background information for the work described in this thesis is given. After reviewing pertinent background material for retrieval of wet path delay, several types of radiometers and previous retrieval algorithms will be covered. Once a foundation has been built based on these concepts, the brightness temperature deflection ratio algorithm will be introduced and explained in detail.

1.1: Scientific Motivation

In this work, a method by which to discern the wet path delay over inland bodies of water and along coastlines is explained, developed, and tested. However, before explaining the algorithm it is useful to consider the context of the problem. Water vapor density, and in turn wet path delay, has been retrieved over open oceans for many years using observations from microwave radiometers on board earth observing satellites. Currently, retrieving water vapor products over the open oceans is a reasonably well understood problem. One reason for measuring atmospheric water vapor and the main purpose for development of the new algorithm presented in this work is to retrieve the wet path delay as a correction for satellite altimeters that measure the surface height of Earth's bodies of water. The tropospheric wet-path delay is the error introduced into a propagating signal due to changes in index of refraction by the amount of water vapor present in the atmosphere. This change in refractive index is proportional to the density of water vapor in the atmosphere in a vertical column from the top of the atmosphere to the ground and causes changes in the refractive index of the medium. This relationship is shown in Eq. 1-1.

$$v = \frac{c}{n} \quad (1-1)$$

In Eq. 1-1, the velocity of light, v , is the ratio of the speed of light in a vacuum, c , to the refractive index of the medium, n . As a note, the refractive index is dependent upon the water

vapor present in the atmosphere as well as the atmospheric temperature, and pressure. In order to avoid complexity in the explanation, it is assumed that water vapor is the primary cause of change in the index of refraction. Increases in the refractive index decrease the speed of propagation of radar signals in the atmosphere. Specifically, for satellite altimeters and radar interferometers, this error causes the path between the satellite and the surface to appear longer than it actually is. This produces an error in the inferred surface height that needs to be corrected. Now that an explanation for the product of interest for this thesis, tropospheric wet path delay, has been established, one can continue to discuss the effects of wet path delay on the atmosphere and ways of estimating it.

One such instrument is the Ka-band Radar Interferometer (KaRIn) under development by NASA as part of the Surface Water and Ocean Topography (SWOT) mission. One main goal of the SWOT mission and one of the design objectives for KaRIn is to measure the surface height of inland water bodies, including rivers of width greater than 100 m [1, 2, 3]. Additionally, higher frequency (90-180 GHz) radiometers with improved radiometric resolution are being designed to provide path delay corrections for such altimeters [4]. To do this to with the precision required by the SWOT objectives, new algorithms are needed to retrieve the tropospheric wet path delay in the atmosphere and thereby provide a correction for the altimeter measurements.

In the past, such algorithms have been formulated that depend on prior, or *a priori*, information. Specifically, for coastal areas, algorithms based on open-ocean retrieval techniques have been developed by adapting the algorithm to account for mixed land-water emissivity pixels [5]. Another method is to correct the measured brightness temperatures from satellite microwave radiometers and apply an open-ocean retrieval algorithm [6]. In contrast, retrieval of wet-path delay over inland water is a relatively new endeavor, so there are comparatively fewer studies of this topic. One of these takes the approach of modeling land emissivities, which are typically much more variable than those of open oceans, in an attempt to provide a basis for wet path

delay retrievals over land [7]. In contrast to [7], which attempts to retrieve wet path delay over all land, the algorithm presented in this thesis is intended to retrieve wet path delay over inland water.

In contrast to prior retrieval algorithms, the Brightness Temperature Deflection Ratio (BTDR) algorithm requires no *a priori* information and is therefore not as sensitive to the statistical properties of the atmosphere. This algorithm is based on detecting contrast between background scenes, i.e. surfaces, from downward-viewing microwave radiometers. Additionally, there is no assumption of which instrument the algorithm is designed for since it can be used with any satellite or airborne microwave radiometer as long as the frequency channels of the instrument meet a number of conditions, which will be discussed. To start the discussion, first one needs to consider the background material on which the BTDR method retrievals are based.

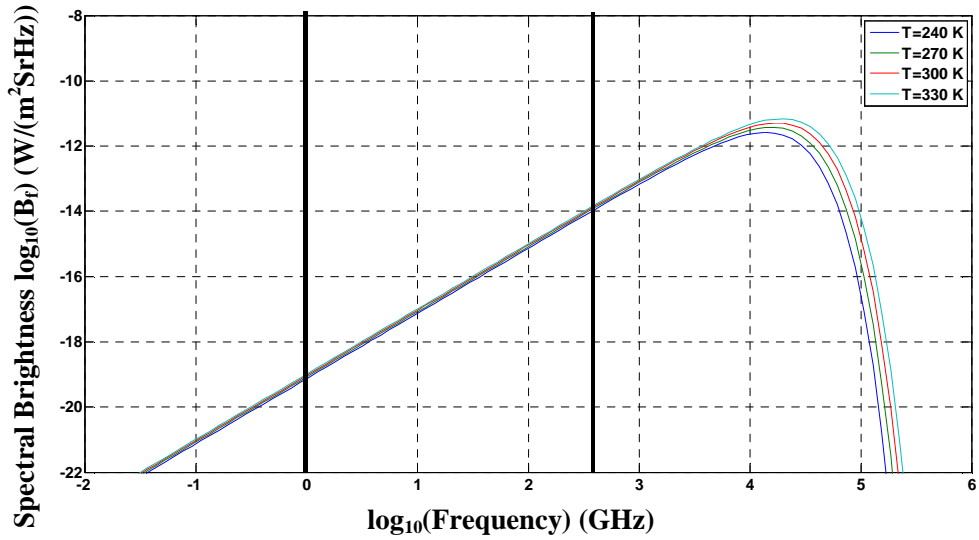
1.2: Planck Blackbody Radiation and Brightness Temperature

Before quantifying radiation from the atmosphere, it is useful to consider the underlying theory and causes of such radiation. By definition, a perfect absorber is an object that absorbs all incident electromagnetic radiation. Due to conservation of energy, for an object to remain in thermal equilibrium it must emit the same amount of energy as it absorbs. From this, we can quantify the thermal radiation, i.e. the electromagnetic radiation generated by thermal energy of the molecules, by using Planck's Law [8] as in Eq. 1-2.

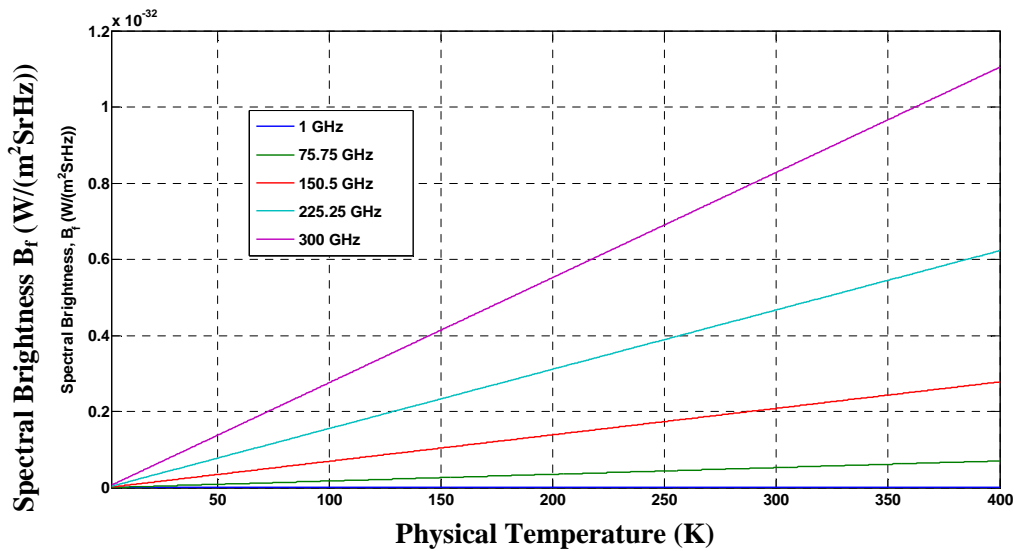
$$B_f = \frac{2hf^3}{c^2} \left[\frac{1}{e^{\frac{hf}{kT}} - 1} \right] \quad (1-2)$$

This relationship quantifies the spectral brightness of the object, B_f , with units $W/(m^2SrHz)$, in terms of Planck's constant, $h = 6.626 \times 10^{-34}$ J · s, Boltzmann's constant, $k = 1.381 \times 10^{-23}$ J/K, absolute temperature T , in K, and the speed of light, c in m/s. Through dimensional analysis of Planck's Law, one may not that the units for spectral brightness seem to be W/m^2 . The reason that the units of $W/(m^2SrHz)$ are used is because in the derivation of Planck's law,

the source of the spectral brightness is assumed constant with respect to a unit frequency and solid angle, as further explored in [8]. This relationship is shown as a function of atmospheric temperatures in Fig. 1-1(a) and for various microwave and millimeter-wave frequencies in Fig. 1-1(b).



(a)



(b)

Fig. 1-1: Spectral brightness on a logarithmic plot for a frequency range of 10 MHz to 1000 THz according to the Planck law for spectral brightness at (a) four different absolute temperatures with varying frequency and (b) five frequencies in the microwave and millimeter-wave regions with varying temperature. These frequency regions are shown between the black vertical markers at 0 and 2.5 on the log scale in part (a).

One should note that in the microwave and millimeter wave regions from approximately 1 to 300 GHz in Fig. 1-1, spectral brightness has an approximately linear relationship with frequency, as

in (a), and physical temperature, as in (b). Specifically, this approximation is valid when the exponential term of Eq. 1-2 is very small and meets the condition in Eq. 1-3.

$$\frac{hf}{kT} \ll 1 \quad (1-3)$$

In this case, one can apply the first order Taylor approximation shown in Eq. 1-4.

$$e^{\frac{hf}{kT}} - 1 \cong \frac{hf}{kT} \quad (1-4)$$

After this approximation, one can rewrite Eq. 1-2 in a simplified form known as Rayleigh-Jeans' law [8] for spectral brightness, as shown in Eq. 1-5.

$$B_f = \frac{2kT}{\lambda^2} \quad (1-5)$$

In this equation, λ represents the wavelength in m, meters. From this point, we will assume Eq. 1-5 as the definition for spectral brightness that will be used in the following derivations. The error introduced by using the Raleigh-Jeans law instead of Planck's Law at 300 K is approximately 0.008% at 1 GHz and scales linearly to approximately 2.4% at 300 GHz. Specifically, this approximation is useful for quantifying the radiated power of a blackbody and relating it to an equivalent brightness temperature. To do this, the term "blackbody radiator" needs to be defined. A blackbody radiator is an idealized, perfectly opaque material which absorbs all incident radiation and reflects none [8]. Such an object radiates uniformly in all directions according to Eq. 1-2 and is closely modeled at microwave and millimeter wave frequencies by Eq. 1-5. The power radiated by this object is shown in Eq. 1-6.

$$P_{bb} = kTB_W \frac{A_r}{\lambda^2} \iint_{4\pi} F_n(\Theta, \Phi) d\Omega \quad (1-6)$$

Eq. 1-6 shows that the power radiated by a blackbody is an integral of the normalized antenna pattern, $F_n(\Theta, \Phi)$, over solid angle $d\Omega$. The bandwidth of the received power is $B_W = \Delta f$. By

recognizing the integral as the antenna solid angle, one can simplify Eq. 1-6 to obtain a linear relationship between the physical temperature and the radiated power, as shown by Eq. 1-7.

$$P_{bb} = kTB_W \quad (1-7)$$

To account for the effects of non-blackbodies, the concept of emissivity is introduced in Eq. 1-8.

$$e = \frac{T_B}{T} \quad (1-8)$$

Using the emissivity, the power radiated by an object can be written as a function of its brightness temperature, T_B . Using Eq. 1-8, one can rewrite the power radiated by an object as a function of its brightness temperature. However, to account for antenna pattern effects, the antenna temperature is introduced as Eq. 1-9.

$$T_A = \frac{\iint_{4\pi} T_{AP}(\theta, \phi) F_n(\theta, \phi) d\Omega}{\iint_{4\pi} F_n(\theta, \phi) d\Omega} \quad (1-9)$$

This relationship shows that the antenna temperature, T_A , can be represented as a function of the apparent temperature distribution, T_{AP} , and again the normalized antenna pattern, F_n . As a note, the apparent temperature distribution is the blackbody-equivalent temperature distribution from the energy incident upon the antenna. This antenna temperature corresponds to the equivalent temperature measured by an antenna and is equal to the physical temperature of the object if the antenna is measuring a blackbody radiator. This relationship can be expanded and simplified by considering effects of the main lobe and side lobes of the antenna as well as its efficiency, as in Eq. 1-10.

$$T_A = \eta_m \bar{T}_{ML} + (1 - \eta_m) \bar{T}_{SL} \quad (1-10)$$

In this equation, η_m represents the main-beam efficiency of the antenna and in microwave radiometry is typically greater than 90%. Also, \bar{T}_{ML} represents the apparent temperature of the main-lobe, and \bar{T}_{SL} represents the apparent temperature of the side-lobes. Both \bar{T}_{ML} and \bar{T}_{SL} have similar definitions to Eq. 1-9. Now that a relationship for the antenna temperature as seen by the radiometric receiver has been established, one can continue and quantify the radiation from the atmosphere according to radiative transfer theory.

1.3: Radiative Transfer Theory

Before developing a model for the transfer of radiation in a medium, it is first useful to explain the concepts of extinction and emission. When radiation traversing a medium is reduced in intensity, this is referred to as extinction. Alternatively, if the intensity of the radiation increases when travelling through the medium, it is referred to as emission. With these concepts in mind, one can begin development of a radiative transfer model by first considering a small cylindrical volume with cross-sectional area dA and thickness dr , as shown in Fig. 1-2.

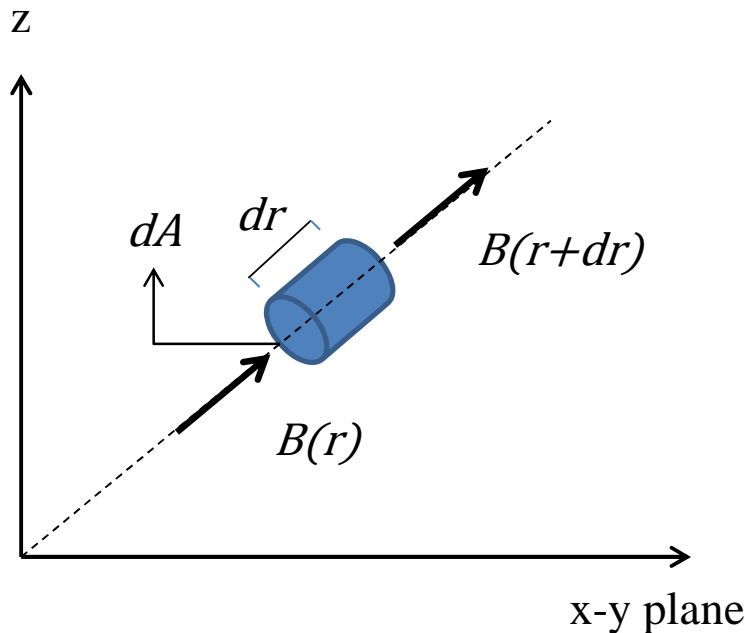


Fig. 1-2: Illustration of a small cylindrical volume in space

Losses in brightness due to extinction over the thickness, dr , can be quantified by Eq. 1-11.

$$dB(\text{extinction}) = \kappa_e B dr \quad (1-11)$$

In this equation, κ_e represents the extinction coefficient of the medium and has units of nepers/m. This coefficient quantifies the energy of the incident radiation lost due to absorption in the material. This energy is conserved in other forms such as heat and scattering. Scattered energy is energy which travels in some other direction than the direction of the incident radiation. As a result, the extinction coefficient can be written as a sum of two other coefficients; namely, κ_a , the absorption coefficient, and κ_s , the scattering coefficient. Analogous to the losses due to extinction, the increase in energy due to emission can be written as Eq. 1-12.

$$dB(\text{emission}) = (\kappa_a J_a + \kappa_s J_s) dr \quad (1-12)$$

In this case, the extinction coefficient has been expanded as the sum of the absorption and scattering coefficients. Each of these coefficients is multiplied by a source function, J_a and J_s , for the absorption and scattering cases, respectively. The change in brightness due to absorption and emission can be combined to form a differential equation with respect to a differential distance dr by combining the source terms into a single term, J , otherwise known as the effective total source function, as shown in Eq. 1-13.

$$dB = dB(\text{emission}) - dB(\text{extinction}) = \kappa_e dr (J - B) \quad (1-13)$$

From here, the differential equation can be further simplified by introducing the concept of optical depth, τ . This is done through the relationship shown in Eq. (1-14), where $d\tau$ is an increment of optical depth.

$$d\tau = \kappa_e dr \quad (1-14)$$

Combining Eq. 1-13 and 1-14 yields the equation of transfer with respect to the brightness, B , and effective total source function, J , shown in Eq. (1-15)

$$\frac{dB}{d\tau} + B = J \quad (1-15)$$

To facilitate the solution to Eq. 1-15, one can introduce the optical thickness, $\tau(r_1, r_2)$, along a path from r_1 to r_2 as seen in Eq. 1-16.

$$\tau(r_1, r_2) = \int_{r_1}^{r_2} \kappa_e dr \quad (1-16)$$

Using this, it is possible to obtain a solution to the radiative transfer equation by considering the transfer along the path from 0, corresponding to the ground, to a point r' and using Eq. 1-15 and 1-16 to obtain a differential equation of the form shown in Eq. 1-17.

$$\frac{dB(r')}{d\tau} e^{-\tau(0,r')} + B(r') e^{\tau(0,r')} = J(r') e^{\tau(0,r')} \quad (1-17)$$

After several simplifications and manipulations, one can arrive at the formal solution to the radiative transfer equation shown in Eq. 1-18.

$$B(r) = B(0) e^{-\tau(0,r)} + \int_0^r \kappa_e(r') J(r') e^{-\tau(r',r)} dr' \quad (1-18)$$

From this point, one can apply Raleigh-Jeans form of Planck's law to this solution to the radiative transfer equation, as shown in Eq. 1-19.

$$B(r) = \frac{2k}{\lambda^2} T_{AP}(r) B_W \quad (1-19)$$

Additionally, the source function, J , can be rewritten using a similar approach. Since the local thermal equilibrium is assumed, the thermal emission must equal the absorption. It is important to point out that these source functions represent an approximation since the atmosphere is constantly losing energy due to radiation. As such, the source function takes a form similar to $B(r)$ in Eq. 1-19.

Now, if one considers a scatter-free medium, the extinction coefficient reduces to only the absorption coefficient. This corresponds to conditions in which the sky is clear, for the microwave and millimeter wave regions, and should be considered a valid assumption in this situation. If clouds or rain are present, the validity of this assumption is dependent upon many factors, including the density, drop-size distribution, and size of the droplets relative to the electromagnetic wavelength. From this point, clouds and precipitation will not be considered in the formulation of the wet path delay retrieval algorithm in this work. With that said, the apparent temperature at a height r above the surface is given as Eq. 1-20.

$$T_{AP}(r) = T_{AP}(0)e^{-\tau(0,r)} + \int_0^r \kappa_a(r')T(r')e^{-\tau(r',r)}dr' \quad (1-20)$$

1.4: Brightness Temperatures as Measured by Downward Looking Radiometers

Now that the apparent temperature, T_{AP} , has been explained, one can further quantify the contributors to atmospheric radiation. In order to understand the sources of radiation received by an observing antenna, it is first useful to consider where they come from. Essentially, these contributors can be decomposed into two parts, upwelling and downwelling. Upwelling components are those which are energy travels from a point in the atmosphere upward toward the top of the atmosphere. Downwelling components are those in which energy is directed downward toward the surface.. However, before examining the various contributors, the concept of transmissivity should be introduced. The transmissivity of the atmosphere, is a dimensionless measure of how transmissive the atmosphere is, as shown in Eq. 1-21.

$$\Upsilon = e^{\tau(0,H) \sec \theta} \quad (1-21)$$

In this equation, θ represents the incidence angle of the radiometer antenna at the Earth's surface and the term $\tau(0,H)$ comes from Eq. 1-16. By excluding scattering from the problem, the

opacity, or optical thickness, can be rewritten as in terms of the atmospheric absorption coefficient, $\kappa_a(z)$, as Eq. 1-22.

$$\tau(0, H) = \int_0^H \kappa_a(z) dz \quad (1-22)$$

The absorption coefficient is typically calculated using semi-empirical models, such as the Rosenkranz or Van Vleck-Weisskopf models [9, 10]. The Rosenkranz model, which will be discussed in Chapter 2, is used for the calculations in this work. Additionally, opacities from the absorption coefficients given by the Rosenkranz model, are shown in Fig. 1-3.

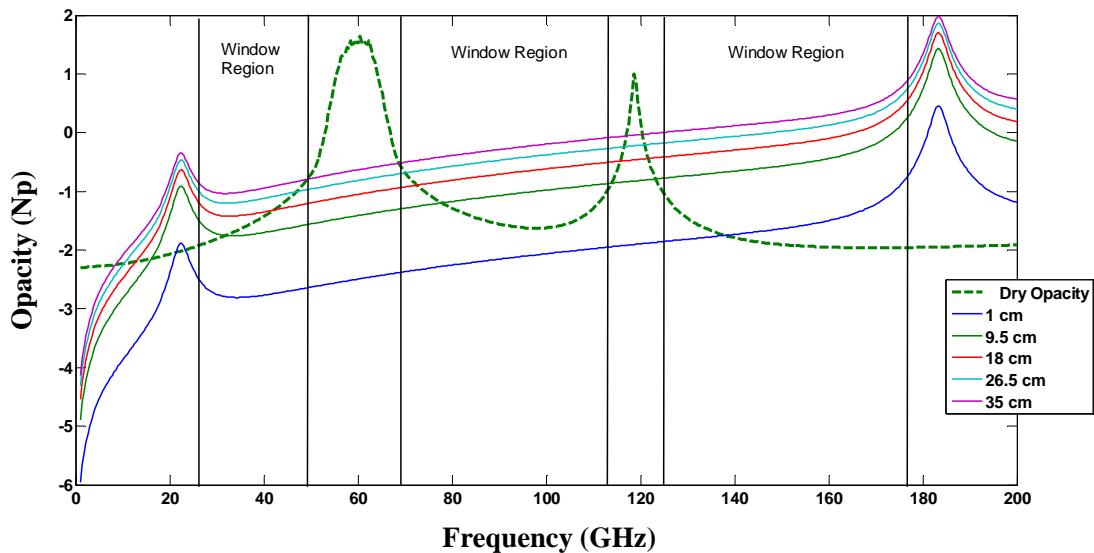


Fig. 1-3: Comparison of various opacities for both oxygen and water vapor (given with units of cm wet path delay).

In Fig. 1-3, frequency ranges with low opacity in the 20 to 200 GHz range are labeled window regions. The nomenclature comes from the fact that one can typically observe brightness temperatures due to both the atmosphere and the ground at these frequencies, whereas at the peaks, called sounding frequency ranges, only emission from the atmosphere is seen. The opacities shown in Fig. 1-3 have been decomposed into wet (water vapor) and dry (oxygen)

components. This decomposition is critical to the formation of the BTDR algorithm. Both the window regions and the opacity decomposition will be discussed in greater detail in Chapter 2.

To discuss radiative transfer in terms of a model atmosphere, one can first consider the properties of media which could be present in the atmosphere. To that end, the concepts of emissivity and transmissivity can be further explained by considering conservation of power when an incident wave travels from one medium into another by examining the power relationship in Eq. 1-23.

$$P_{inc} = P_{abs} + P_{refl} + P_{trans} \quad (1-23)$$

This relationship states that the incident power, P_{inc} , can be decomposed into the sum of the absorbed, reflected, and transmitted power [8] shown by P_{abs} , P_{refl} , and P_{trans} respectively. By taking ratios of the incident power to the absorbed, reflected, and transmitted power, one can arrive at Eq. 1-24.

$$1 = \alpha + \Gamma + Y \quad (1-24)$$

In this equation, it can be seen that the sum of the absorption, α , reflection, Γ , and transmissivity, Y , must be 1 according to the power relationship in Eq. 1-23. From here, three different types of media: opaque, lossless, and non-reflective/non-scattering, exhibit different relationships among these coefficients, as shown in Eq. 1-25 to 1-27, respectively.

$$Y = 0 \quad \Rightarrow \quad \Gamma = 1 - \alpha \quad (1-25)$$

$$\alpha = 0 \quad \Rightarrow \quad Y = 1 - \Gamma \quad (1-26)$$

$$\Gamma = 0 \quad \Rightarrow \quad e = 1 - Y \quad (1-27)$$

Now that a basis for the transmissivity and opacity concepts for different media has been established, one can begin to quantify the various upwelling and downwelling contributors to the antenna temperature observed by a radiometric receiver. Specifically, the two of interest for this work are opaque and non-reflective media. Shown in Fig. 1-4 is a diagram outlining these contributors assuming a downward looking radiometer.

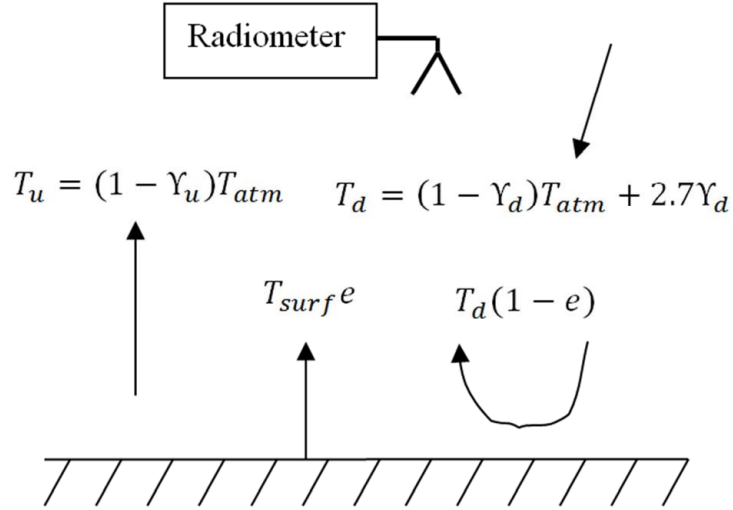


Fig. 1-4: Radiative transfer model for a downward-looking radiometer

Of the various components in Fig. 1-4, we will start with the emission from the atmosphere itself. This is quantified by the term $T_u = (1 - Y_u)T_{atm}$ where T_u represents the upwelling brightness temperature contribution from the atmosphere. This depends on the mean atmospheric temperature, T_{atm} , as well as the upwelling atmospheric transmissivity Y_u . The next component in Fig. 1-4 is the brightness temperature of the surface. This component is the product of the physical temperature of the surface, T_{surf} , and the surface emissivity e . For the downwelling components, we will begin with an analog to the upwelling atmospheric radiation. Similar to the upwelling atmospheric radiation, it is quantified by $T_d = (1 - Y_d)T_{atm} + 2.73Y_d$. In this component, the subscript d indicates that the brightness temperature and transmissivity are downwelling. Additionally, the emission from the cosmic background radiation appears as $2.73Y_d$. At the microwave and millimeter wave frequencies, this emission at the top of the atmosphere is constant at 2.73 K. When observed by a downward-looking radiometer, the downwelling brightness temperature is seen as $(1 - e)T_d$ due to reflection from the surface. In this work, we assume only specular reflections and do not consider the effects of scattering and diffraction from a rough surface, such as those mentioned in [11]. These contributors can be combined to obtain an expression for the antenna temperature, as shown in Eq. 1-28.

$$T_A = T_{atm}(1 - Y_u) + Y_u(eT_{surf} + (1 - e)[T_{atm}(1 - Y_d) + 2.73Y_d]) \quad (1-28)$$

Now that an expression for the antenna temperature has been explained, it is noteworthy to turn attention to the radiometric receivers, or radiometers, that measure these brightness temperatures. In Section 1.5 several different radiometer topologies and their advantages and disadvantages are explored.

1.5: Microwave and Millimeter-wave Radiometry

A radiometer is a very sensitive receiver designed to measure the thermal emission which has been discussed in the previous sections. There are many different radiometer topologies; however, the three discussed in this section can be considered the three most basic ones. They are covered in order of complexity, from the total power radiometer to the noise injection radiometer. A system diagram of a total power radiometer is shown in Fig. 1-5.

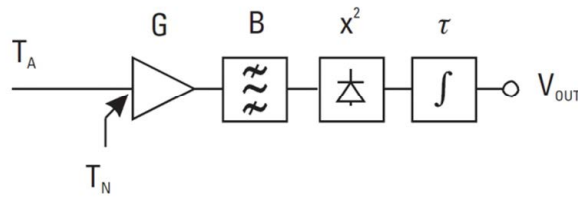


Fig. 1-5: System diagram of a total power radiometer

As the name suggests, in a total power radiometer the total amount of power radiated by the scene is detected by the radiometer, which in this case consists of an antenna, gain stage, band pass filtering, and detection. In nearly all radiometers, detection is accomplished by using a square law detector. With the total power radiometer, the output is highly dependent upon gain fluctuations and system noise. At this point, it is appropriate to introduce the concept of radiometric resolution. The radiometric resolution of a radiometer is the smallest change in input brightness temperature that can be detected in the system output. This quantifies the standard deviation of the mean of a number of measurements of the same quantity made over a short enough time period such that the system can be considered stable [12]. Shown in Eq. 1-29 is the

radiometric resolution relationship for a total power radiometer, assuming no gain fluctuations in the receiver.

$$NE\Delta T = \frac{T_A + T_N}{\sqrt{\beta t}} = \frac{T_{sys}}{\sqrt{\beta t}} \quad (1-29)$$

In this equation, the radiometric resolution, also called the noise equivalent delta temperature, $NE\Delta T$, is the ratio of the sum of the antenna and noise temperatures, T_A and T_N respectively, to the square root of the bandwidth, β , and integration time, t . Due to gain variations, total power radiometers need to be calibrated on a time scale of seconds to minutes, and depending on temperature variations, it may not be stable enough to provide meaningful measurements [13]. In an attempt to remedy this problem, the Dicke radiometer, shown in Fig. 1-6, was developed.

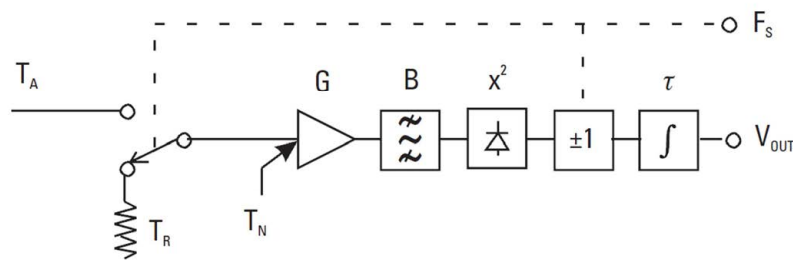


Fig. 1-6: System diagram of a Dicke radiometer

As seen in Fig. 1-6, the Dicke radiometer is similar to the total power radiometer except that the input is switched between the antenna, or scene, and a matched load. Depending on the switch position, the signal is modulated by a factor of positive or negative one. In this way, the output of the Dicke radiometer can be regarded as the difference between the outputs of two total power radiometers [13]. As such, if each total power branch is considered independent, the radiometric resolution of the Dicke radiometer can be quantified as a combination of the radiometric resolutions of each, as was explained in Eq. 1-29. In the example shown here, the Dicke

radiometer is assumed to be balance, meaning the antenna temperature and receiver noise temperature are equal. Therefore, the radiometric resolution of the Dicke radiometer can be quantified as Eq. 1-30.

$$NE\Delta T = 2 \frac{T_A + T_N}{\sqrt{\beta t}} \quad (1-30)$$

However, Eq. 1-29 is typically an overestimate of the radiometric resolution of the Dicke radiometer due to several of the assumptions made in the derivation. As such, it can be viewed as an estimate of the radiometric resolution and another such estimate is shown in Eq. 1-31.

$$NE\Delta T = 2 \frac{T_R + T_N}{\sqrt{\beta t}} \quad (1-31)$$

The T_R term in Eq. 1-31 represents the equivalent antenna temperature of the reference load. In reality, the radiometric resolution of the Dicke radiometer is between Eq. 1-30 and 1-31 since the assumption that $T_A = T_R$ does not always hold [13]. However, the difference between these two is considered small and often ignored in practical applications. As such, either Eq. 1-30 or 1-31 can be used to calculate the radiometric resolution of the balanced Dicke radiometer if the antenna and receiver noise temperatures are assumed to be equal [13]. This radiometer topology is less sensitive to gain fluctuations than the total power radiometer and tends to be capable of providing reliable measurements with less strict calibration requirements. As a trade-off, the Dicke radiometer has typically poorer sensitivity than the total power radiometer. In attempt to make an even more stable radiometer, the noise-injection radiometer shown in Fig. 1-7 was developed.

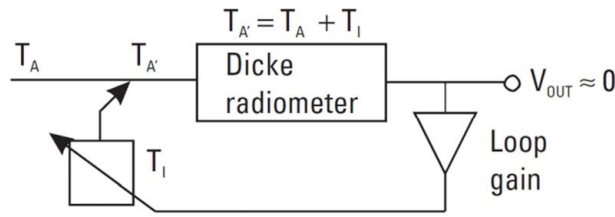


Fig. 1-7: System diagram of a noise-injection radiometer

As seen in Fig. 1-7, the noise-injection radiometer is essentially a Dicke radiometer whose input has an additional noise component added to it. This results in the difference between the new scene temperature, $T_{A'} = T_A + T_I$, as shown in Fig. 1-7, and the reference signal (from the Dicke Radiometer shown in Fig. 1-6), T_R , is nearly zero. Typically the noise sources used for injecting noise into the radiometer input are made using noise diodes. Modern noise diodes are extremely stable, resulting in a measurement that is mostly dependent upon how well the noise diode's noise characteristics can be quantified. In terms of radiometric resolution, the noise-injection radiometer has the same radiometric resolution as Eq. 1-29 if the antenna temperature $T_{A'}$ is equivalent to the reference temperature, which is usually the case.

There are other radiometer topologies which have various trade-offs in radiometric resolution, stability, and noise immunity; however, they will not be discussed in this work. Now that a foundation for understanding radiometers has been established, one can continue to develop ways to discern meaningful products, such as wet path delay, from their measurements. Before introducing the new approach that is the focus of this thesis, it is useful to consider past approaches, as discussed in Section 1.6.

1.6. Existing Coastal Retrieval Algorithms

In order to derive physically meaningful products from brightness temperatures, retrieval algorithms are needed which can use the brightness temperatures, typically along with other data, to retrieve geophysical parameters, such as the tropospheric wet path delay. Since this work is

based on the detection and measurement of wet path delay in the coastal and inland water zones, two previous algorithms by S. Brown [5] and R. Bennartz [6] which have been used to determine the wet path delay will be discussed.

The algorithm proposed by S. Brown involved observations of the fraction of land present in radiometer scenes and applied models to estimate the emission of the mixed-pixel. With this approach, the brightness temperature measurements were separated into land and water contributions. From here the wet path delay was retrieved up to approximately 2 km from the coast using a modified open-ocean algorithm with *a priori* information from databases. This approach reports an error on the order of 1.5 cm.

The second approach proposed by R. Bennartz corrected the brightness temperature measurements near the land based on models. From here, a standard open-ocean algorithm was applied to obtain wet path delay values. This error obtained using this method was on the order of 2-3 cm.

In an attempt to avoid using prior data, such as radiosonde launches, a new algorithm based on measuring the deflection between land and water pixels has been introduced. This algorithm, named the Brightness Temperature Deflection Ratio (BTDR) algorithm, is the focus of this work and will be discussed in detail in Chapter 2.

Chapter 2: Brightness Temperature Deflection Ratio Algorithm

After developing the required background information, one can now turn attention to developing the theory and practice for the Brightness Temperature Deflection Ratio (BTDR) algorithm. In this chapter, the theory behind the BTDR algorithm is explained, as well as a brief synopsis of the edge detection and absorption model which is used. Additionally, as a point of further understanding for how the algorithm and its various contributors work computationally, the code flow of the MATLAB implementation of the algorithm is covered.

2.1 Theoretical Introduction to BTDR Algorithm

Before formally introducing the algorithm, it is useful to consider, intuitively, what is measured to retrieve wet path delay using this algorithm. Initially, the concept of the algorithm described in this section arose from observations of the window channel imagery of the Advanced Microwave Sounding Unit (AMSU) and the Special Sensor and Microwave Imager (SSM/I). In this imagery, one can see a clear reduction in brightness temperatures in the millimeter wave channels between land and nearby water pixels. This suggested that detecting the amount of water vapor present in the atmosphere would be possible if one were able to discern parameters, such as the transmissivity, concerning the state of the atmosphere in these regions. In an attempt to realize this idea, an algorithm based on measuring the deflection between neighboring pixels in coastal and in-land water regions is developed.

If we assume a basic atmosphere model where the measured radiation is due to only surface emission and atmospheric transmissivity (i.e. upwelling and downwelling radiation are not considered) then it is possible to determine the wet path delay through the atmospheric transmissivity by relating differences of brightness temperature measurements between two scenes. This is done by assuming that the emissivity of the surfaces are approximately the same with respect to frequency but differ with respect to the type of surface. By using multiple ratios of brightness temperature differences over the scenes, it is possible to retrieve the wet path delay

by adjusting the transmissivity of the atmosphere until the error between the measured brightness temperatures and brightness temperatures synthesized from a model is obtained.

By assuming a simplified radiative transfer model and applying this methodology, the deflection ratios take the form shown in Eq. 2-1.

$$D = \frac{e_{m-f_1} T_m \Upsilon_{f_1} - e_{n-f_1} T_n \Upsilon_{f_1}}{e_{m-f_2} T_m \Upsilon_{f_2} - e_{n-f_2} T_n \Upsilon_{f_2}} \quad (2-1)$$

By assuming the surface emissivities are roughly equal with respect to frequency and that any transmissivity can be written as the transmissivity at f_1 to some power k , then D is given by Eq. 2-2.

$$D = \Upsilon_{f_1}^k \frac{\Delta T_{Bf_1}}{\Delta T_{Bf_2}} = D' \Upsilon_{f_1}^k \quad (2-2)$$

If k can be modeled accurately, then the error between the measured deflection ratios, D , and a model deflection ratio can be minimized by finding the optimal choice of D' and Υ_{f_1} for several different deflection ratios. This leads to knowledge of the wet path delay by inverting the model for transmissivity.

With the intuitive description of the algorithm in mind, one can turn attention to the mathematical theory behind the BTDR algorithm. Recall from Chapter 1 that the brightness temperature measured by a nadir pointing microwave radiometer in observing a non-scattering atmosphere, T_A , is quantified as in Eq. 2-3

$$T_A = T_{atm}(1 - \Upsilon_u) + \Upsilon_u(eT_{surf} + (1 - e)[T_{atm}(1 - \Upsilon_d) + 2.73\Upsilon_d]) \quad (2-3)$$

As mentioned before, this antenna temperature depends on both upwelling and downwelling brightness temperatures, T_u and T_d as were shown in Section 1.3, which are functions of the upwelling and downwelling transmissivities of the atmosphere, Υ_u and Υ_d , respectively, as well as several other contributing factors. If the radiometer observes two distinct surfaces, e.g. land

and water, with emissivities, e_m and e_n , respectively, we can determine the transmissivity of the atmosphere, assuming it is homogeneous over the two observations, by minimizing a cost function constructed from the sum of squared errors between measured and modeled deflection ratios for each frequency pairing. Then, the atmospheric transmissivity can be mapped to a wet path delay by using absorption models.

In order to do this, consider the model deflection ratio for a frequency channel pairing $\{f_1, f_2\}$, which is formed by first considering the difference between the antenna temperatures, shown in Eq. 2-4, for two different scenes, m and n , at a single frequency f_1 .

$$\Delta T_{A_{f_1-mn}} = Y_{uf_1} [(e_{f_1-m} T_{surf-m} - e_{f_1-n} T_{surf-n}) - (e_{f_1-m} - e_{f_1-n}) [T_{atm} (1 - Y_{df_1}) + 2.73 Y_{df_1}]] \quad (2-4)$$

As seen in Eq. 2-2, the difference in antenna temperatures is established by introducing equations of the form in Eq. 2-1 for each of the surfaces and then subtracting. In a practical matter, using a difference allows us to avoid uncertainties in resolving the atmosphere above a single surface scene and reduces the number of unknowns in the retrieval. From here, if such differences of the form in Eq. 2-4 are considered for two frequency channels, f_1 and f_2 , one can form a brightness temperature deflection ratio by taking the ratio of the channel differences to one another. In other words, the brightness temperature deflection ratio is the ratio of the differences between the antenna temperature difference for scenes m and n at frequencies f_1 and f_2 , as can be seen in Eq. 2-5.

$$M_{f_1 f_2 - mn} = \frac{Y_{uf_1} \{ (e_{f_1-m} T_{surf-m} - e_{f_1-n} T_{surf-n}) - (e_{f_1-m} - e_{f_1-n}) T_{atm} (1 - Y_{uf_1}) \}}{Y_{uf_2} \{ (e_{f_2-m} T_{surf-m} - e_{f_2-n} T_{surf-n}) - (e_{f_2-m} - e_{f_2-n}) T_{atm} (1 - Y_{uf_2}) \}} \quad (2-5)$$

In constructing the model deflection ratio, it is necessary to assume the atmosphere is constant over the two surfaces, m and n . Additionally, the upwelling and downwelling transmissivities are assumed equal. This assumption should be valid so long as the atmosphere meets the non-

scattering assumption used in the radiative transfer model from Section 1.3. Now that an expression for the model deflection ratio, $M_{f_1 f_2 - mn}$, has been explained, several simplifications can be made which can reform it in a way that is more conducive to two-dimensional minimization. The first of these assumptions is to gather several terms into a single parameter, as shown by Eq. 2-6.

$$z(f) = \frac{\Delta T_{surf-mn}(f)}{T_{atm} \Delta e_{mn}(f)} - 1 \quad (2-6)$$

Before discussing the new parameter, one should note that in doing this, the differences in surface physical temperature and surface emissivity have been condensed into differential notation, that is $\Delta T_{surf-mn}(f)$ and $\Delta e_{mn}(f)$ respectively. This new parameter, $z(f)$, allows the combination of several parameters in which the purpose of the algorithm, retrieving the wet path delay by way of transmissivity, is not directly concerned with. Therefore, we can reduce the complexity of the minimization by introducing this lumped parameter. It should be noted that the parameter is, by this derivation, frequency dependent. However, this would mean that the number of minimization parameters would scale with the number of frequency channels which are used and is an unwanted result in this work as it would result in a far more complicated, more time consuming to perform the calculations required for the algorithm. With that said, the lumped parameter will be assumed constant with frequency, $z(f) \rightarrow z$, for the remainder of this work and errors due to this assumption can be accepted as part of the algorithm. This assumption is made because helps to constrain the number of optimization variables, as introducing more degrees of freedom to the optimization implies less stringent requirements on its convergence and therefore could lead to multiple or misleading solutions, increasing uncertainty in the retrieved result. Furthermore, a point of interest about Eq. 2-6 is the case in which it can become degenerate. Specifically, if the emissivities of the targets is equal then the Δe_{mn} is zero and z becomes infinite. A histogram showing the distribution of the z values calculated using Eq. 2-6 is shown in Fig. 2-1.

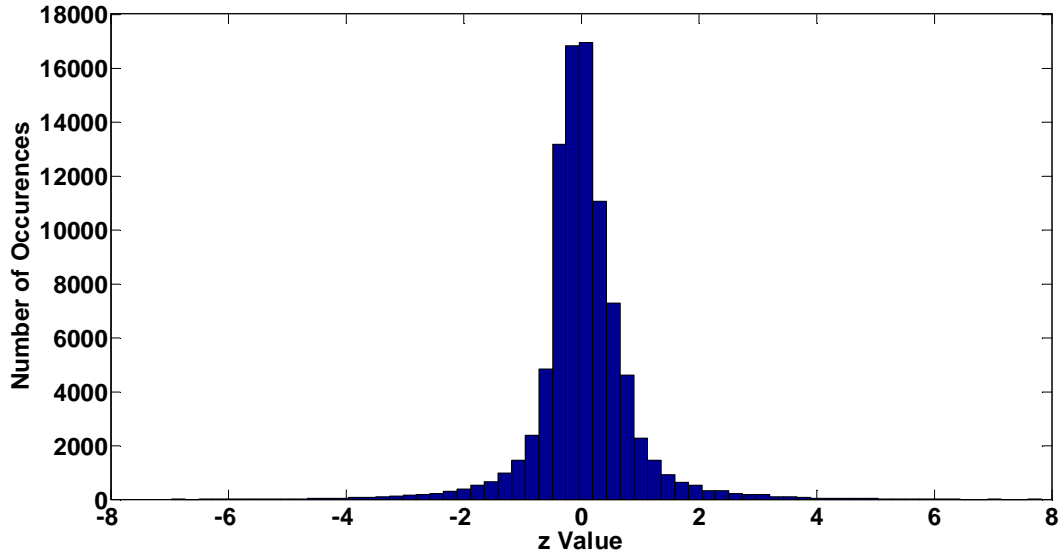


Fig. 2-1: Histogram of possible z values based on the definition of z from Eq. 2-4, assuming no frequency dependence.

The distribution of z values shown in this histogram is based on the possible combinations of surface temperature, surface emissivity, and mean atmospheric temperature which have been observed on Earth. The emissivities are allowed to range from 0 to 1 with and the physical temperatures are allowed to range from the minimum and maximum observed temperatures on Earth. Now that the lumped parameter, z , has been established, one can further assume that the transmissivity has two components, Y_D and Y_W , one due to the dry absorption (from oxygen and to a lesser extent nitrogen) and another due to the wet absorption (from water vapor), respectively. Using this new assumption, it is possible to write the wet transmissivity at any frequency f_2 in terms of only the wet transmissivity at frequency f_1 by Eq. 2-7.

$$r_{f_2 f_1} = \frac{E[\tau_{Wf_2}(\overline{WPD})]}{E[\tau_{Wf_1}(\overline{WPD})]} \Rightarrow \frac{Y_{Wf_1}}{Y_{Wf_2}} = Y_{Wf_1}^{1-r_{f_2 f_1}} \quad (2-7)$$

The quantity $r_{f_2 f_1}$ is the ratio of the expected value of opacities at f_2 , τ_{Wf_2} , to that at f_1 , τ_{Wf_1} , for all possible wet path delay values, \overline{WPD} , in the range of 0 to 35 cm. Using the equation for transmissivity established in Chapter 1 for Y_D , one can reform a ratio of transmissivities into a

single wet transmissivity as a function of r . Using Eq. 2-7, one can simplify the model deflection ratio for two frequencies, f_1 and f_2 , into Eq 2-8.

$$M_{f_1 f_2 - mn} = \frac{Y_{Df_1} Y_{Wf_1}^{(1-rf_2f_1)}}{Y_{Df_2} Y_{Wf_1}} \frac{(z + Y_{Df_1} Y_{Wf_1}) \Delta e_{f_1 - mn}}{(z + Y_{Df_2} Y_{Wf_1}^{rf_2f_1}) \Delta e_{f_2 - mn}} \quad (2-8)$$

This form of the model deflection ratio is more conducive to two-dimensional minimization with respect to Y_{Wf_1} and z as many of the unknowns in previous forms have been accounted for. The two unaccounted for terms in Eq. 2-8, namely Y_{Df_i} and $\Delta e_{f_i - mn}$ where $i \in \{1, 2\}$, are accounted for by the use of the Rosenkranz absorption model with considerations of the absorption of nitrogen [9, 14, 15] or the land/water emissivity models of [16, 17] respectively.

Now that a model deflection ratio has been established for use in constructing a cost function, attention can be turned to the deflection ratio of the measured brightness temperatures. Shown in Eq. 2-9 is the measured deflection ratio for brightness temperatures of the scenes m and n at frequencies f_1 and f_2 .

$$D_{f_1 f_2 - mn} = \frac{T_{Bf_1 - m} - T_{Bf_1 - n}}{T_{Bf_2 - m} - T_{Bf_2 - n}} \quad (2-9)$$

By computing the squared difference between the modeled and measured deflection ratios from Eq. 2-8 and 2-9, one can quantify the error between the two. By minimizing this error, it is possible to find the optimal Y_{Wf_1} and z pair for the two observed pixels. Along with this comes an implicit assumption that the atmosphere stays the same above both of the observed pixels. In order to transition this concept to more than two frequency channels, consider an instrument with a set of p frequencies $\mathcal{F}_p = \{f_1, f_2, \dots, f_p\}$. If unique pairs of the frequency channels are formed, this results in a total number of channel differences equal to $p - 1$ and a total number of deflection ratios as defined by Eq. 2-10.

$${}_p C_k = \frac{p!}{k!(p-k)!} \quad (2-10)$$

Since pairs of frequency channels are used in computing the deflection ratios $k = 2$. From here, one can form a cost function composed of the sum of squared errors, as discussed previously, to compute the total error in the optimization problem. This cost function, shown in Eq. 2-11, is a two-dimensional minimization problem with ${}_p C_k$ terms, each with respect to Y_{Wf_1} and z .

$$\chi^2 = \sum_{\substack{f_i, f_j \in \mathcal{F}_p \\ s.t. j > i}} [D_{ij-mn} - M_{ij-mn}(Y_{Wf_1}, z)]^2 \quad (2-11)$$

Once a value for Y_{Wf_1} has been found, it can then be mapped to a corresponding wet path delay by inverting the transmissivity model described in Chapter 2. This is done by first discretizing the transmissivity equation with respect to total amount of water vapor and then evaluating it at each point. The retrieved transmissivity value is then mapped to an equivalent water vapor amount corresponding to the discretization size of the transmissivity model. The chosen threshold for the retrievals using measured data was chosen as 0.001, as this provided sufficient transmissivity resolution for ensuring resolution of 0.05 cm in the wet path delay. This value was chosen because it provides a low enough quantization level for the wet path delay values to avoid impacting the retrieved results and still allows for fast computation.

One of the practical aspects of using the BTDR algorithm is in how to compute the absorption coefficients used to calculate the required transmissivities for the minimization. In this work, the 1998 Rosenkranz absorption model was used and will be explained briefly in Section 2.2.

2.2 Atmospheric Absorption Models

Although several models for atmospheric absorption exist, the one chosen for the absorption coefficient calculations in this work was the Rosenkranz 1998 absorption model [9]. This model includes contributions to the absorption based on two concepts, line absorption and continuum

absorption. The line absorption is based on measurements made at several frequencies in the microwave to near-optical regions and for the purposes of this work can be quantified as in Eq. 2-12.

$$\alpha_{line} = n \sum_i S_i(T) [f_i(\nu) + f_i(-\nu)] \quad (2-12)$$

At this time it is convenient to point out that a change in notation for this section has occurred in order to remain consistent with the reference terminology. In this case, n , is the number density of water molecules, ν is frequency, f_i represents line shape functions that are frequency dependent, and S_i represents a line intensity function that is dependent upon temperature, T , in Kelvin. The line intensities are based on further models and databases, such as the High-resolution TRANsmission (HITRAN) database from [18], and will not be discussed further as they are out of the scope of this Master's thesis. The line shape functions can be quantified by Eq. 2-13, assuming cutoff frequency ν_c .

$$f_i(\nu) = \begin{cases} \left(\frac{\nu^2 \gamma_i}{\pi \nu_i^2} \right) \left\{ \frac{1}{[(\nu - \nu_i)^2 + \gamma_i^2]} - \frac{1}{\nu_c^2 + \gamma_i^2} \right\}, & |\nu - \nu_i| < \nu_c \\ 0, & |\nu - \nu_i| \geq \nu_c \end{cases} \quad (2-13)$$

In equation 2-13, ν_i defines the center frequency of the absorption line and γ_i represents the line half width. The half-width of the line is a semi-empirical function of the partial pressures of water vapor and dry air. In the microwave and millimeter wave region, there are two lines, 22.235 and 183.31 GHz, although contributions from higher frequency lines, up to 750 GHz, are included in calculating the value of the line shape function [9]. Now that a basis for understanding the line contribution to absorption has been established, one can begin to quantify the continuum contribution. In an intuitive sense, this represents the values in between the line frequencies and is a way of considering un-modeled contributions to the absorption than those in the line summation. As such, one can consider the total absorption as the addition of the line and continuum absorption terms, as shown in Eq. 2-14.

$$\alpha = \alpha_{line} + \nu^2 \theta^3 (C_f P_f P_{H_2O} + C_s P_{H_2O}^2) \quad (2-14)$$

This equation quantifies the absorption due to water vapor in air, α , to the line absorption plus a continuum term composed of θ , defined as $300/T$, The partial pressures of dry air and water vapor, P_f and P_{H_2O} respectively, and two coefficients, C_f and C_s . The coefficient, C_f , depends on both temperature and frequency and represents what is known as the foreign-broadened component of water vapor continuum and is typically obtained by observation. The terminology “foreign-broadened” indicates effects on the water vapor continuum due to interactions with molecules other than pure water. Similarly, C_s represents the self-broadened component of the continuum and is taken from effects on the continuum due to interactions between water molecules. At frequencies below 800 GHz, C_s can be represented by Eq. 2-15.

$$C_s = 7.8 \times 10^6 \theta^{4.5} \quad (2-15)$$

Taking all of these factors into account, one can merge the information in Eq. 2-14 into a partial-pressure dependent total absorption by representing the line absorption in a similar manner as the continuum absorption. Shown in Eq. 2-16 is the partial-pressure dependent form of the total absorption with temperature and frequency dependent coefficients, a , b , and c .

$$\alpha = a P_f P_{H_2O} + b P_{H_2O}^2 + c P_f \quad (2-16)$$

2.3 Edge Detection Algorithms

Now that the basic theory of the Rosenkranz absorption model has been covered, it is useful to shift the focus of to a more practical aspect of retrievals using the BTDR algorithm; how does one determine the locations of transition regions, i.e. land/water boundaries, to apply the algorithm to? The answer to this, for this work, is to use edge detection algorithms on brightness temperature maps to determine which areas show contrast. In order to start the discussion, it is useful to define what an edge is in an image and highlight issues with this definition. To do this, consider the example using the pixels shown in Fig. 2-2.

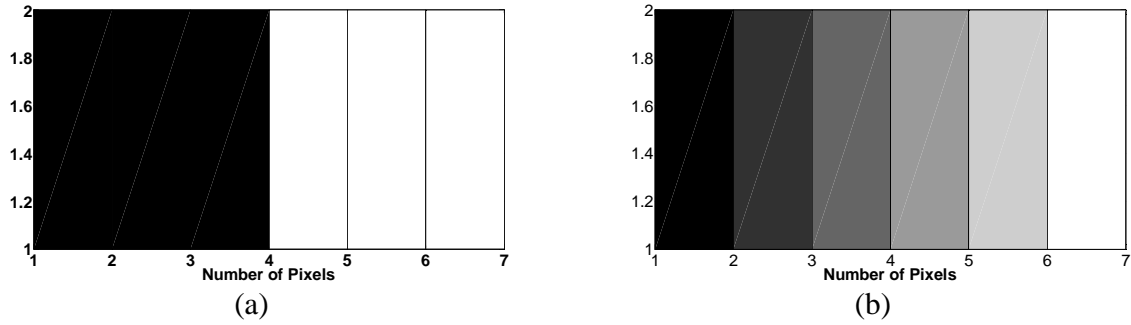


Fig. 2-2: Illustration of the concept of an edge using (a) black and white and (b) grey scaled pixels.

As can be seen by Fig. 2-2a, an edge could clearly be considered to be between pixels 3 and 4 (assuming the pixels are indexed on the left) as there is a sharp transition from black to white. A more interesting case, shown in Fig. 2-2b, is in detecting an edge when the transition is not sharp. In this image, it can be said that there is either a single edge, at between pixels 3 and 5, or two edges, between pixels 2 and 4 and another between pixels 5 and 7. The number of edges seen in the second image is highly dependent upon which threshold is chosen to represent an edge. This highlights, in a simple way, some of the issues with detecting edges that should be kept in mind when applying edge detection algorithms. Some of these algorithms are designed to detect very subtle changes, or only changes in certain directions. The first of the two detector types which will be covered in this section is the Sobel detector. In short, the Sobel detector is a discrete approximation to the two-dimensional gradient of an image with respect to horizontal and vertical directions [19]. Mathematically, this is accomplished by applying horizontal, G_x , and vertical, G_y , such as the 3x3 kernel functions shown in Eq. 2-17.

$$G_x = \begin{bmatrix} -1 & 0 & 1 \\ -2 & 0 & 2 \\ -1 & 0 & 1 \end{bmatrix}, G_y = \begin{bmatrix} -1 & -2 & -1 \\ 0 & 0 & 0 \\ 1 & 2 & 1 \end{bmatrix} \quad (2-17)$$

These kernel functions are then applied to the image to create another image displaying the magnitude of the gradient of the original image, such as those shown in Fig. 2-3.

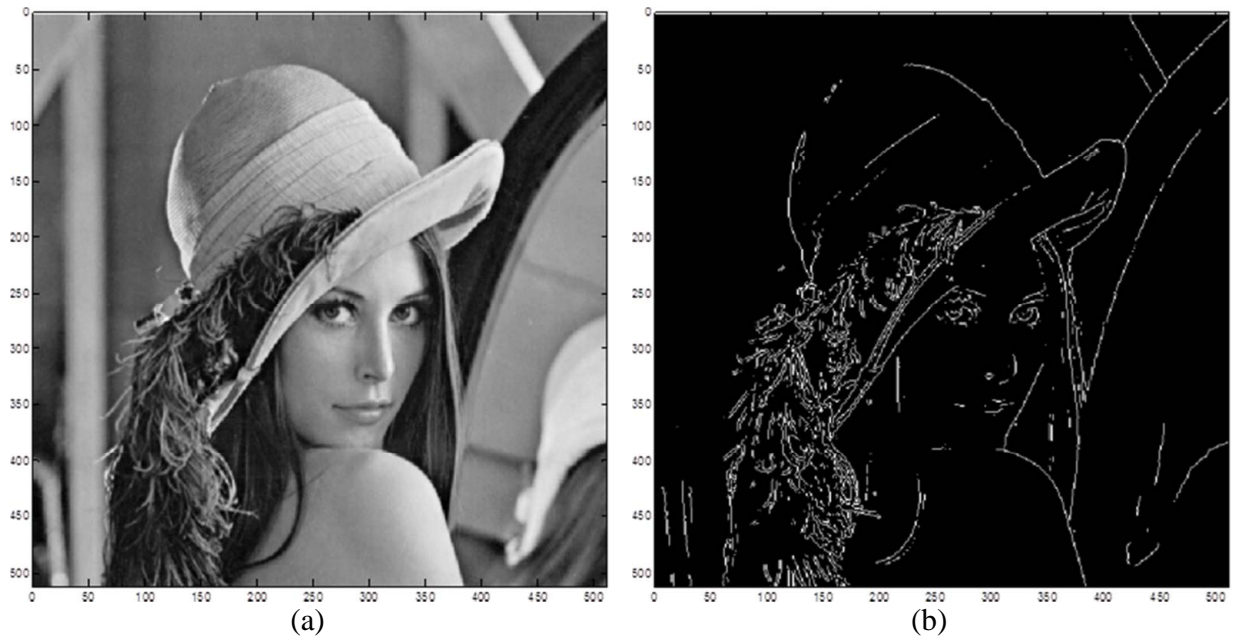


Fig. 2-3: (a) Original image and (b) Sobel gradient detected edges of original image

As can be seen from Fig. 2-3, several edges in the image are detected by observing changes in the gradient. However, the Sobel detector does not detect many of the more subtle features in the image. In order to do this, we refer to the Canny detector [20]. The Canny detector applies similar discrete gradient calculations and also includes several smoothing steps which aid in detecting edges which are less sharp. As an example, the Canny detector was applied to the same image and the edges computed using its gradient approximation are shown in Fig. 2-4.

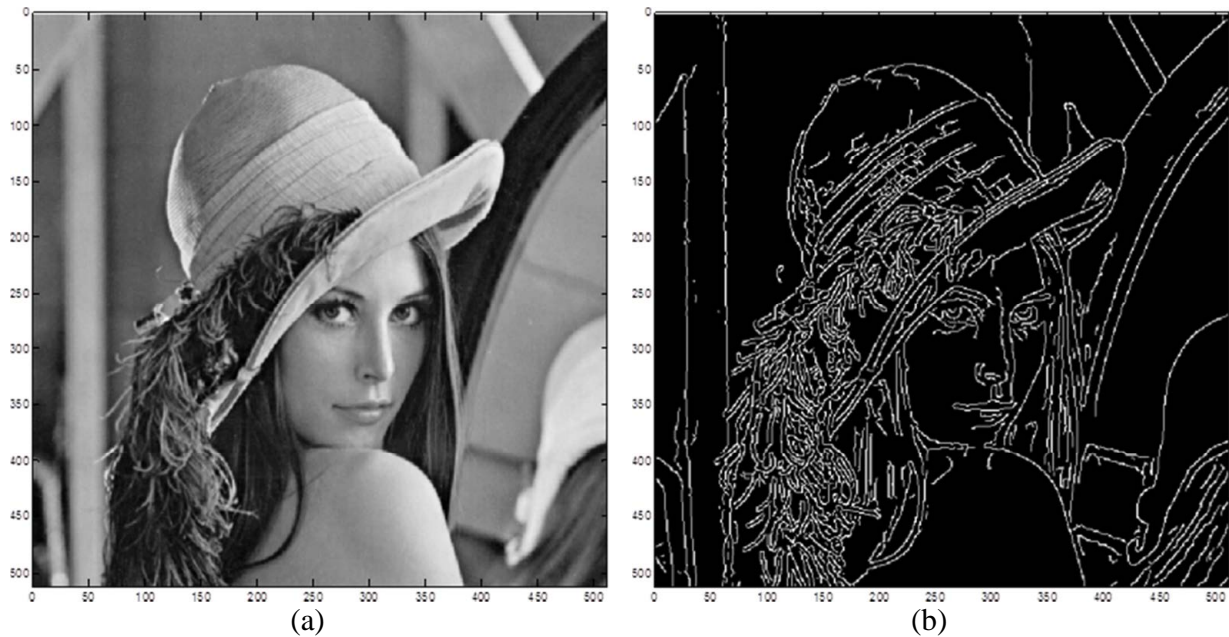


Fig. 2-4: (a) Original image and (b) Canny gradient detected edges of original image

With this detector, many more edges can be seen. This means that the Canny detector can be used to effectively identify subtle changes in images, such as those caused by small inland lakes and rivers like those for this Master's thesis, and the Sobel detector would be beneficial in detecting large features in the image, such as coastlines, without increased sensitivity to fine changes in contrast. In Chapter 5, the use of the Canny detector as a way to identify such small inland features from brightness temperature imagery of the Earth will be demonstrated.

2.4 Software Implementation

In order to implement the algorithm which has been detailed in this chapter, a choice of which platform the development should occur within had to be made. As this stage of the algorithm is a prototype, it was sensible to find a platform which was easy to use and in which code could be written fairly easily. The toolboxes included with MATLAB made it a natural choice, as many of the functions needed for the algorithm to work, such as edge detection and file parsing, were included. Additionally, the code to parse the input files for the independently derived Total Precipitable Water (TPW) products was written using Python as it facilitated the conversion of

the binary data files to ASCII, which could be read using MATLAB. The TPW is a comparable product to wet path delay and can be converted using approaches such as [21].

The main portion of the code, written in MATLAB, contains several core modules which are necessary for the implementation of the algorithm. In order to perform the various retrievals in Chapters 3 and 4, several other code portions are used to provide input to or modify the way the main code body functions. Essentially, the main body of the code contains 5 parts: atmosphere generation and data input, emissivity calculations, calculation of the deflection ratios, cost function minimization, and transmissivity to wet path delay mapping. A data flow diagram showing how these sections interact is shown in Fig. 2-5.

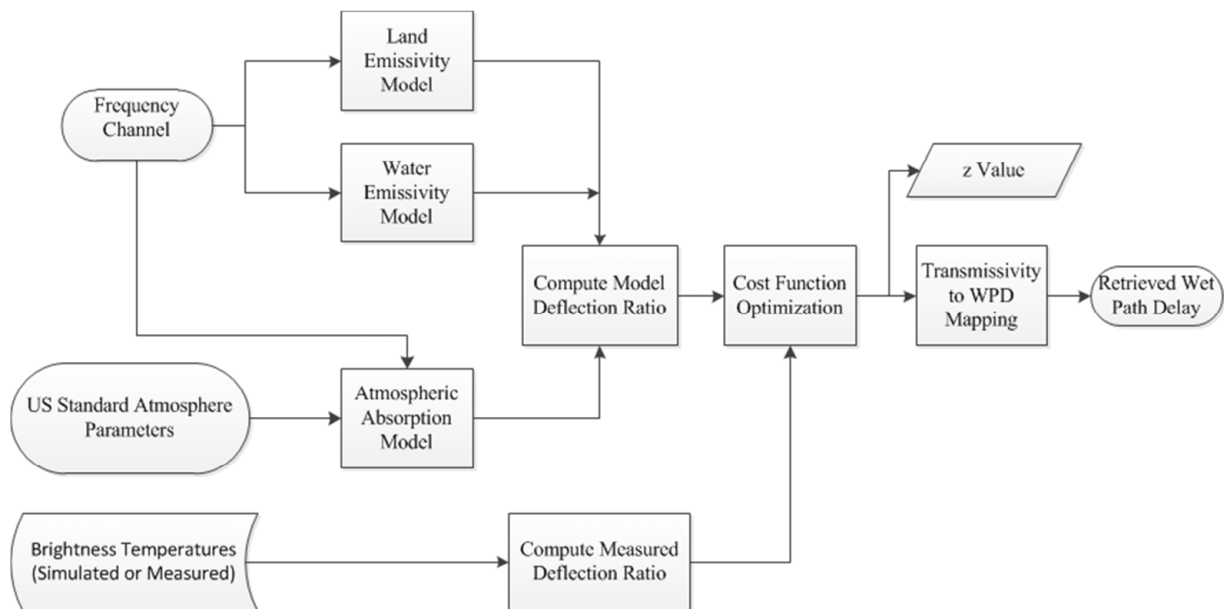


Fig. 2-5: Data flow diagram of the main portion of the code

From Fig. 2-5 it should be noted that this diagram represents only the portion of code which is used to compute the deflection ratios and minimize the cost function. For the simulated retrievals, the input branch for the simulated brightness temperatures is modified to obtain the desired level of noise in the measurements whereas for the measured brightness temperatures, the edge detection algorithms are used to find areas of contrast in which the BTDR method could be applied before passing the brightness temperature measurements on to the main code body. For

the simulated retrievals, changed to the brightness temperatures, scene temperatures, emissivities, and other parameters were needed. In order to streamline this process, an input structure was created. This structure involved several parameters which affected the retrieval input process. In Table 2-1 is a description of the parameters in the input structure.

Table 2-1: Description of input parameters used to perform simulated wet path delay retrievals

Input Parameter Name	Purpose
NumNoisePoints	Defines the number of points used for simulated retrievals included Gaussian distributed noise (default standard deviation is 0.1 cm)
NumWVPoints	Defines the number of wet path delay values for which simulated retrievals are performed (by default between 0 and 35 cm)
WVDist	Defines a distribution of water vapor values for simulated retrieval. Mutually exclusive with NumWVPoints
NoiseDist	Defines a distribution of noise levels to be added to the simulated brightness temperatures. Mutually exclusive with NumNoisePoints
RetFreqs	Defines the frequency set which is used for the retrieval
Emissa	Emissivity of surface “a”
Emissb	Emissivity of surface “b”
Tempa	Temperature of surface “a”
Tempb	Temperature of surface “b”
IncAngle	Incidence angle at which the receiver is assumed to be pointing, in degrees. Set to 0 by default

By use of this input structure, all simulated retrievals, save for those for the contour analysis presented in Chapter 3, can be performed. For the contour analysis, several extra input

parameters are required in order to set up the minimization space. These parameters include definitions for points in the $\{Y_{wf_1}, z\}$ plane at which the cost function evaluations are performed, as well as a saturation threshold, described in Section 3.3, for the images which are produced. For the retrievals from measured data, a similar approach is taken.

Chapter 3: Wet Path Delay Retrieval: Simulation Results

In this chapter various simulated retrievals are performed in order to determine the characteristics of the algorithm in an idealized environment. Several types of simulations are covered and various conclusions can be drawn from their results. However, before any of these can be discussed, it is important to mention how to set up the simulated atmosphere and surface parameters, i.e. surface temperature and emissivity. All of the atmospheres discussed in this chapter are based on simulations using the 1976 U.S. Standard Atmosphere which is detailed in [22]. This model provides mean temperatures and pressures as well as the size of the layers in the simulated atmosphere. The U.S. Standard Atmosphere was chosen as it was decided to be a good model for mid-latitude atmospheres. Additionally, the simulations in this chapter assume nadir incidence angle unless otherwise specified. By doing this, one can exclude considerations for polarization, which will be discussed in Chapter 5. As mentioned in Chapter 2, the ground and emissivity models of [16, 17] are used to provide emissivities for the targets. With this in mind, the discussion continues to a study to analyze how many of the frequency channels in the frequency channel set contribute to the retrieval.

3.1: Determining the Number of Contributing Channels

Before performing retrievals using arbitrary frequency sets, it is useful to examine how many frequency channels are needed in order to perform the wet path delay retrievals. This was accomplished by computing brightness temperature differences and brightness temperature deflection ratios for $N \in \{2, 3, 4\}$ total frequency channels where one of the N channels is allowed to vary. Then, the number of significant eigenvalues calculated from a covariance matrix relating the channels is examined to determine the number of contributing channels. For example, with $N = 3$ there will be 3 frequency channels, one of which is allowed to vary.

To avoid introducing more complexity into the problem in the form of additional degrees of freedom in the frequency channel selection, we begin with the $N = 4$ case and choose sets of three fixed frequencies. These choices include two sets that were identified in the frequency

selection study in Section 3.2, the 50, 52, 113 GHz frequency set used for retrievals with the HAMSR instrument, and 52.8, 91.655, 150 GHz frequency set used in the SSMIS instrument. Then, the number of fixed channels is decreased to form the $N = 3$ and $N = 2$ cases. Furthermore, to perform the simulations several parameters including information about the atmosphere and ground targets were included. These parameters are detailed in Table 3-1.

Table 3-1: Description of simulation parameters for BTDR initialization

Simulation Parameter	Description
T_m	Surface temperature of m
T_n	Surface temperature of n
e_m	Emissivity of surface m
e_n	Emissivity of surface m
T_{atm}	Mean temperature of atmosphere (equal to 277.26 K from U.S. Standard Atmosphere model unless otherwise stated)

The simulations were performed by choosing $N - 1$ channels as described above and then varying the N^{th} channel in the range 40-200 GHz for wet path delay values between 0-35 cm. The first analysis that will take place focuses on the eigenvalues of a covariance matrix composed of the brightness temperature differences for various wet path delay values. The purpose of this comparison is to examine the number of frequency channels which contribute to the retrieval. It should be noted that since the differences are taken for two targets at each frequency, the number of eigenvalues of this matrix will be the same as the number of frequency

channels and is equal to N . For each channel choice, the covariance of the simulated measurement differences was computed with respect to the wet path delay dimension, forming an $N \times N$ covariance matrix. The eigenvalues of the covariance matrix were computed and normalized with respect to the largest eigenvalue and presented for comparison. In order to decide which of the eigenvalues are useful, a threshold needs to be set below which the eigenvalues can be considered insignificant. For the BTDR method, we consider any normalized eigenvalue less than 10^{-3} to be insignificant. With that said, the frequency channel selections providing the best complement to the previously chosen channels are those whose eigenvalues are greater than the threshold. In Fig. 3-1 are the results for the four frequency sets chosen earlier.

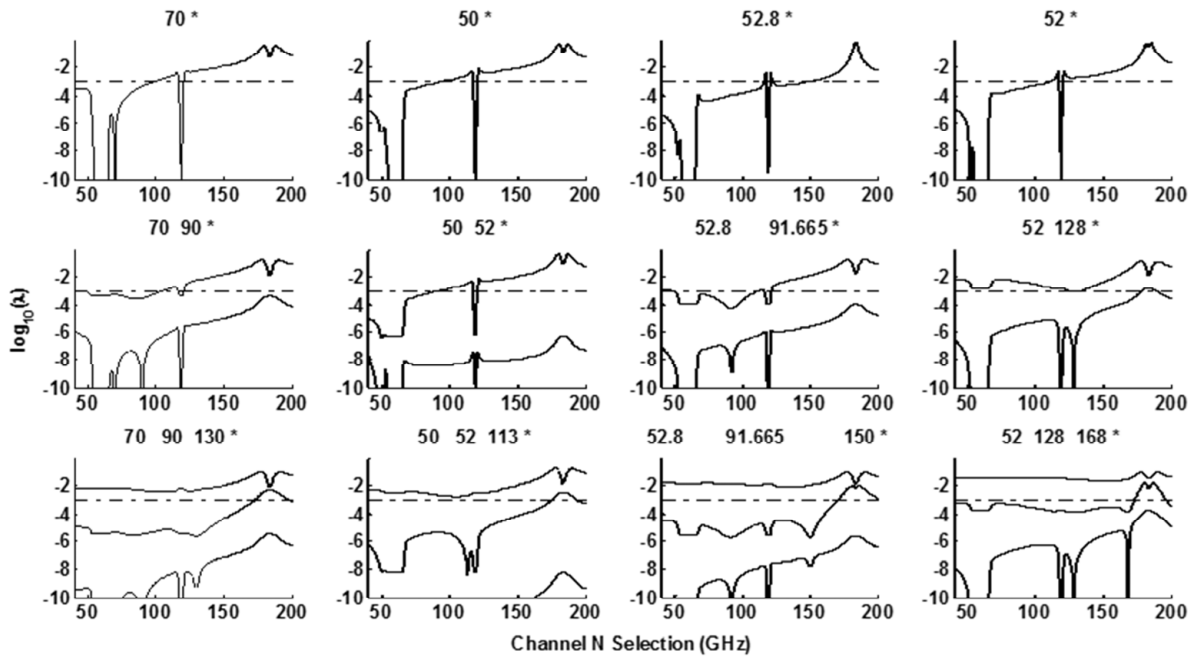


Fig. 3-1: Comparison of the normalized eigenvalues, denoted by λ , for antenna scene temperatures. The * in the figures corresponds to the frequency channel that is allowed to change and is represented by the x-axis. The atmosphere and surface parameters for these simulations are as follows: $T_m = 290$ K, $T_n = 285$ K, $e_m = 0.95$, $T_{atm} = 277.26$ K, and e_n taking values based upon the water emissivity model from [17].

As can be seen in the first row of Fig. 3-1, there are either 1 or 2 significant channels which contribute to the overall measurement of the scenes, depending on the frequency choice that is made. Specifically, there are two significant eigenvalues for the portion of the spectrum from 118 to 200 GHz. However, this results in only a single deflection ratio with which to describe the two-dimensional cost function and would lead to multiple solutions in the optimization process. Continuing to the second row, one can note that by including another channel in the set of channels typically increases the second eigenvalue to above or approximately equal to the threshold of significance in all but the second column, corresponding to the 50, 52, and 113 GHz initial frequency set choice. When choosing a third frequency near the 183 GHz water vapor absorption line, the third eigenvalue is above the threshold, implying that there are three significant contributors to the brightness temperature differences to the cost function formulation. Although this would add greater measurement diversity according to the eigenvalue analysis using a frequency channel near this region would likely introduce errors into the algorithm since brightness temperature measurements at these frequencies would not contain significant contributions from the surface due to high atmospheric opacity. Moving on to the third row yields a similar conclusion for columns 1 through 3, i.e. that there are 2 contributing frequency channel differences (and therefore frequency channels) to the optimization problem. However, in column 4 it is worthy to note that the third eigenvalue has increased by when a fourth channel is added and is nearly at the significance threshold chosen. From this, one could deduce that in certain cases using more than 3 frequency channels could be beneficial. However, this is highly dependent upon the choice for the preceding frequency channels, the analysis of which will not be discussed in detail in this paper. In conclusion, we have verified that for the frequency channel sets that are available to us through current instruments and for the 70, 90, and 130 GHz frequency set, that a set of three channels is sufficient to perform retrievals using the BTDR method and adding further channels does not contribute a significant amount to the retrieval in these cases.

From this analysis, one can conclude that the number of contributing frequency channels is dependent upon specific selection of the channels. However, for the channels which have been chosen for use with the algorithm, it seems that a selection more than two channels does not provide a large contribution to the retrieval. On the other hand, a choice of two channels provides only a single deflection ratio. In the next analysis, the number of contributing deflection ratios based on the same frequency channels is presented.

With that said, it is useful to determine how many of the deflection ratios formed by those channels are useful in performing the retrieval. This is accomplished by performing the same analysis on the brightness temperature deflection ratios as was done for the brightness temperature differences. For this study, the number of eigenvalues of the deflection ratio covariance matrix is $M = 1, 3,$ and 6 for $N = 2, 3,$ and 4 frequency channels respectively. The value M also represents the number of possible deflection ratios when using N frequency channels. The results for this simulation using the frequency sets described above are shown in Fig. 3-2.

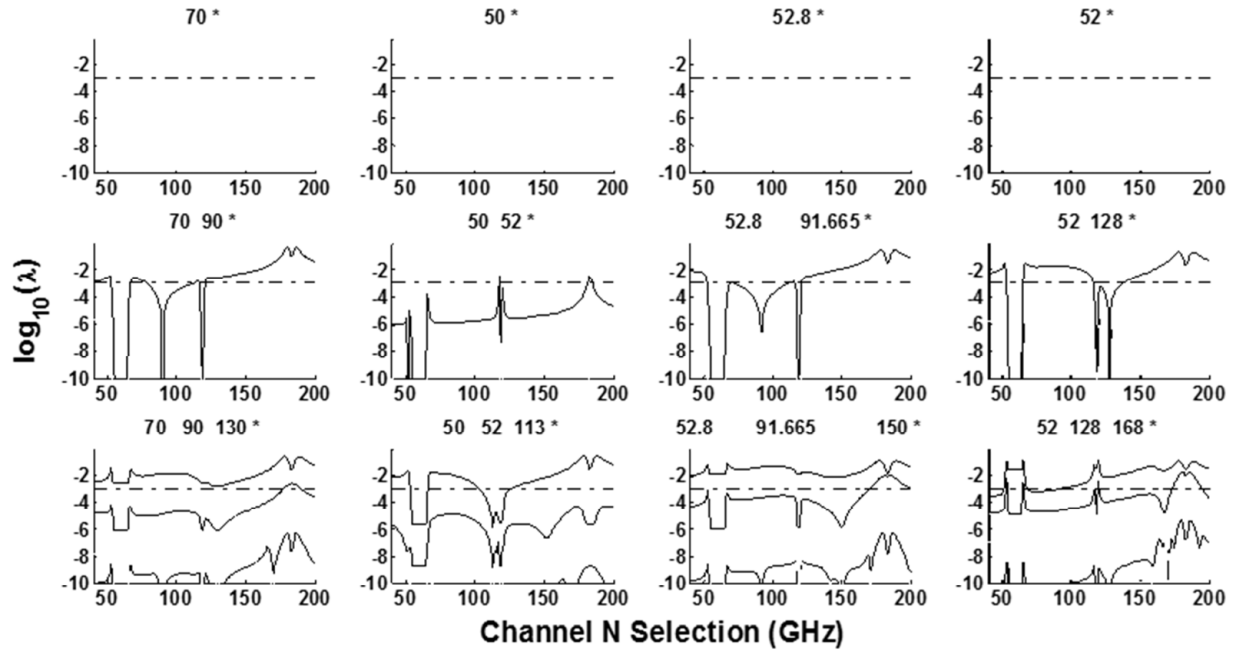


Fig. 3-2: Comparison of the eigenvalues, denoted by λ , of simulated deflection ratios. The * in the title of each figure corresponds to the frequency channel that is allowed to change and is represented by the x-axis. The atmosphere and surface parameters for these simulations are as follows: $T_m = 290$ K, $T_n = 285$ K, $e_m = 0.95$, $T_{atm} = 277.26$ K, and e_n taking values based upon the water emissivity model from [17]

Once again, the eigenvalue threshold is 10^{-3} and normalized eigenvalues lower than the threshold are assumed to be insignificant to solving the problem. Since there is only a single deflection ratio possible for row 1 of Fig. 3-2, analysis of it is not relevant. In row 2 of Fig. 3-2, one can see that of the three deflection ratios formed from three frequency channels only two of them are significant in forming the cost function. This is dependent upon the choice of the third frequency channel in the set. For columns 1 and 3 of row 2, there are only two eigenvalues in the portions of the spectrum from 40 to 50 GHz and from 120 to 200 GHz which are above the threshold, assuming that channels near the 183 GHz water vapor absorption line are not desirable for the retrieval since sufficient surface contrast cannot be seen. In column 4 of row 2, this still holds, however the spectrum between the 60 GHz absorption complex and the 118 GHz absorption line is now also a significant contributor to the cost function value assuming that it is chosen for the

third frequency in the set of channels. In column 2 of row 2, almost any choice for a third frequency channel does not contribute to the formulation of the cost function, and it is almost entirely determined by a single deflection ratio. In columns 1, 3, and 4 of row 3 only two of the six possible deflection ratios are significant in determining the value of the cost function. However, in column 2 (the HAMSR channels) the second eigenvalue increases substantially if a fourth channel from the spectrum is added to the set. This means that the cost function is determined mostly by two deflection ratios rather than one for this frequency set. However, since the portions of the spectrum which allow for four-channel retrieval are not included in the frequency channels available on the HAMSR instrument, further analysis of this frequency set will be performed using a set of three frequencies. Furthermore, since it is determined that two deflection ratios are useful to the retrieval, this emphasizes that three frequency channels should be used, in contrast to the result from the analysis of the brightness temperature difference eigenvalue study.

Since the same atmospheric and surface simulation parameters are used for all of the frequency sets in Fig. 3-1 and Fig. 3-2, it is useful to consider this analysis for different atmospheric and surface conditions. In Table 1, five different combinations of simulation parameters are presented.

The eigenvalues for the 52.8, 91.655, and 150 GHz frequency set are compared to determine if changes in atmospheric and surface conditions could modify the number of contributing frequency channels. We present a comparison of the eigenvalues for the 70, 90, and 130 GHz and 52.8, 91.655, and 150 GHz frequency sets for the five combinations of simulation parameters shown in Table 3-2.

Table 3-2: Description of the 5 simulated atmospheres used to determine the relationships of the eigenvalues of the brightness temperature differences and the brightness temperature deflection ratios. The analysis of these cases is shown in Fig. 4 and 5.

	Case 1	Case 2	Case 3	Case 4	Case 5
T_{atm}	277.26	260	277.26	277.26	277.26
T_m	290	290	290	300	300
T_n	285	285	285	285	300
e_m	0.95	0.95	0.75	0.95	0.95

In these cases, the land is denoted by m and the water is denoted by n . The emissivity for the water target is not shown since it depends on the water emissivity model [17]. The eigenvalues for both the brightness temperature differences and deflection ratios are shown in Fig. 3-3.

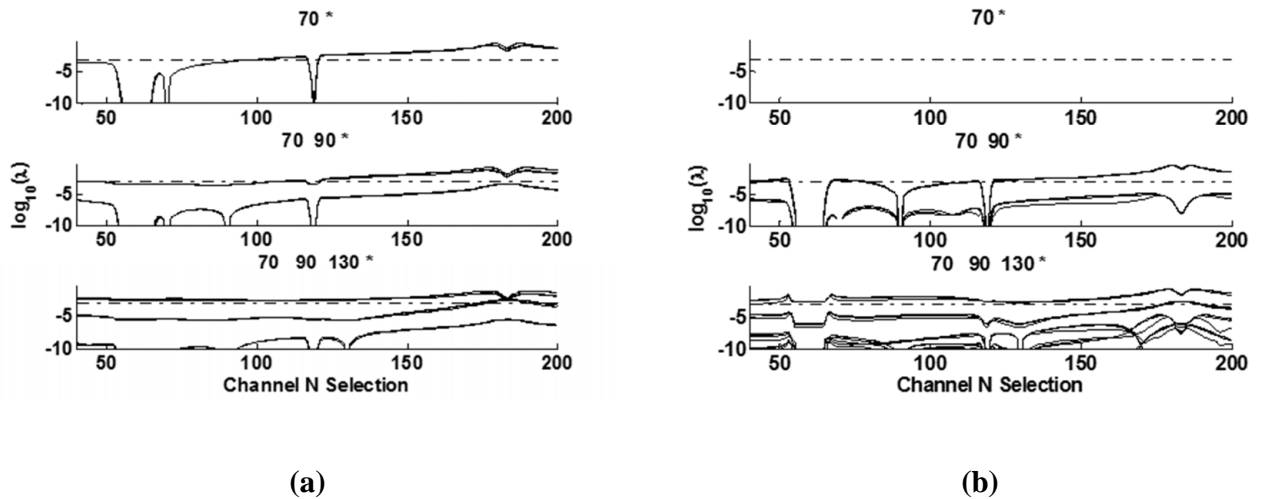


Fig. 3-3: Comparison of the eigenvalues of a) the brightness temperature differences and b) the deflection ratios of the 70, 90, 130 GHz frequency set for the 5 atmospheres shown in Table 3-2.

As can be seen in Fig. 3-3a, the most significant normalized eigenvalue for $N=2, 3,$ and 4 is changed only slightly in the region between 170 to 190 GHz. However, as previously mentioned, this portion of the spectrum is not conducive to use with the BTDR method since it is unlikely that any background emission will be seen due to high water vapor absorption. The rest of the spectrum shows very little sensitivity to changes in atmospheric and background parameters. The lower eigenvalues show little to no sensitivity. In Fig. 3-3b, the most significant eigenvalue is almost entirely insensitive to changes in simulation parameters, although small changes can be seen in the 40 to 100 GHz section of the $N=4$ figure. Significant changes are seen in the lower eigenvalues, especially for $N=4$, however as these eigenvalues are below the threshold, they are not significant in the retrieval. Similar results for the $52.8, 91.655,$ and 150 GHz frequency set are shown in Fig. 3-4.

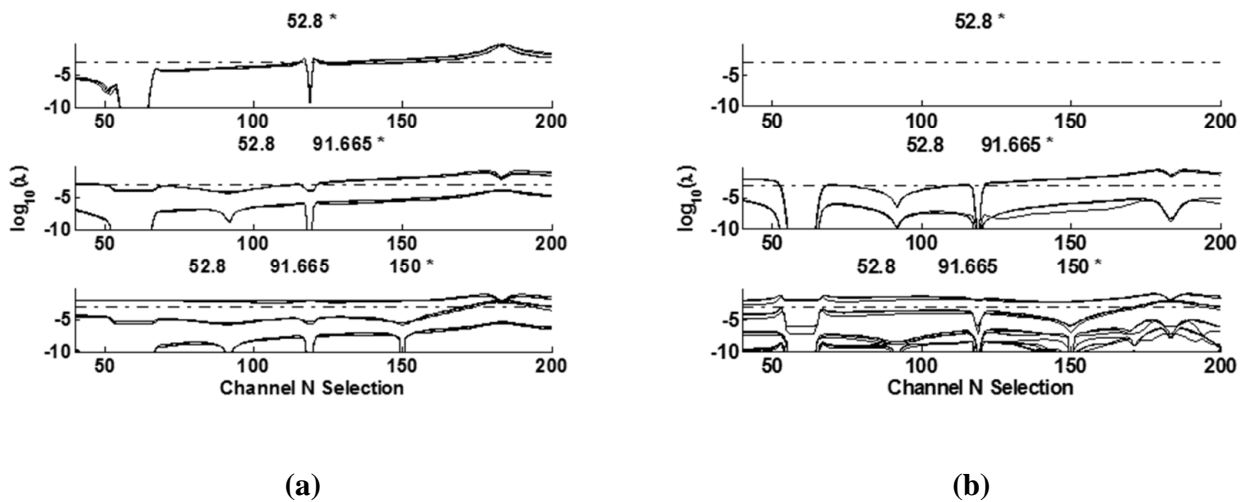


Fig. 3-4: Comparison of the eigenvalues of a) the brightness temperature differences and b) the deflection ratios of the 52.8, 91.665, 150 GHz frequency set for the 5 atmospheres shown in Table 3-2.

Fig. 3-4 (a) shows sensitivity to parameter changes from 120 to 160 GHz for $N = 1$. However, this sensitivity is reduced in the $N = 3$ and 4 cases, implying that sensitivity to varying atmospheric and surface parameters can be reduced by including more frequency channels in the

frequency set used for retrieval. In Fig. 3-4 (b), little to no sensitivity is observed in the most significant normalized eigenvalue. The majority of sensitivity to changes in the atmospheric and surface parameters can be observed in the less significant eigenvalues, indicating that they are not significant.

The results presented in this section show that the number of contributing channels and deflection ratios needed is dependent upon which frequency channels are chosen. However, for the frequency channel selections studied two deflection ratios using three frequency channels are sufficient to perform retrievals. Furthermore, from Fig. 3-1 and Fig. 3-2 we see that including a fourth frequency channel in the set of channels contribute very little to the retrieval and from Fig. 3-3 and Fig. 3-4 that varying atmospheric and surface conditions do not affect the number of contributing channels.

3.2: Frequency Channel Selection

After confirming that three frequency channels are indeed sufficient to perform wet path delay retrievals using the BTDR method, it is useful to examine a way to choose the frequency channels from the available spectrum. These simulations assume that no noise is present, that each frequency channel has infinitesimal bandwidth, and that the amount of water vapor, described by the wet path delay, is the only changing atmospheric variable. This approach allows one to obtain a general knowledge of the choice of frequency channel sets and analyzes their performance when wet path delay, the product of interest for this thesis, is the only changing variable.

This approach will allow us to obtain a guideline of how one could choose frequency channel sets if an instrument were being designed based on the BTDR approach. Retrievals are performed for a number of wet-path delay values using sets of three frequencies between 40 to 200 GHz, namely in the window regions between the absorption lines at 60, 118.75, and 183.31 GHz, as well as a portion of the 25-50 GHz window region, as previously indicated in Fig. 1-3.

This frequency range was chosen such that it would provide a sufficiently small spot size on the ground from a nadir viewing airborne radiometer. Each frequency set was tested using fixed values for dry, temperate and moist atmospheres, i.e. 5, 15, and 30 cm wet path delay, respectively. The cost function minimization was performed over a constrained physically-meaningful range of Y_{Wf_1} from 0 to 1, and letting z range from 0 to 250. Allowing this variation in z does not negatively impact the retrieval accuracy, since this parameter is discarded after the retrieval is performed, and no product is derived from it.

The frequency sets were binned according to the path delay retrieval bias, defined as the difference between the retrieved wet path delay and the actual wet path delay. The bin centers range from 0.01 cm to 1 cm. Any sets which had a mean retrieval bias greater than 1 cm were discarded. Additionally, the sets were separated into three groups within each bin: those with constant error, those with linear error, and those with non-linear error, based on their performance for the three amounts of water vapor tested. This was done as a preliminary test to approximate the linearity of the retrieval over the entire path delay range. Linearity is desirable since linear retrieval error provides results that are easier to interpret. Fig. 3-5 shows the results of the frequency selection criteria study for the 0.01 cm bin using sets with constant and linear retrieval bias.

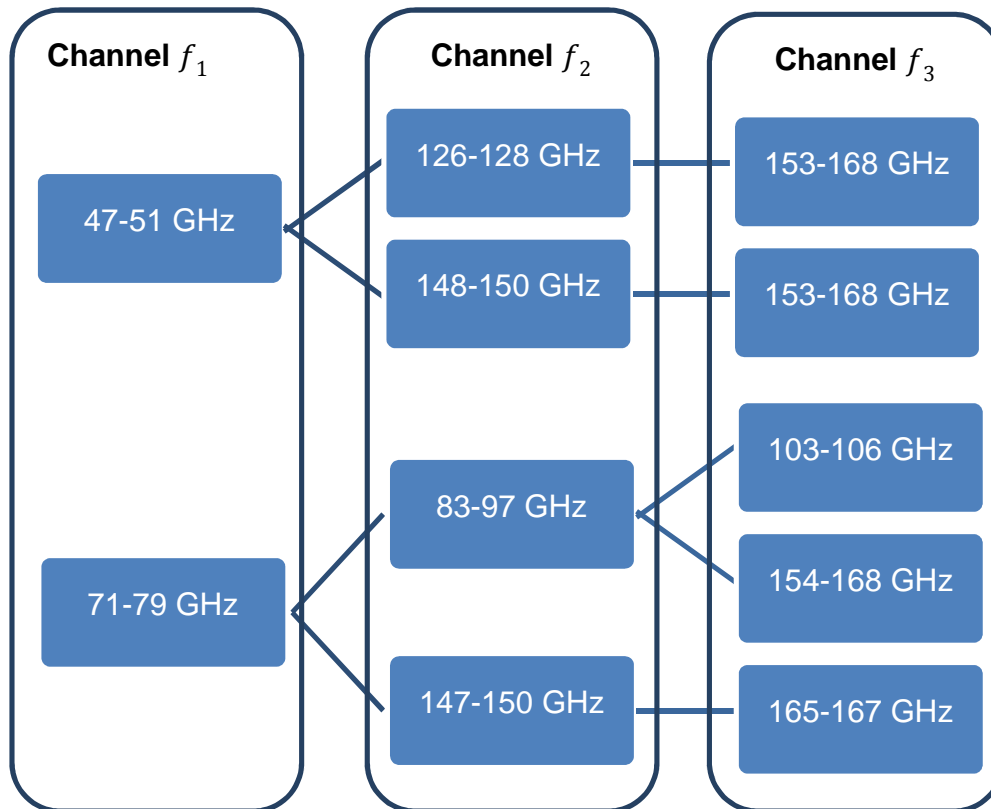


Fig. 3-5: Diagram of frequency selection criteria for 0.01 cm simulated retrieval error

The majority of the frequency channel choices for the retrieval algorithm are in the window regions between the absorption lines in the 40-200 GHz spectrum. This is an expected result since channels too close to the absorption lines would not provide sufficient contrast. Since these regions are relatively broad and based on three sample points in the 0 to 35 cm range, the results from the frequency selection study should be viewed as guidance in choosing frequency channels within the window regions. However, they do not indicate that frequency channels which are not selected using this method are not useful since the results are based on a restrictive set of error constraints. In Section 3.3, analysis of the minimization parameters, Y_{f_1} and z , is presented.

3.3: Stability and Sensitivity Analysis

With that in mind, we also introduce three additional frequency sets which were determined either from observing the relative transmissivities in the 40-200 GHz range or from already available radiometer frequency channels in the field. The first of these, the High Altitude MMIC

Sounding Radiometer (HAMSR), has eight sounding channels near the 60-GHz oxygen complex, ten channels near the 118-GHz oxygen absorption line, and seven channels near the 183-GHz water vapor absorption line [23]. Of these, we found that one of the frequency channel sets which could provide us with minimal error to be 50, 52, and 113 GHz. This was done as part of initial error testing of the BTDR method using the HAMSR channels. Another instrument which provides usable frequency channels in the 40-200 GHz range is SSMIS which has 21 frequency channels as described in [24]. Of these channels, we found that retrievals using the 52.8, 92.665, and 150 GHz channels showed the least error in our preliminary simulations of those available from SSMIS.

For all four selected frequency sets, the behavior of the cost function, χ^2 defined in Section 2.1 by (2-9), is examined on the minimization space $\{Y_{Wf_1}, z\}$ with respect to atmospheric and background parameters. This enables understanding of the effects of those parameters on the retrieval and aids in identifying potential sources of error using the BTDR method by way of contour analysis. In this simulation, the cost function was evaluated with respect to Y_{Wf_1} ranging from 0 to 1 and z , from 0 to 250. To investigate the impact of surface emissivities and temperatures, as well the atmospheric physical temperature, we simulated four cases for a range of these three parameters. The results for the 52.8, 91.655, and 150 GHz SSMIS frequency frequency set are shown in Fig. 3-6.

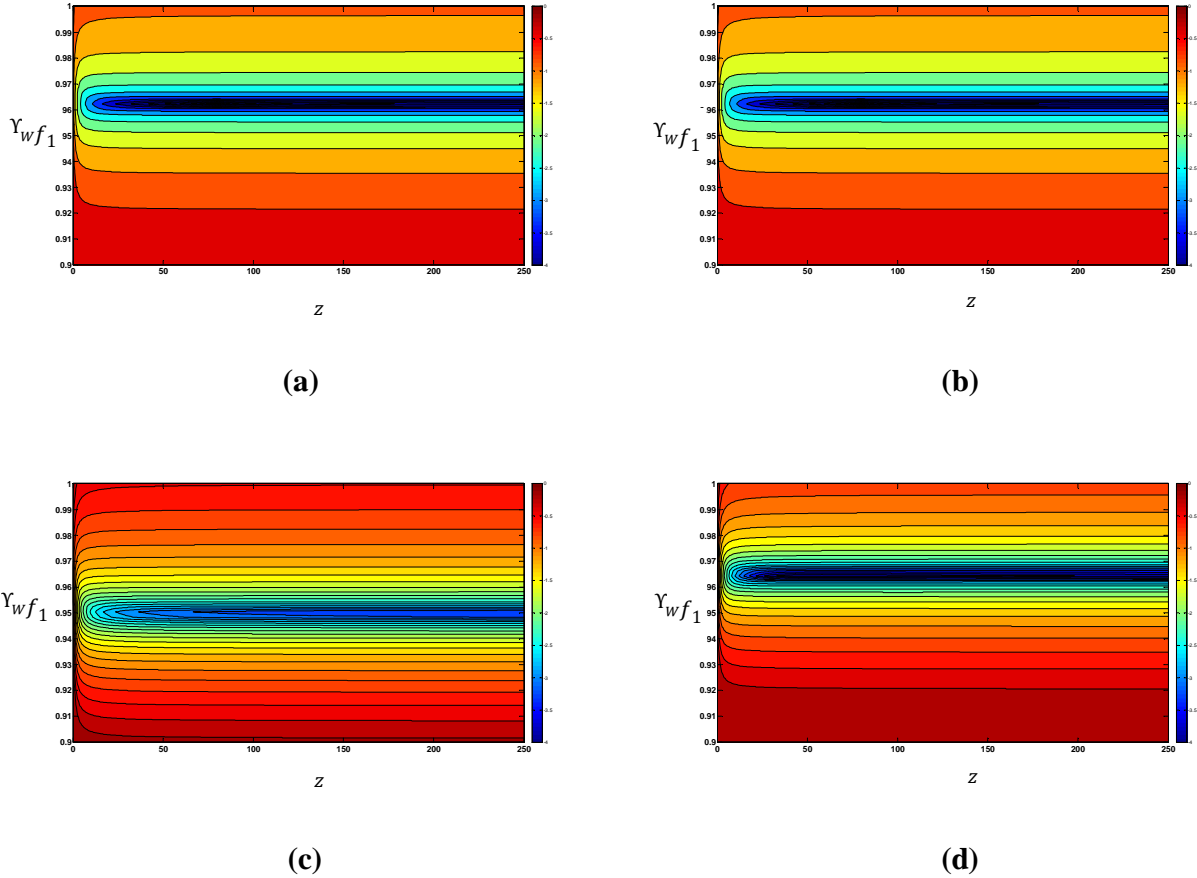


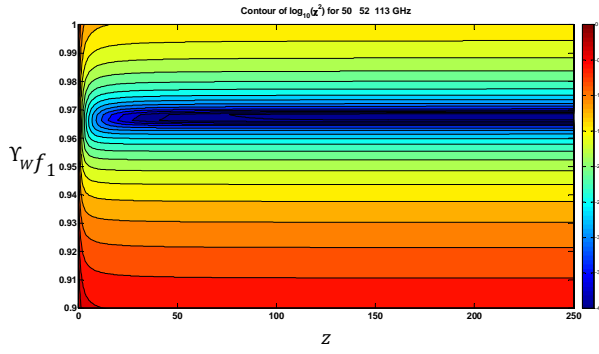
Fig. 3-6: 52.8 91.655 150 GHz cost function contours with constant simulation parameters $T_m=285$ K, and e_m is frequency dependent and calculated using [17], where the actual transmissivity for each case is $Y_{wf_1}=0.9597$. The parameters which vary are: (a) $T_n=290$ K, $e_n=0.95$, $T_{atm}=277.27$ K, (b) $T_n=290$ K, $e_n=0.95$, $T_{atm}=277.27$ K (c) $T_n=270$ K, $e_n=0.95$, $T_{atm}=260$ K (d) $T_n=290$ K, $e_n=0.85$, $T_{atm}=277.27$ K

It is worthwhile to note that each contour had approximately the same shape; a relatively flat area with a trough at the transmissivity which provided the lowest values of the cost function. In order to compare the contours to one another, it is useful to consider the steepness of the trough and the range of transmissivities that the trough could cover. A trough which is very narrow and takes values less than a cost function tolerance, ϵ , around a single transmissivity would likely perform better than a one whose trough was spread across a wider range of transmissivities where the cost function was less than the threshold value. The value of ϵ chosen for the contour

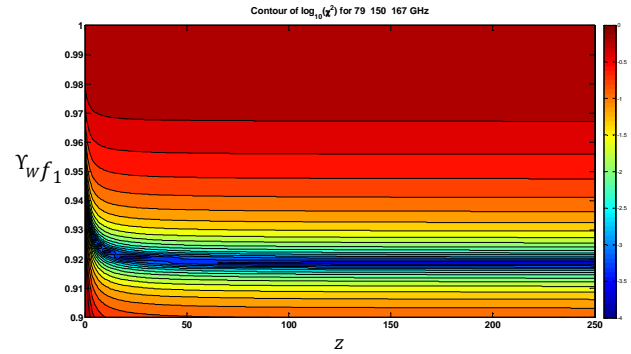
analysis is 10^{-4} . To investigate the impact of changing the emissivities, surface temperatures, and the lumped parameter z (through the atmospheric physical temperature), we simulated 4 cases in which these changes occurred. The results of this simulation are shown in Fig. 3-6a-d.

The trough in Fig. 3-6 is steep for z values greater than 25 for the four test cases near the transmissivity that provides a minimum. This indicates that this frequency set provides acceptable immunity to variation in the simulation parameters when the retrieval bias is small, as shown in Fig. 3-6 a, b, and d, in which cost function contours show little change with changing mean atmospheric temperature and surface emissivities. However, in Fig. 3-6 c, a change in the scene temperature T_n significantly increases the retrieval error. This error is incurred because the difference in the physical temperature of the two surface scenes (approximately 15 K) is too large to be absorbed into the z parameter. As such, very large differences in scenes will cause retrieval errors. In conclusion, the algorithm's performance is not strongly dependent on varying atmospheric temperature T_{atm} or the emissivity of the scenes, e_m and e_n , provided that the two scenes are contrasting. Namely, the BTDR method is designed to provide accurate retrievals only for contrasting scenes, such as land-water boundaries.

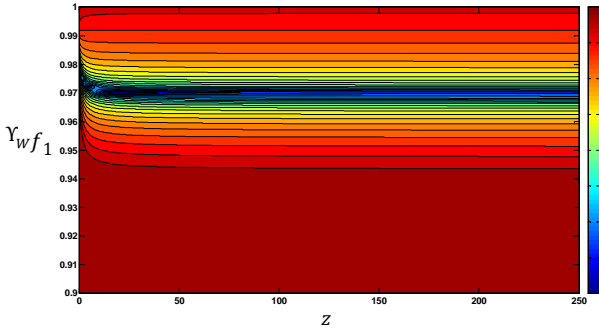
Now that the SSMIS frequency set has been analyzed, similar comparisons can be made used the other three frequency sets which are mentioned in the beginning of this section. By examining Fig. 3-7, one can see how the cost function behavior on the minimization space changes when different frequency sets are chosen.



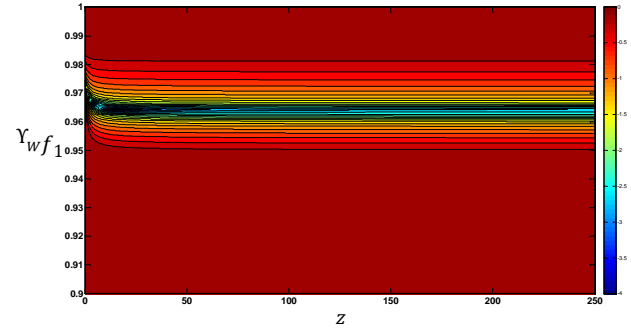
(a)



(b)



(c)



(d)

Fig. 3-7: Cost function contours for a) 50, 52, and 113 GHz, b) 79, 150, and 167 GHz, c) 47, 126, and 153 GHz, and d) 52, 128, and 168 GHz with simulation parameters $T_m=285$ K, $T_n=290$ K, $e_n=0.95$, $T_{atm}=277.27$ K. The water emissivity, e_m , is based on the frequency dependent model from [17] and values are not shown. The simulated transmissivity values for the contours are a) $Y_{Wf_1}=0.96333$, b) $Y_{Wf_1}=0.91568$, c) $Y_{Wf_1}=0.9669$, and $Y_{Wf_1}=0.96207$. The difference in simulated transmissivity values is due different frequency channel choices for f_1

In Fig. 3-7, one frequency set from the HAMSR instrument is shown with three possible frequency set choices from the frequency selection study in Section 3.2. For each of the choices based on Section 3.2, the trough for the cost function minimum is much steeper than the HAMSR frequency set. However, the transmissivity bias (the difference between the simulated and retrieved transmissivity) for the 79, 150, and 167 GHz frequency set, shown in Fig. 3-7b, is higher than any of the contours in Fig. 3-7 indicating higher bias in the retrieved wet path delay. Both Fig. 3-7c and d have very little transmissivity bias and would therefore be the most promising candidates according to contour analysis to further examine for a new instrument design. Since Fig. 3-7d seems to have the most narrow trough, it would likely give a retrieval with lower uncertainty than Fig. 3-7c for a given value of ϵ .

By considering Fig. 3-6 and Fig. 3-7, it can be seen that in each case there is very little dependence on the lumped parameter z , meaning that atmospheric conditions other than those modeled by the BTDR model would likely not affect the retrieval error. This indicates that the retrieval algorithm would perform well regardless of atmospheric conditions. At present, clouds, wind speed, and other error sources are considered to be included in the z parameter since it provides an additional degree of freedom to adjust the transmissivity value based on such unmodeled parameters. The sensitivity of the retrieval to small perturbations can be further examined by observing the effect of noise on the retrieval accuracy. To account for retrieval uncertainty due to noise, in the next section we present a statistical simulation of the retrieval algorithm assuming noisy measurement channels.

3.4: General Noise Analysis

The next step in understanding errors in the BTDR retrievals is to analyze the retrieval performance in the presence of noise to study the behavior of the BTDR algorithm when unmodeled changes are present in the brightness temperatures used for retrieval. Additionally, one may also consider such an analysis to include factors, such as wind speed and presence of clouds,

which may cause changes in the surface emissivity and temperature as well as the atmosphere. The noise characteristics of the BTDR method are examined using two types of analysis. The general characteristics of the retrieval bias and spread of the retrieval values are studied using an aggregate statistical of the retrieval results.

To simulate this situation, a statistical noise analysis was performed in which Gaussian noise with $\sigma_{noise} = 0.1$ K and $\sigma_{noise} = 0.5$ K was introduced to each frequency's brightness temperature. This is done for each frequency channel using 35 bins of wet path delay ranging from 1 to 35 cm, assuming the same number of wet path delay values in each bin. To ensure that the distribution of simulated brightness temperature data was Gaussian for each frequency in the set, a large number of samples for each wet path delay bin are used. For each of these sets of simulated brightness temperature measurements, the cost function was evaluated over the range of Y_{Wf_1} was from 0 to 1 and the range of z from 0 to 250 and the minimum was computed. After the minimum was found, the transmissivity model was inverted to obtain the corresponding wet path delay. The transmissivity inversion is accomplished by calculating transmissivity, Y'_{Wf_1} , for wet path delay values, WPD' , ranging from 0 to 35 cm [9]. The transmissivity found by the cost function minimization, \tilde{Y}_{Wf_1} is then mapped to the closest value of Y'_{Wf_1} and the corresponding wet path delay, \widetilde{WPD} , is obtained. In Fig. 3-8, the histograms for $\sigma_{noise} = 0.1$ K are shown.

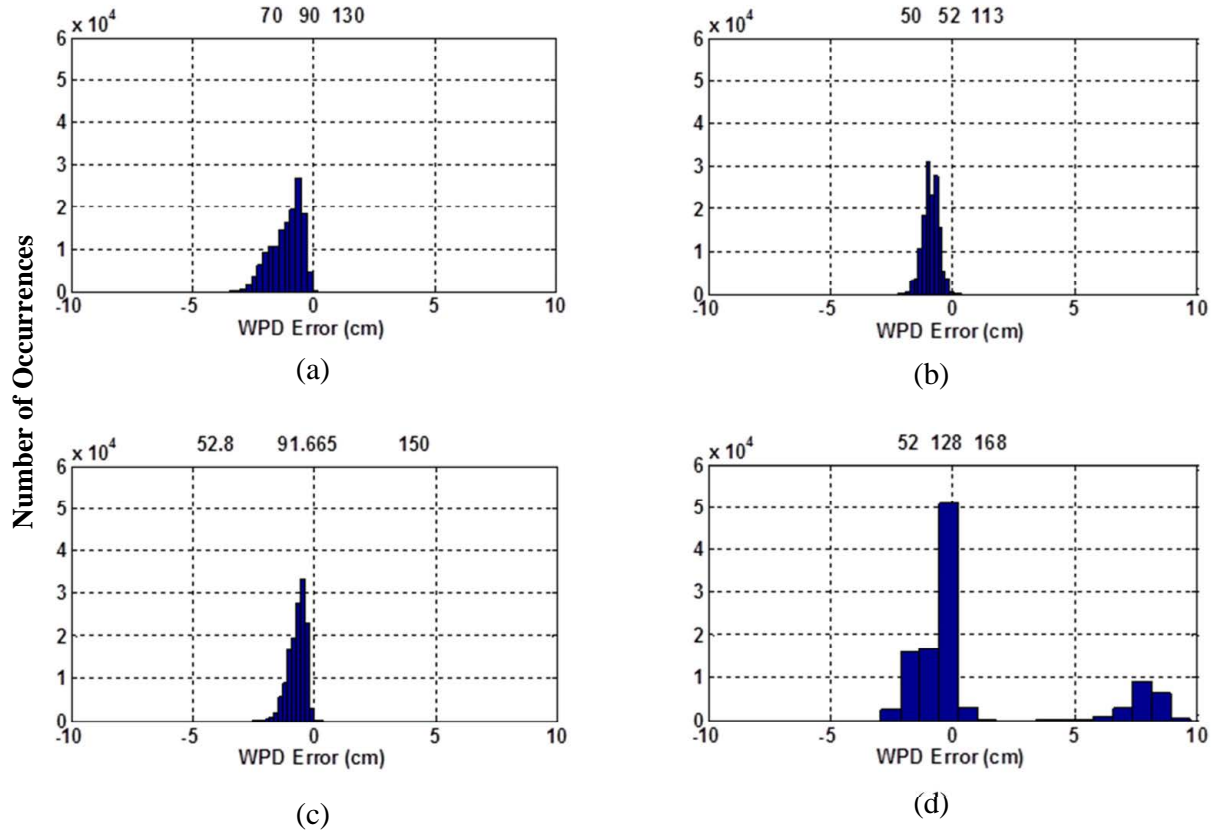


Fig. 3-8: Histograms of wet path delay error assuming $\sigma_{noise} = 0.1$ K for the a) 70, 90, and 130 GHz, b) 50, 52, and 113 GHz; c) 52.8, 91.665, and 150 GHz; and d) 52, 128, and 168 GHz sets.

By comparing the histograms in Fig. 3-8a through c, one can see that the retrievals from these frequency sets are roughly Gaussian distributed where histograms a and c have left skew. The means for of histograms a) through c) are -1.12, -0.89, and -0.69 cm, respectively. The standard deviation of these histograms is 0.19, 0.19, and 0.20 cm, respectively. The histogram shown in d has two modes. The primary mode has mean and standard deviation of -0.62 cm and 0.74 cm whereas the secondary mode has mean and standard deviation of 7.85 cm and 0.66 cm. Due to the bi-modal nature of this frequency set's results, it is likely not a very useful candidate to consider for performing BTDR based wet path delay retrievals since the results from measured retrievals could be difficult to interpret. With this analysis in mind, the best behaved frequency set given for $\sigma_{noise} = 0.1$ K, is the 52.8, 91.665, and 150 GHz shown in c which corresponds to

the SSMIS frequency channels. In order to determine how the retrieval error changes when a larger amount of noise is present, the same simulations were performed where $\sigma_{noise} = 0.5$ K. Histograms for these simulations are shown in Fig. 3-9.

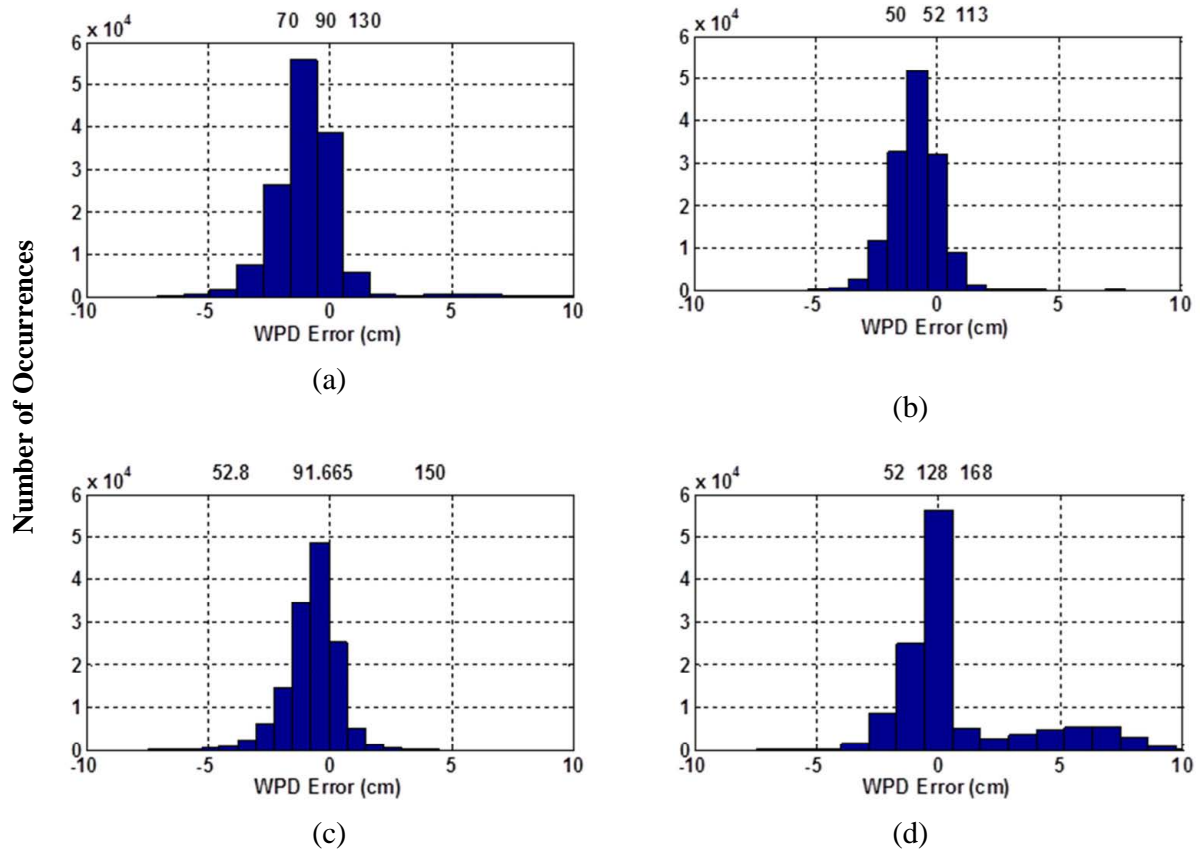


Fig. 3-9: Histograms of wet path delay error assuming $\sigma_{noise} = 0.5$ K for the a) 70, 90, and 130 GHz, b) 50, 52, and 113 GHz; c) 52.8, 91.665, and 150 GHz; and d) 52, 128, and 168 GHz frequency set.

In Fig. 3-9, the histograms for $\sigma_{noise} = 0.5$ K are shown. In this case, the number of bins has remained the same, however the sizing of the bins has changed due to the larger range of error values than shown in Fig. 3-10. The distributions in Fig. 3-9a, b, and c are fairly symmetric, with a slight negative bias. These distributions have means of -0.98, -0.89, and -0.71 cm with standard deviations of 1.25, 0.91, and 1.00 cm, respectively. The distribution in Fig. 3-9d appears to be bi-modal, with the primary mode centered at -0.46 cm and the secondary mode centered around 5.73 cm. The standard deviations of the primary and secondary modes are 0.94 and 1.71 cm,

respectively. Due to the bi-modal nature of this frequency set's results, it is likely not very useful for performing BTDR based wet path delay retrievals since the results from measured retrievals could be difficult to interpret. As an ending note for this analysis method, it can be seen that the bias is overall unchanged by the increase in noise level. Furthermore, an increase in the amount of noise from 0.1 to 0.5 K resulted in an increase in the standard deviation of the retrieval distribution by a factor of 5, proportional to the increase in the introduced noise.

The second analysis method again focuses on the retrieval bias and standard deviation, with the latter representing the retrieval uncertainty with respect to particular wet path delay values rather than for the set of all wet path delay values. The mean and standard deviation of the retrieval error are examined to determine the dependence of BTDR retrieval error on wet path delay. Fig. 3-10 shows the results of this analysis with $\sigma_{noise} = 0.1$ K for the same four frequency sets as those shown in Fig. 3-9.

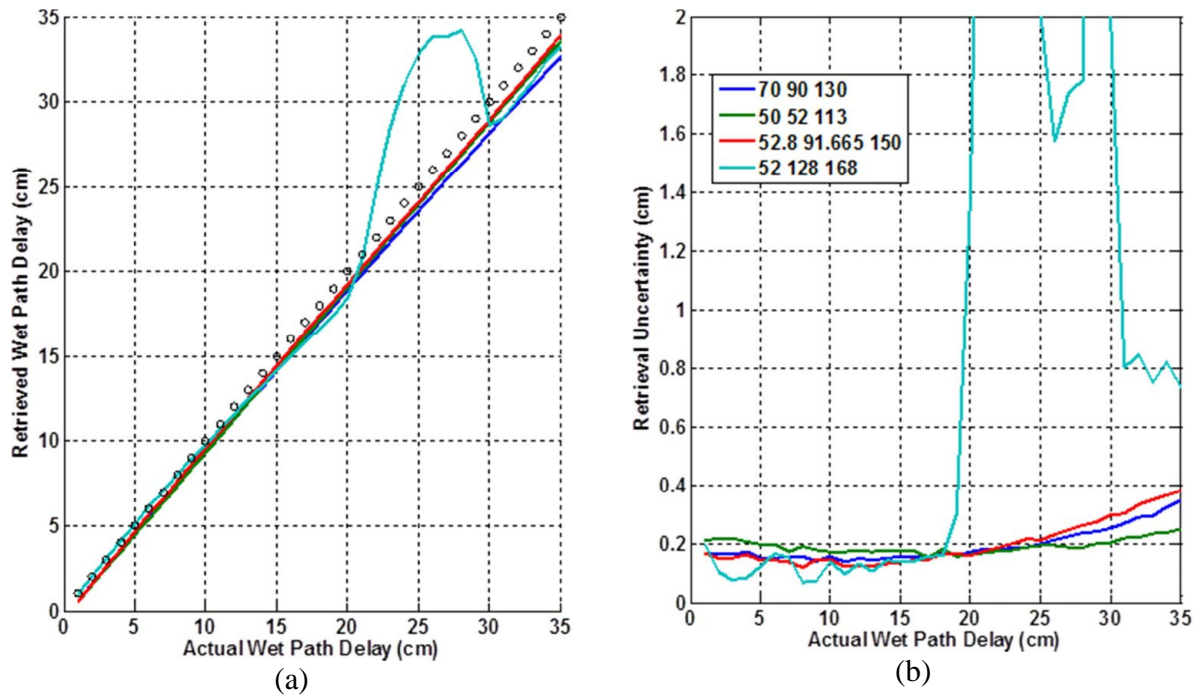


Fig. 3-10: Comparison of the a) retrieval bias and b) retrieval uncertainty for the 70, 90, and 130 GHz; 50, 52, and 113 GHz; 52.8, 91.665, and 150 GHz; and 52, 128, and 168 GHz sets with $\sigma_{noise} = 0.1$ K with respect to the actual wet path delay for the simulated atmosphere.

As shown in Fig. 3-10a, the four frequency sets under examination have approximately the same retrieval bias for 0 to 15 cm wet path delay. For larger wet path delay, the 52, 128, 168 GHz frequency set has a large positive bias for 15 to 30 cm which decreases toward the end of the simulation range of 35 cm. The remaining three frequency sets maintain approximately the same bias above 15 cm wet path delay, with increasing bias as the wet path delay increases. The 50, 52, and 113 GHz and 52.8, 91.665, and 150 GHz frequency sets have less bias than the 70, 90, and 130 GHz frequency set by approximately 0.5 to 1 cm in the 25 to 35 cm wet path delay range. As shown in Fig. 3-10b, the measurement uncertainty is low, below 1 cm for all but the 52, 128, and 168 frequency set. For wet path delay values greater than 17 cm, the retrieval bias of

the 52, 128, and 168 GHz frequency set is quite large and can be attributed to the secondary mode of its histogram. In Fig. 3-11, similar results are shown for $\sigma_{noise} = 0.5 K$.

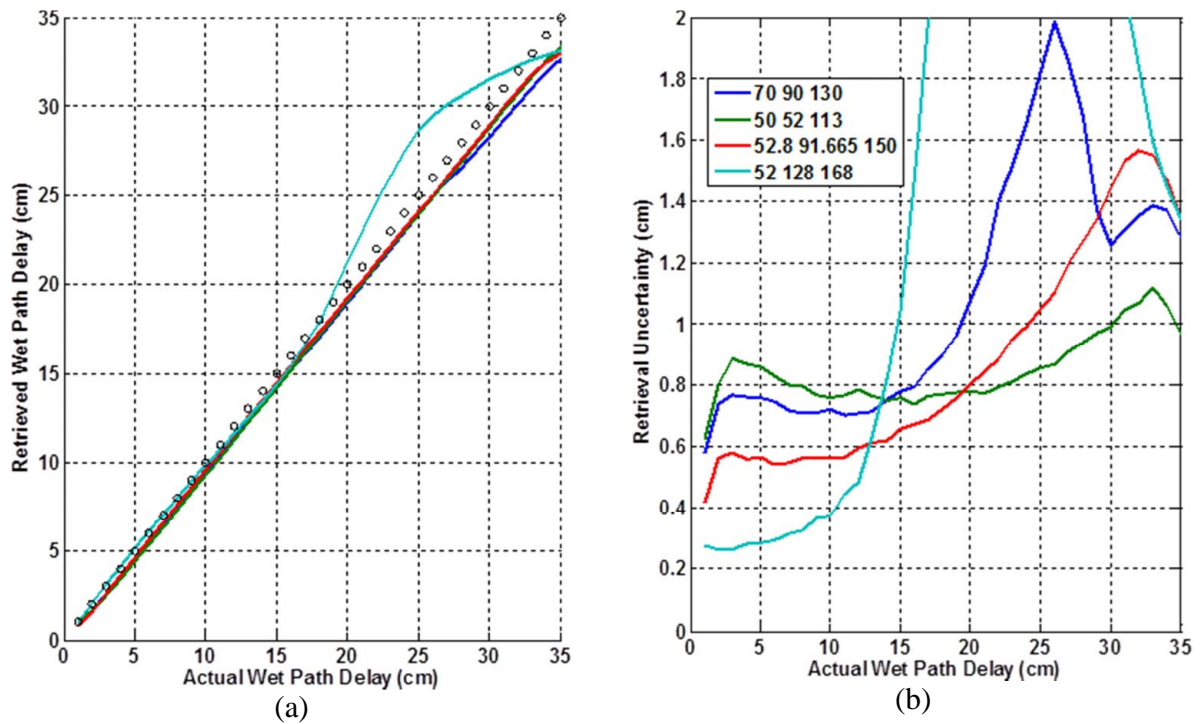


Fig. 3-11: Comparison of the a) retrieval bias and b) retrieval uncertainty for the 70, 90, and 130 GHz; 50, 52, and 113 GHz; 52.8, 91.665, and 150 GHz; and 52, 128, and 168 GHz sets with $\sigma_{noise} = 0.5 K$ with respect to the actual wet path delay for the simulated atmosphere.

Similar to Fig. 3-10, the bias for all frequency sets except for 52, 128, and 168 have approximately the same bias throughout the wet path delay range. The bias for the 52, 128, and 168 GHz frequency set is less than 2 cm except for in the range of 20 to 32 cm. In this area, the secondary mode from Fig. 3-9d can be seen, showing retrieval bias from 2 to 5 cm. The retrieval uncertainty for the 70, 90, and 130 GHz frequency increases rapidly up to 25 cm wet path delay whereas the 52.8, 91.544, and 150 GHz frequency set increases less rapidly up to 32 cm wet path delay. The retrieval uncertainty for the 52, 128, and 168 GHz frequency set is low up to 17 cm

wet path delay but is high and larger wet path delay values. Similar to before, the effects of the primary mode from Fig. 3-9d can be seen in the 1 to 17 cm range and the effects of the secondary mode can be seen from 20 to 32 cm. In summary, the second analysis method in general confirms the result from the first. The bias is relatively unchanged while the retrieval uncertainty increases by an amount approximately equal to the increase in noise level. An increased effect on the retrieval uncertainty can be seen with increasing wet path delay.

Following these comparisons, it is useful to consider how these results may vary when using measured data from actual radiometers, i.e. including bandwidth in the simulations. In particular, the currently available radiometer data limits the retrieval algorithm's testing to using the 50, 52, and 113 GHz frequency set from the HAMSR radiometer and the 52.8, 91.665, and 150 GHz frequency set from SSMIS. Up to this point, the issue of bandwidth has not been considered. Since measurements from any instrument will not be at a single frequency, we shall inspect the effects of bandwidth on the retrieval performance through a similar analysis described in Section 3.5.

3.5: Radiometer Noise Analysis

Up to this point, the impact of bandwidth has not been considered. Since measured data will have non-zero bandwidth, the effects of bandwidth on the retrieval performance were considered using a similar analysis to that of this section. In the previous analysis, each of the radiometer channels has been assumed to operate at only a single frequency. It is worthwhile to consider the effects of realistic bandwidths for the radiometer channels and in turn the effects on the retrieval accuracy. In particular, we would like to examine the tradeoff between radiometer bandwidth and radiometric resolution. Small radiometer bandwidths enable the use of highly accurate transmissivities, but cause increased radiometric resolution, increasing the instrument noise. To accomplish this, we use the radiometric resolution, of an ideal total power radiometer (10) with no gain fluctuations, system temperature, T_{sys} , bandwidth, β , and integration time, t [8].

$$NE\Delta T = \frac{T_{sys}}{\sqrt{\beta t}} \quad (10)$$

The relationship of $NE\Delta T$ with respect to bandwidth for a system temperature of $T_{sys} = 2000$ K and an integration time of 20 ms, typical for space-borne millimeter-wave radiometers such as SSMIS [24]. The $NE\Delta T$ and bandwidth tradeoff is shown in Fig. 3-12 for a total power radiometer with the aforementioned specifications for various bandwidths.

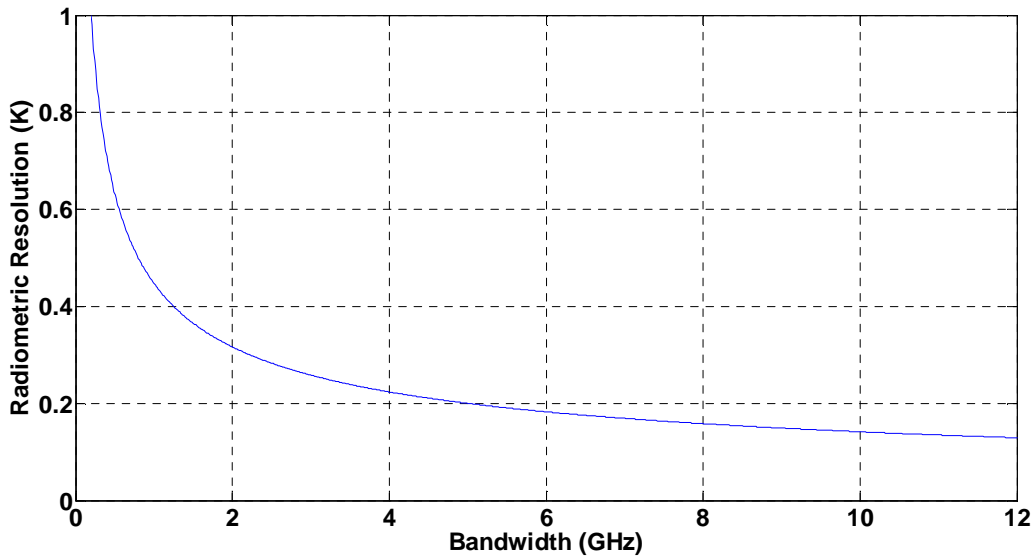


Fig. 3-12: Radiometric resolution with respect to bandwidth for $T_{sys}=2000$ K and $t=0.02$ s

In order to analyze the effects of changing bandwidths on the BTDR retrievals, we will perform retrievals using bandwidths ranging from 0.1 to 4 GHz for the simulations and compute the mean and standard deviation of the introduced noise based on the total power radiometer radiometric resolution.

Using this setup, we shall perform retrievals using the bandwidth in a manner similar to Section 3.4 using the radiometric resolutions determined according to total power radiometers as the standard deviation of the introduced noise. This will introduce bias into the retrieval due to the integration of brightness temperatures over the bandwidth as well as measurement uncertainty from the instrument noise. The results from this simulation are shown in Fig. 3-13.

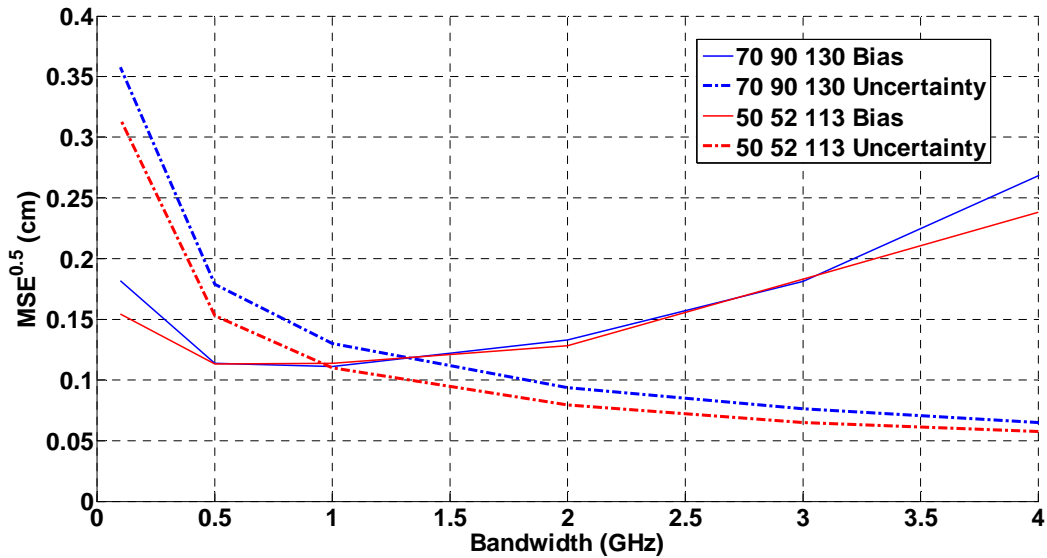


Fig. 3-13: Comparison of the mean squared error of both the mean and standard deviation of the retrieval error for the 70, 90, and 130 and 50, 52, 113 and GHz sets

As can be seen, a tradeoff between the bandwidth of the radiometer channels and the retrieval bias and uncertainty exists. Bandwidths can be chosen based on a compromise between minimizing the mean and the standard deviation of the mean squared error of the retrievals. In this case, it is more desirable to have a larger bias but low uncertainty in the retrieved value. In both of the sets studied it should be noted that between 0 to 4 GHz the results are approximately the same. However, since the 50, 52, and 113 GHz frequency set contains two frequencies that are close to each other, bandwidths greater than 4 GHz for this case yielded unacceptably high retrieval error and are not shown, leaving yet another option for consideration in choosing a set of frequency channels for wet path delay retrieval.

To further discuss the notion of bandwidth with the BTDR method, a similar simulation to Fig. 3-10 and Fig. 3-11 was performed using instrument specifications from both HAMS and SSMIS. This enables a better understanding of which instrument is likely to provide the better results. Additionally, this study can give a general idea of the retrieval error when using measured data from either instrument. The retrieval bias and uncertainty are shown as a function

of wet path delay assumed for the simulation, for the 50, 52, and 113 GHz frequency set from HAMSR and the 52.8, 91.655, and 150 GHz frequency set from SSMIS in Fig. 3-14.

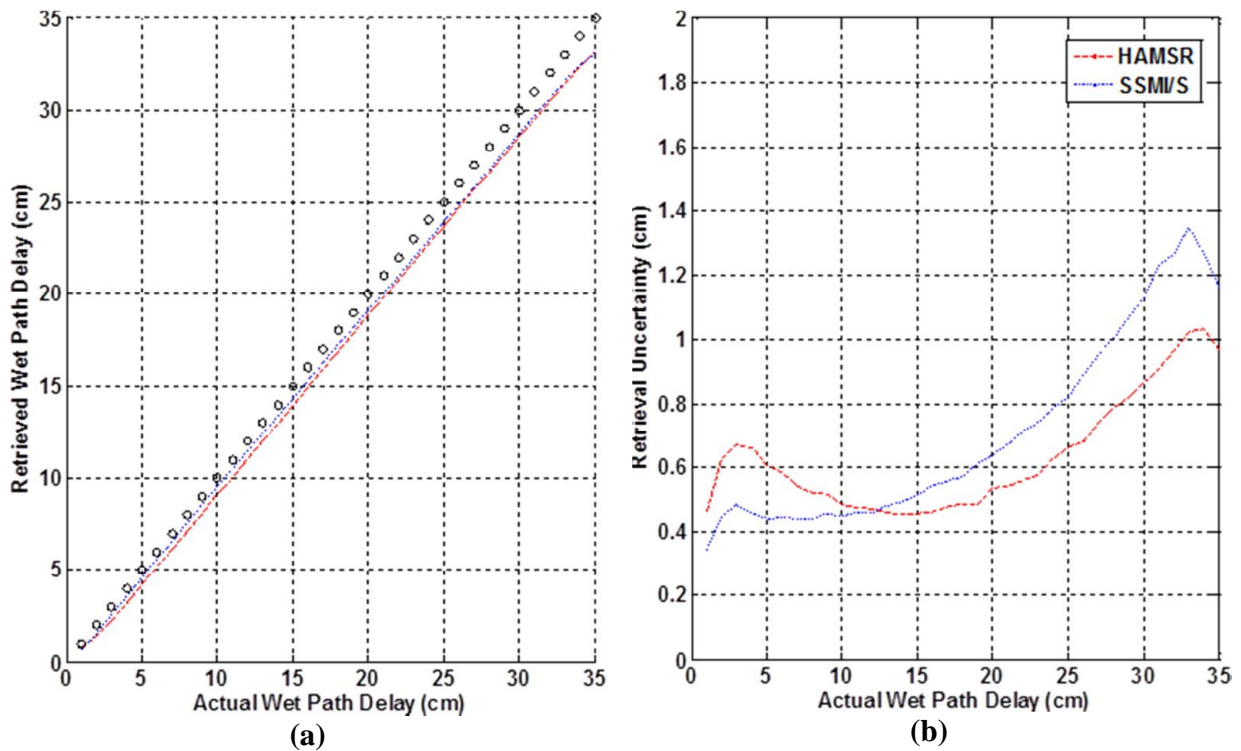


Fig. 3-14: Comparison of HAMSR and SSMIS retrievals using the BTDR method. The frequency set used for HAMSR was 50, 52, and 113 GHz and the set for SSMIS was 52.8, 91.655, and 150 GHz. The measurement bias can be seen in (a) and the measurement uncertainty in (b).

The retrieval bias for the frequency sets from both instruments is essentially the same, with the retrievals from the SSMIS frequency having slightly less bias; particularly in the low to mid wet path delay regions. Both instruments have increasing bias with increasing wet path delay, with a maximum bias of 2 cm at wet path delay of 35 cm. However, from 10 to 28 cm wet path delay, the retrieval bias is 1 cm or less. In all cases, the bias is negative, meaning that all of the simulated wet path delay retrievals underestimated the actual value. The retrieval uncertainty of both of the frequency channel sets chosen for the instruments has similar behavior as a function of wet path delay. The SSMIS retrieval uncertainty increases monotonically with respect to the

wet path delay from approximately 5 to 32 cm; whereas, the HAMSR retrieval uncertainty has an inflection point around 15 cm, above which it increases monotonically. Additionally, the SSMIS retrieval uncertainty exceeds 1 cm above approximately 27 cm wet path delay, but the HAMSR uncertainty is below 1 cm. The retrieval uncertainty for both instruments has decreased from those shown in Fig. 3-11 by included the effects of bandwidth and radiometric resolution of the actual instruments. This is an expected result as the noise level used for the simulations in Fig. 3-11 is quite large.

However, the HAMSR data is limited to a series of aircraft flight campaigns. Additionally, since it is an aircraft based instrument it is not feasible to use it for measuring brightness temperatures on a regular basis. On the other hand, SSMIS provides daily measurements brightness temperature measurements of the globe, allowing a much greater variety in areas which could be used to retrieve wet path delays.

Chapter 4: Wet Path Delay Retrieval: Results from Measured Data

Since the algorithm demonstrated potential in retrieving wet path delay values in the simulations, the next sensible step was to test the algorithm using measured data. In this chapter, retrievals from two instruments, HAMSR and SSMIS, are presented. The HAMSR retrieval is shown as a proof of concept step to see how the algorithm would perform with measured brightness temperatures from an airborne instrument. Following this, the algorithm was applied to satellite data to perform retrievals on a near-global scale. However, before investigating the retrieval results it is important to consider additional sources of error which is present in simulated measurements, as detailed in Section 4.1.

4.1: Sources of Retrieval Noise

So far little mention has been made about the nature of the errors seen in the comparisons of Sections 5.1 and 5.2. We will now resolve these issues by identifying the various contributors to the errors from the BTDR retrievals and explain possible methods of mitigation and areas of further study. In general, there are three categories of error which could contribute to uncertainties in the BTDR retrievals. They include un-modeled atmospheric changes, errors due to image processing techniques, and errors due to the retrieval instrument.

The first source of retrieval noise is error resulting from un-modeled atmospheric conditions, such as those discussed in Section 3.2. These include atmospheric changes that are either not modeled by the model deflection ratio or cannot be accounted for by the use of the lumped parameter z . These errors are assumed to be spatially and temporally smooth, meaning that they do not change rapidly between pixels in the brightness temperature image. In order to mitigate errors of this type, updated atmospheric models could be used which more closely describe the atmosphere.

The second source of retrieval noise is image processing errors. This category includes both errors from the detection of edges and those from the orientation of the detected edges. The edge

detection algorithms identify areas of significant change in the brightness temperature maps produced by the radiometric measurements. As such, edge detection in moist atmospheres is more difficult than in dry atmospheres since areas in which large amounts of water vapor are present will appear nearly homogeneous, regardless of the surface conditions. Therefore, fewer retrievals are available for these regions and higher retrieval error is expected in regions with large amounts of water vapor, as seen in Section 3.4. However, using edge detection methods that are more suitable for detecting subtle changes, such as the Canny method [20], may be more useful than the Sobel method in these cases. Conversely, the Canny method may increase false positive identification of land/water boundaries. A possible solution is to segment the image based on a prior TPW retrieval and then use Sobel method for the drier and Canny for the wetter atmospheric conditions. An example of this type of image processing error is shown in Fig. 4-1.

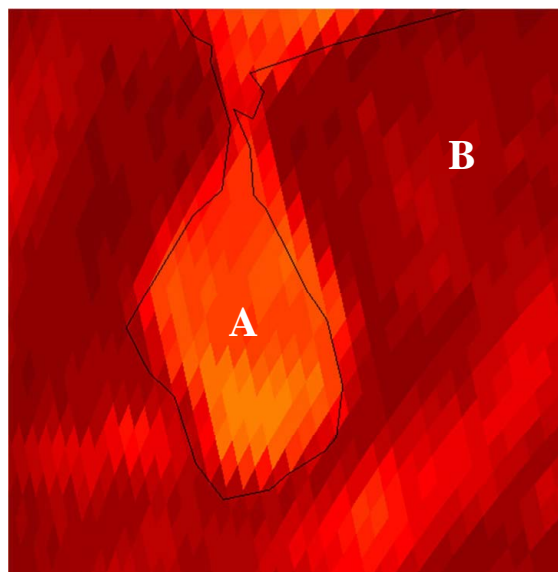


Fig. 4-1: Illustration of image processing errors due to detection of edges. The boundary for the water (shown by A) and the land (shown by B) is blurred due to the high concentration of water vapor in the atmosphere.

The second type of error due to the image processing is lack of alignment of coastlines with the axes of the image grid. This could lead to an error in identifying which two pixels should be used for the retrieval. Namely, when two nearby pixels are compared, one needs to be on each

side of the coastline, i.e. one on land and the other on water. When this condition is not met, the wet path delay retrieval is invalid since both of the pixels which are used to compute the wet path delay are from the same surface type, either both land or both water. An example of this type of image processing error is shown in Fig. 4-2.

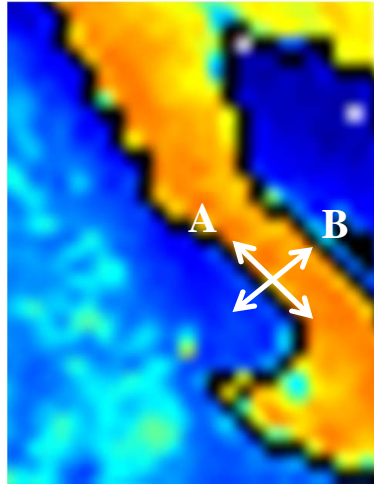


Fig. 4-2: Illustration of image processing errors due to grid and coastline alignment. In this image, if the retrieval is taken along the line labeled A, the assumptions of the land/water pixels mentioned in Chapter 2 is violated. If the retrieval is taken along the line labeled B, the assumptions of the model are valid and a retrieval can be performed.

The third source of retrieval noise is instrument errors from the radiometer. These errors are due to calibration, linearity, radiometric resolution ($NE\Delta T$), antenna pattern, etc. The BTDR retrieval algorithm does not include mitigation of instrument errors. As such, instrument errors including measurement bias and uncertainty, will affect the retrieved wet path delay. This emphasizes the need for better calibration methods and lower noise radiometers to reduce errors in brightness temperature measurements. In particular, retrieval noise of the BTDR method depends on the radiometer used to measure brightness temperatures.

4.2: HAMSR Retrieval Results

As a proof of concept, retrievals were performed using measurements from a HAMSR overpass above the Saint John's River in Florida. The instrument was flown on board a NASA Global Hawk UAV for the Genesis and Rapid Intensification Processes (GRIP) field experiment, in which its purpose was to retrieve the three dimensional temperature, water vapor, and cloud liquid water profiles. The instrument has 25 frequency channels and originally was designed to be similar to the Advanced Microwave Sounding Units (AMSU). The frequency channels of the HAMSR instrument include eight sounding channels near the 60-GHz oxygen absorption complex, ten channels near the 118.75 GHz oxygen absorption line, and seven channels near the 183.31 GHz water vapor absorption line [23]. The details of the frequency channels are shown in Table 4-1.

Table 4-1: Description of the frequency channels available from the HAMSR instrument from [23]. The W_1 and W_2 entries are weighting factors for the lower and upper sidebands, respectively.

Channel	f_c – LSB [GHz]	BW – LSB [MHz]	W_1	f_c – USB [GHz]	BW – USB [MHz]	W_2
1	50.30	185.34	-	-	-	-
2	51.81	456.26	-	-	-	-
3	52.82	444.60	-	-	-	-
4	53.46	151.29	0.58	53.69	155.73	0.42
5	54.41	446.50	-	-	-	-
6	54.94	442.91	-	-	-	-
7	55.46	374.80	-	-	-	-
8	55.99	279.05	0.90	56.61	235.84	0.10
9	113.27	1062.11	-	-	-	-
10	115.19	1060.03	-	-	-	-
11	116.18	506.09	-	-	-	-
12	116.70	504.33	-	-	-	-
13	117.13	432.13	-	-	-	-
14	117.54	418.95	-	-	-	-
15	117.93	459.60	0.54	119.56	424.56	0.46
16	118.30	319.84	0.54	119.19	302.38	0.46
17	118.50	117.19	0.47	118.98	140.74	0.53
18	118.61	100.86	0.42	118.86	105.95	0.58
19	166.95	3812.82	-	-	-	-
20	173.22	3298.97	0.54	192.88	2926.96	0.46
21	176.26	2409.16	0.34	190.23	2472.45	0.66
22	178.74	2133.24	0.23	187.95	2162.90	0.77
23	180.39	1093.10	0.29	186.32	1119.17	0.71
24	181.44	1157.75	0.36	185.09	1109.80	0.64
25	182.30	536.28	0.27	184.31	539.22	0.73

Of the 25 channels available from the HAMSR instrument, channels 1, 2, and 9 provided the most promising frequency set for BTDR retrievals in initial simulations and according to several selection criteria detailed in Chapter 3. These channels correspond approximately to the frequency set 50, 52, and 113 GHz and will be labeled as such in the following analysis.

The flight path which the Global Hawk took in order to allow HAMSR's measurements took off from the Meadows Field Airport in Bakersfield, CA airport and flew across the United States to a location over the Atlantic Ocean to measure the thermodynamic atmospheric state of a hurricane in that area. As part of this flight, an overpass of a wide river in Florida, the Saint John's River, occurred. This area provided a good test retrieval location for the BTDR method using HAMSR's calibrated brightness temperature measurements. A map of the specific retrieval area with respect to the continental United States is shown in Fig. 4-3:

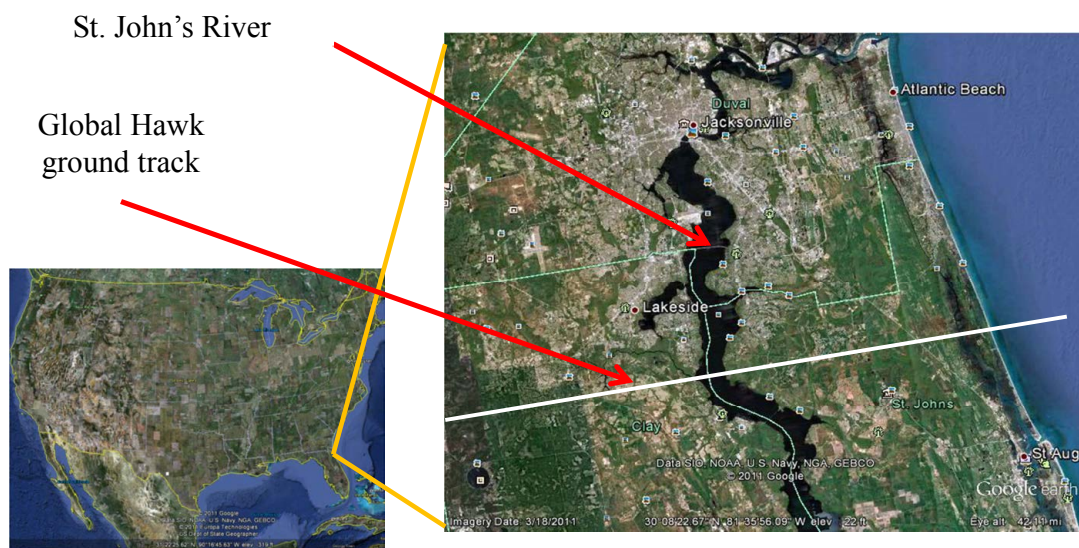


Fig. 4-3: Illustration of the ground track of HAMSR aboard the NASA Global Hawk unmanned aircraft over the Saint John's River.

Prior to performing the retrieval, looking at the measured brightness temperatures from the instrument can give an idea of where the algorithm could be used and estimates of the results can be made. Specifically, by observing the input before turning to the results, one can get a better idea of the detection of water vapor, regardless of the amount, before attempting to retrieve the actual wet path delay in the area. In short, doing this can tell us if the BTDR algorithm can actually detect a change present within the data. The measured brightness temperatures along the track shown in Fig. 4-3 are shown in Fig. 4-4.

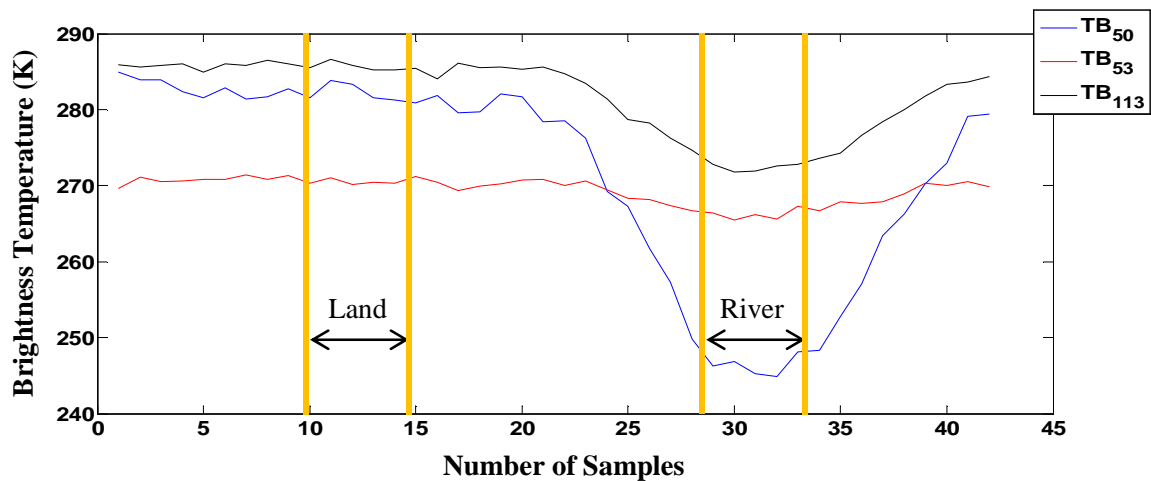


Fig. 4-4: Brightness temperature measurements taken by HAMSR over the St. John’s River in Florida for September 1, 2010.

From examining Fig. 4-4, one can see a clear distinction between the land and river measurements for the 50 and 113 GHz channels. This change is most evident in the 50 GHz channel since it has the lowest opacity of the three. The 50 GHz channel has been attenuated slightly due to the higher opacity and its proximity to the 60 GHz absorption complex. Since the 53 GHz channel is fairly close to the 60 GHz absorption complex, the difference in between land and river measurements at 53 GHz is very small and likely could not be detected without the aid of other channels. With that said, this does not imply that the 53 GHz channel is not at all useful to the retrieval. Moreover, it provides a baseline from which one can judge the amount of water vapor in the atmosphere since the 60 GHz absorption complex is mostly due to oxygen absorption and therefore, the attenuation in the 53 GHz channel is due to mostly to oxygen rather than water vapor. In a practical sense, performing the retrieval with the BTDR algorithm is performed by using the labeled land and river scenes in Fig. 4-4 to obtain contrasting scenes. In this case, this can be viewed as an acceptable practice since the goal of the HAMSR retrieval is to show that the BTDR algorithm can retrieve atmospheric water vapor, in the form of wet path delay, when it is applied to measured data from a radiometric receiver. To transition to a more

operational retrieval, the selection of land and water targets requires a further level of automation, such as the edge detection method described in Chapter 2.

Before discussing the retrieval results, it is necessary to explain the independent data to which they are compared. For this comparison, the National Oceanic and Atmospheric Administration (NOAA) National Operational Model Archive and Distribution System's (NOMADS) weather model database was used. The product provided by NOMADS that is used for comparison to the BTDR retrieved wet path delays is in the form of total precipitable water and were obtained from the Service Records and Retention System (SRSS) analysis and forecast charts [25]. In order to provide a comparison to the BTDR retrievals, this product needs to be converted to a wet path delay value by using methods such as [21].

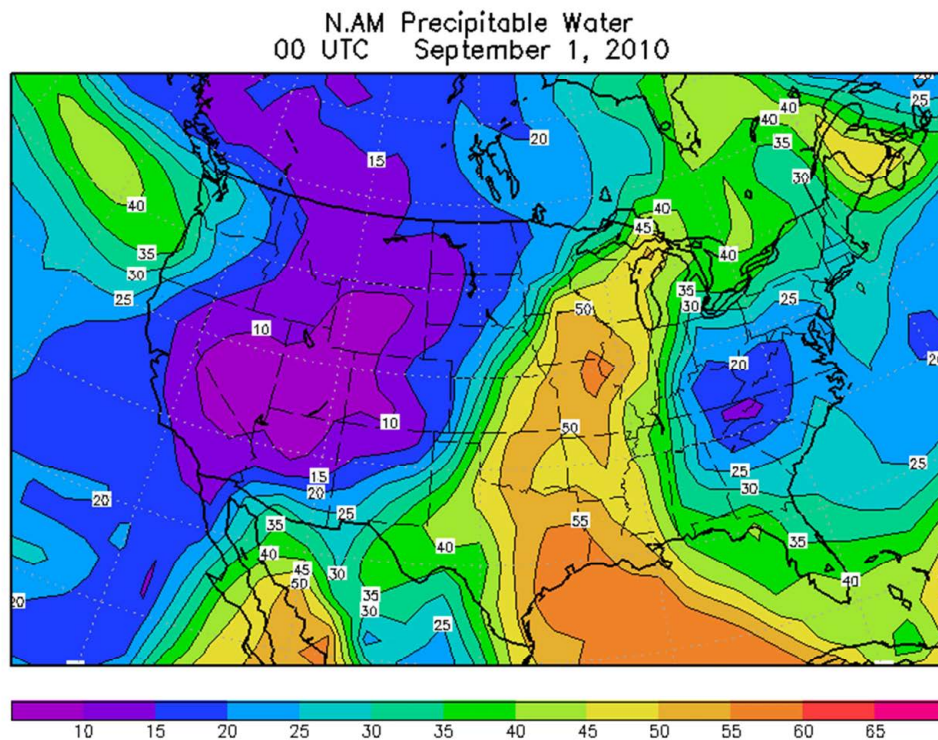


Fig. 4-5: Map of NOMADS predicted total precipitable water values for September 1, 2010; the date of the HAMSR based BTDR retrievals

Now that the source of independent measurements for comparison to the HAMSR retrievals has been identified, one can continue to perform the retrievals using the BTDR method on the shorelines of the Saint John’s River. The retrievals were performed using the brightness temperatures indicated in Fig. 4-4 and the results from this retrieval as well as the converted NOAA NOMADS prediction is shown in Table 4-2.

Table 4-2: Comparison of the BTDR retrievals using HAMSR measured brightness temperatures and the converted total precipitable water predictions from NOAA NOMADS

Data Source	Wet Path Delay (cm)
NOAA NOMADS	22.1
HAMSR with BTDR	23

As can be seen, the retrievals offer very close agreement to the predicted wet path delay value for the date of the retrieval. As the NOMADS predictions are based on past observations as well as current weather modeling, it is likely that they represent an average value for the day and deviations from the average are to be expected. With that said, one can be fairly confident that using the BTDR algorithm to retrieve the wet path delay using microwave and millimeter wave brightness temperature measurements is feasible and can provide useful results.

Now that the algorithm has been presented in a prototype situation using the HAMSR data, one can continue to transition into a more operational, yet preliminary, form by applying the BTDR approach to a wider range of measurements. In order to do this, an instrument which provides reliable measurements on a global scale is preferred as a much wider range of situations can be

tested. For this, the satellite based SSMIS measured brightness temperatures aboard provided a prime opportunity and will be discussed in Section 4.3.

4.3: SSMIS Retrieval Results

The Special Sensor Microwave Imager / Sounder (SSMIS) is a space-borne conically scanning radiometer which has 24 frequency channels as described in [24]. Of these channels, we have chosen to use the 52.8, 91.655, and 150 GHz channels for retrieving wet path delay by the BTDR method. These channels have 0.389, 1.411, and 1.642 GHz bandwidths, respectively, with radiometric resolution of approximately 0.32 K for the two lower frequency channels and 0.89 K for the 150 GHz channel. After processing, the effective footprint of the SSMIS is approximately 17 by 29 km for the 52.8 GHz, 9 by 15 km for the 91.655 GHz and 150 GHz channels. All channels used for the BTDR retrievals use horizontal polarization. Further information concerning the frequency channels included in SSMIS can be seen in Table 4-3 from [24].

Table 4-3: Description of the frequency channels on the SSMIS instrument from [24].

TABLE I
SSMIS SENSOR CHARACTERISTICS (S/N 02) ON DMSP F-16

Channel	Center Freq.(GHz)	3-db Width (MHz)	Freq. Stab.(MHz)	Pol.	NEDT (K)	Sampling Interval(km)
1	50.3	380	10	*V	0.34	37.5
2	52.8	389	10	*V	0.32	37.5
3	53.596	380	10	*V	0.33	37.5
4	54.4	383	10	*V	0.33	37.5
5	55.5	391	10	*V	0.34	37.5
6	57.29	330	10	RCP	0.41	37.5
7	59.4	239	10	RCP	0.40	37.5
8	150	1642(2)	200	H	0.89	12.5
9	183.31+/-6.6	1526(2)	200	H	0.97	12.5
10	183.31+/-3	1019(2)	200	H	0.67	12.5
11	183.31+/-1	513(2)	200	H	0.81	12.5
12	19.35	355	75	H	0.33	25
13	19.35	357	75	V	0.31	25
14	22.235	401	75	V	0.43	25
15	37	1615	75	H	0.25	25
16	37	1545	75	V	0.20	25
17	91.655	1418(2)	100	V	0.33	12.5
18	91.655	1411(2)	100	H	0.32	12.5
19	63.283248 +/-0.285271	1.35(2)	0.08	RCP	2.7	75
20	60.792668 +/-0.357892	1.35(2)	0.08	RCP	2.7	75
21	60.792668 +/-0.357892 +/-0.002	1.3(4)	0.08	RCP	1.9	75
22	60.792668 +/-0.357892 +/-0.0055	2.6(4)	0.12	RCP	1.3	75
23	60.792668 +/-0.357892 +/-0.016	7.35(4)	0.34	RCP	0.8	75
24	60.792668 +/-0.357892 +/-0.050	26.5(4)	0.84	RCP	0.9	37.5

* Channels 1-5 (LAS) were incorrectly designed as V-pol on unit S/N 02. All other SSMIS

Flight units will be configured as H-pol

SSMIS provides brightness temperature measurements for most of the Earth on a daily basis. For the data which we will use for our retrievals, we have chosen to use three different satellites carrying the SSMIS instrument, namely the F16, F17, and F18 Defense Meteorological Satellite Program (DMSP) spacecraft.

Since a requirement of the BTDR method is to have contrast in the background scenes, we will apply the Sobel and Canny edge detection algorithms [19, 20] to the 91.655 GHz channel as it provided a more clear distinction between land and water than either the 52.8 or 150 GHz channels. Additionally, it is worthwhile to discuss the method for computing wet path delay values for the valid pixels. First of all, since the spatial resolution of the 52.8 GHz channel is greater than that of the other two channels used for the retrieval, it was interpolated to the same grid as the 91.655 and 150 GHz channels, which have a grid spacing that is three times as small as the 52.8 GHz channel. After this, two edge detections, one horizontal and one vertical, were performed on the 91.655 GHz channel in order to extract both horizontal and vertical areas of contrast. Retrievals were then performed for both the horizontal and vertical edges and the resulting wet path delays were merged to form the final retrieved wet path delay image. As already mentioned, in order to ensure that only measured data, as opposed to interpolated data, was used for the retrieval, the interpolation distance (a factor of 3) was accounted for in the 52.8 GHz channel. An example of this process is shown in Fig. 4-6.

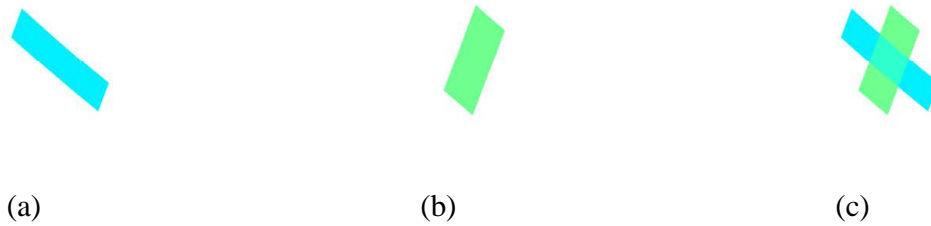


Fig. 4-6: Illustration of (a) horizontally retrieved pixels, (b) vertically retrieved pixels, and (c) the combination of the horizontal and vertical pixels.

As can be seen by the Fig. 4-6, these results in a cross shaped pattern for each retrieval point. If two retrievals are neighboring, their overlapping regions are averaged whereas if there is no data for one of the retrieval directions, the one which contained data is used. This was done in order to account for the varying angles of inclination of the coastlines with respect to the grid formed by the brightness temperature images. As discussed in Section 4.1, this technique is also intended to mitigate the errors incurred due to land/water boundaries which are not aligned with the direction of the brightness temperature image axes. Although these errors are still present, combining both the horizontal and vertical retrievals lessens their impact and provides more consistent final results, as will be discussed in the following sections. However, this technique also has the possibility to add errors should one of the merged pixels due to image processing errors, as discussed in Section 4.1.

Qualitative comparisons with standard wet path delay retrieval products using the (TPW) products are performed. The data for these comparisons comes from the Tropical Rainfall Measuring Mission (TRMM) Microwave Imager (TMI) [26], the Advanced Microwave Sounding Radiometer for Earth Observing System (EOS) (AMSR-E) [27] and SSMIS instruments. The TMI and AMSR-E sensors are included in these comparisons as they have different specifications and characteristics than SSMIS, the instrument which made the BTDR based brightness temperature measurements. The TPW products from all three instruments were

derived using the Goddard PROFiling (GPROF) 2010 algorithm [28, 29] and are converted to wet path delay using the algorithm of Stum et al. [21]. The GPROF 2010 TPW products are available over open ocean to within 50 km of coastlines and over a few of the largest inland water bodies. The BTDR wet path delay retrievals are available only on coastlines and at the shorelines of inland water bodies. Therefore, the BTDR wet path delay retrievals cannot be quantitatively compared with the GPROF 2010 TPW products.

To provide sufficient statistics to characterize the differences among the three data sets, temporally and spatially overlapping measurements are desired. However, since these products are derived from radiometers on different satellites, there are temporal and spatial differences among the SSMIS, TMI, and AMSR-E data sets which lead to errors based on dynamic atmospheric changes. The wet path delay retrievals are examined for three regions: the Caspian and Aral Seas; Arabian Sea; and Chilean and Argentinean coasts. Table 4-4 shows the time of each instrument's overpass of each of these regions on the date of the retrievals, January 1, 2011.

Table 4-4: Comparison of the time of measurement, with a resolution of 5 minutes, in UTC for each of the 3 instruments used for different areas on January 1, 2011

	SSMIS Measurement Time (UTC)	TMI Measurement Time (UTC)	AMSR-E Measurement Time (UTC)
Caspian/Aral Seas	1:35 (F17 D)	11:15 (D)	22:45 (A)*
Arabian Sea	2:00 (F17 D)	7:55 , 9:40 (D)	8:50,10:25 (D)
Chile and Argentina	1:40 (F18 A)	5:30 (A)	5:15, 6:40 (A)

* This later time was chosen as previous measurement times did not provide enough data to obtain a comparison due to the orientation of the AMSR-E orbit.

In order to directly compare the BTDR retrieved wet path delay to the TPW products, we use the conversion found in [21] to translate TPW to wet path delay. Comparisons were performed in three geographic regions in which the BTDR retrievals will be compared to the derived wet path delays from the independent TMI (where available), AMSR-E, and SSMIS retrieved total precipitable water products.

As quantitative error estimate, we will approach the problem from the standpoint of self-consistency of the retrieval results. This approach is taken since there are no geographically or temporally collocated external comparisons available. Specifically, we will apply this approach to connected pixels along coastlines/shorelines which are approximately 200 km in length or longer in order to ensure that the error estimates accurately represent the data set. For now, we will set this analysis aside until Section 5.4 and focus on qualitatively comparing the BTDR retrievals using the SSMIS data to the externally retrieved AMSR-E and TMI retrievals.

4.3.1: Inland Water Retrievals

To address wet path delay retrievals over inland bodies of water, we present retrieval results for the Caspian and Aral Seas between Eastern Europe and Western Asia. Comparisons from both AMSR-E and TMI were available for the area which was chosen, however the TMI measurements over the area are constrained to only the southern portion of the Caspian Sea, as TMI measurements are only available between 38° N and 38° S. It is also worthy to note that there is significant time difference in between the BTDR retrieved wet path delays and the AMSR-E or TMI water vapor products as shown in Table 4-4. The images presented in this section have been filled in to compensate for the grid size of the 52 GHz channel. With this in mind, we present the retrieval results from both AMSR-E and the BTDR method for the Caspian and Aral Seas between Eastern Europe and Western Asia as shown in Fig. 4-7.

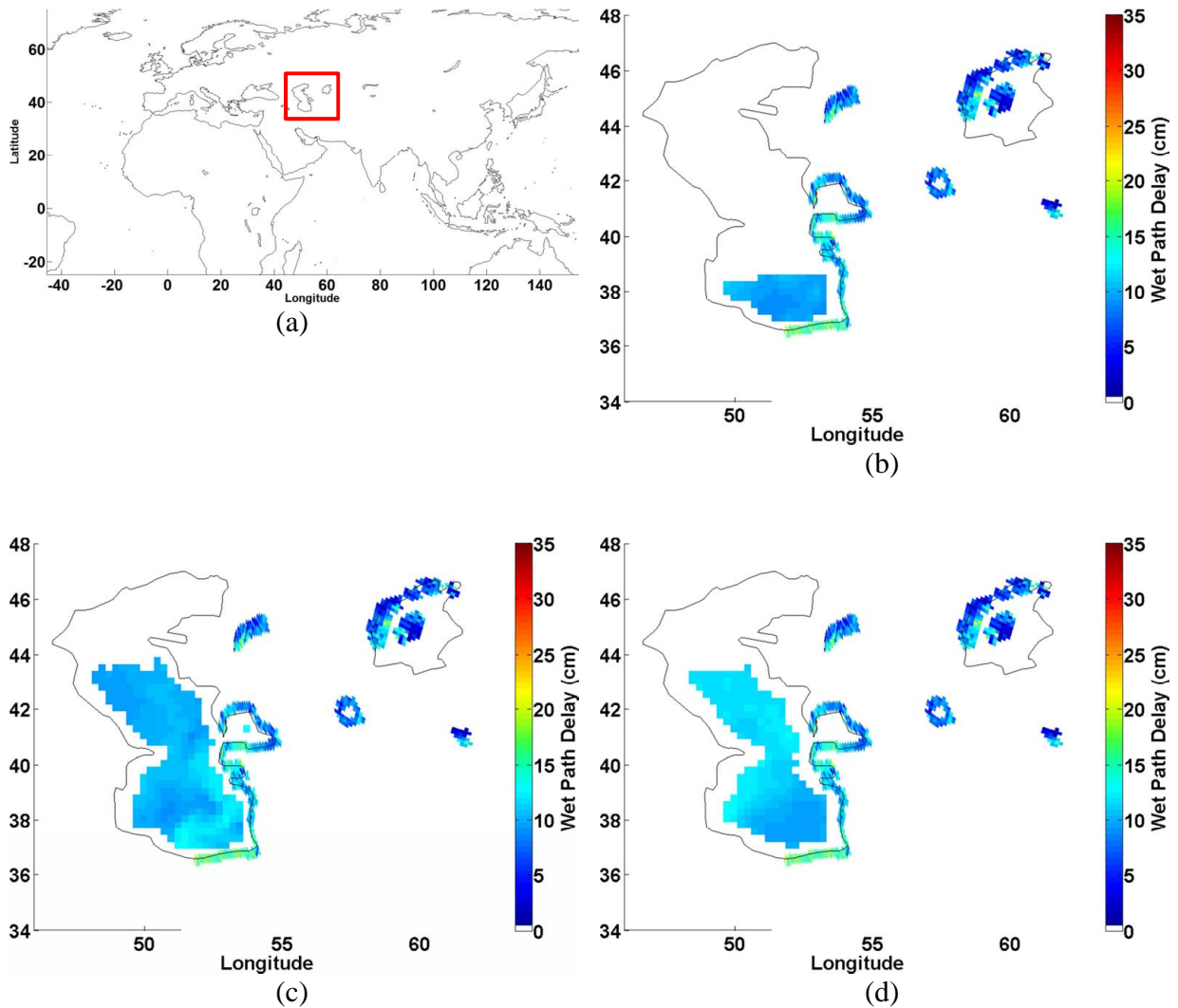


Fig. 4-7: Comparison of BTDR method wet path delay retrievals (shown along the shorelines of the Caspian and Aral Seas) to wet path delays derived from total precipitable water (shown in water) retrieved from (b) TMI, (c) AMSR-E, (d) SSMIS. The general area of the retrieval is shown in (a).

The Caspian and Aral Seas are in a generally dryer region respect to the wet path delay and as such will provide a comparison of the BTDR method retrievals for an area with low wet path delay for the time of year that was studied. As can be seen, the BTDR wet path delay retrievals along the Caspian Sea agree closely to the independent retrievals shown by both Fig. 4-7b for TMI and Fig. 4-7c for AMSR-E for most of the shorelines. Additionally, BTDR retrievals for

lakes at 45° N, 54° E and 42° N 57.5° E and a small island in the Aral Sea also seem to agree with the closest available independent data from AMSR-E and TMI over the Caspian Sea. Retrievals on the north portion of the Aral Sea again seem consistent with the independent retrievals for over the Caspian Sea, implying that BTDR retrievals of low wet path delay areas are likely accurate.

4.3.2: Coastal Retrievals

The BTDR retrievals were performed over the shorelines of the Arabian Sea, with variable wet path delay, from relatively dry in the north to quite humid in the south on the African coast. The BTDR retrievals over the Arabian Sea and the Gulfs of Oman and Aden are shown in Fig. 4-8.

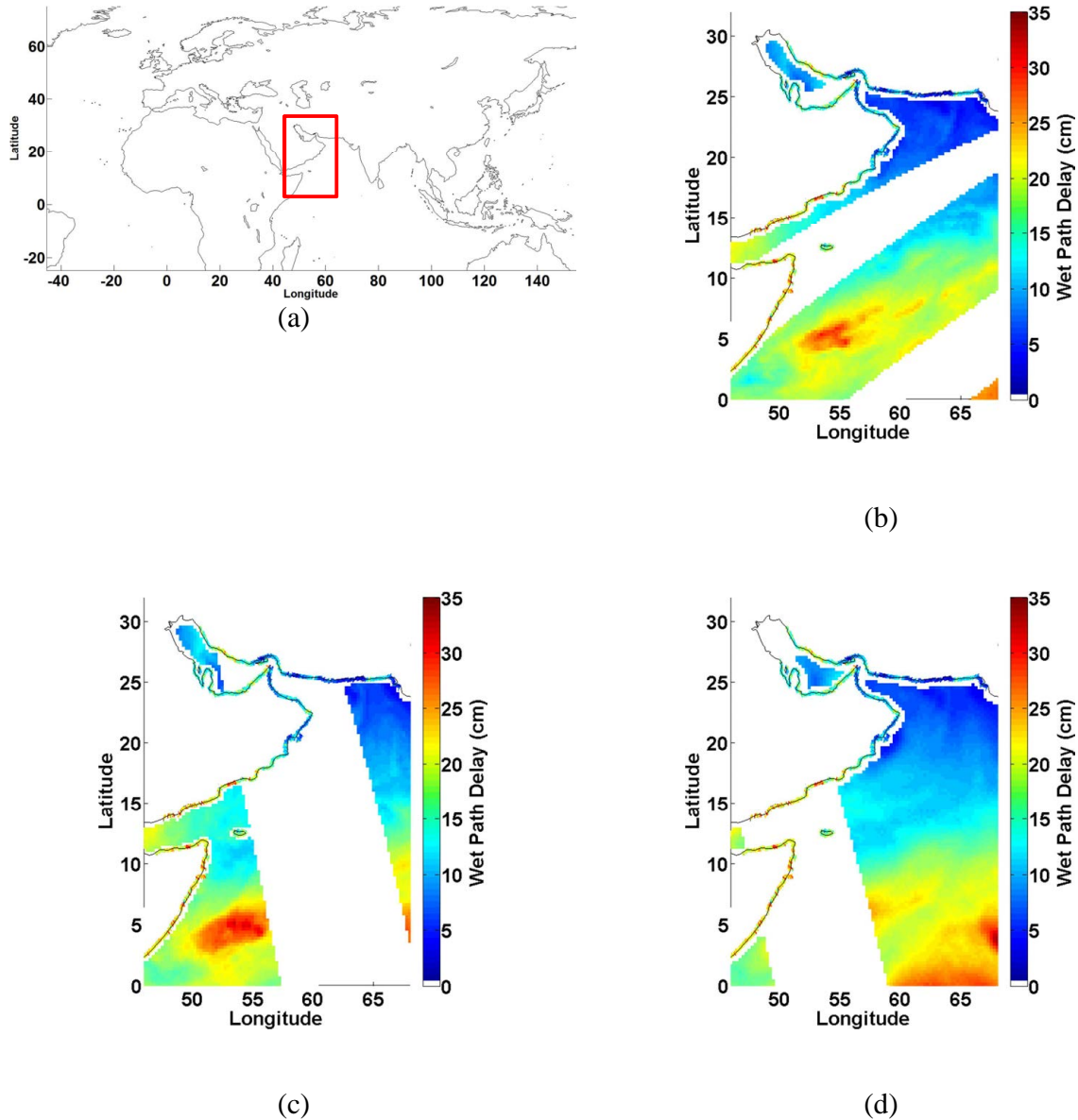


Fig. 4-8: Comparison of BTDR method wet path delay retrievals (shown along the shorelines of the Arabian Sea) to wet path delays derived from total precipitable water (shown in open water) retrieved from (b) TMI, (c) AMSR-E, (d) SSMIS. The general area of the retrieval is shown in (a).

The range of wet path delays from the BTDR retrievals range from approximately 22 cm, near the Gulf of Aden at 12° N, 51° E, to less than 5 cm, on the shore of Pakistan and the Arabian Sea at 25° N, 62° E. Retrievals over the island of Socotra at 12° N, 54° E seem to agree well with the

GPROF 2010 products, highlighting the usefulness of the BTDR method in performing retrievals of wet path delay over islands. Next, we examine the retrieval results from the coastlines of Chile and Argentina as shown in Fig. 4-9.

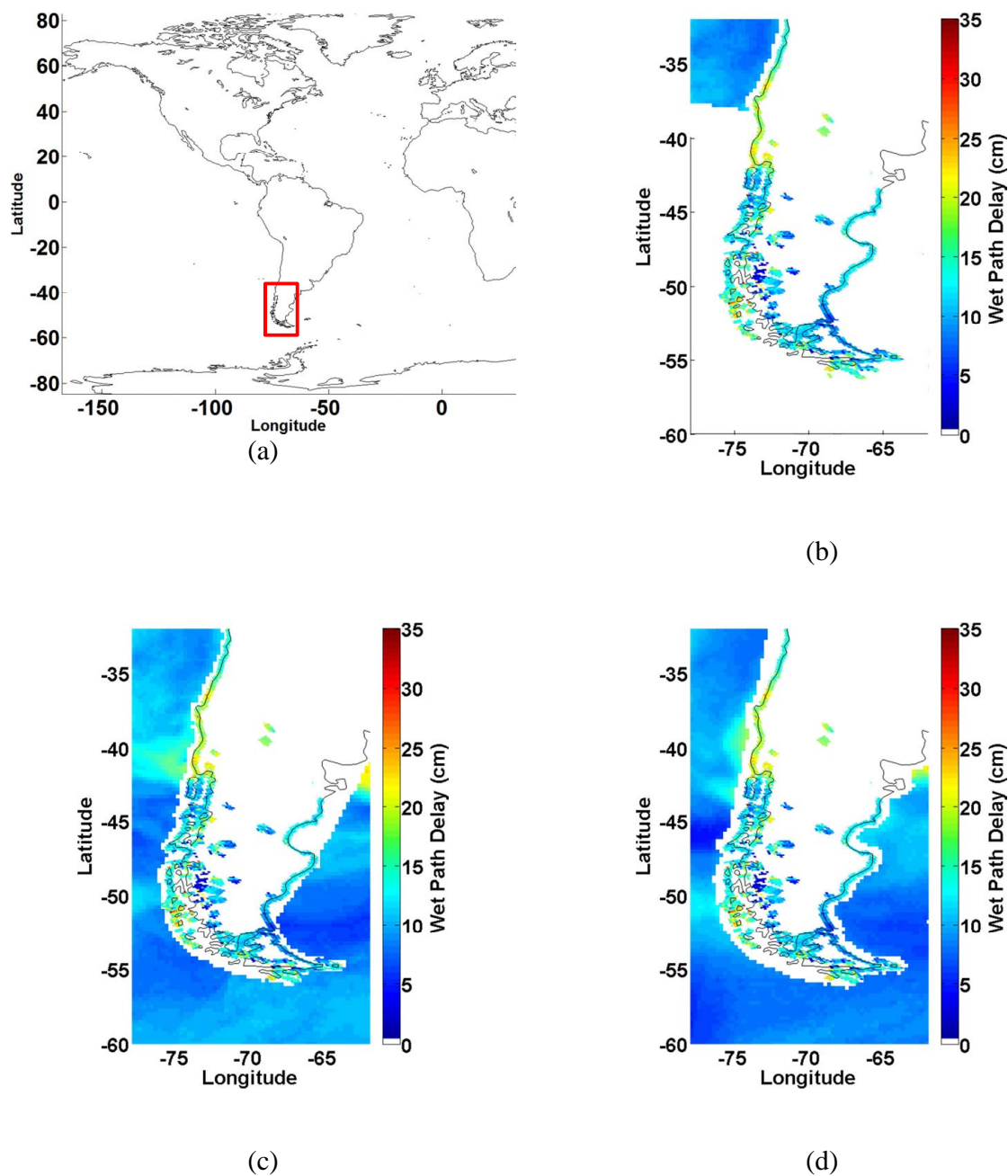


Fig. 4-9 Comparison of BTDR method wet path delay retrievals (shown along the shorelines of the Chile and Argentina) to wet path delays derived from total precipitable water (shown in open water) retrieved from (b) TMI, (c) AMSR-E, (d) SSMIS. The general area of the retrieval is shown in (a).

Similar to before, the BTDR retrievals in this region agree well with the GPROF 2010 TPW products from all three instruments. Several lakes can be seen in the land mass which agree with the nearest coastal TPW products. Additionally, the band of higher wet path delay seen around -

40° S in Fig. 4-9c and d is successfully detected using the BTDR retrievals. Overall, the BTDR method seems to provide qualitative agreement with the GPROF 2010 products over both inland water and coastlines and does not appear to have a bias based on which region the retrieval is performed over. In order to analyze the precision of the BTDR retrievals, a retrieval noise analysis is presented in Section 4.4.

4.4 Error Analysis

In this section, we present a filtering technique in which we will attempt to separate the retrieved atmosphere from the measurement noise, as mentioned in this section. This technique is meant to compensate for the first type of errors which were discussed in Section 4.1, i.e. those due to atmospheric dynamics not included for in the model. By doing this, we can provide a measurement of the algorithm's error in the form of retrieval consistency. In this way, we are able to form an estimate of the retrieval error of the BTDR method in a statistically meaningful way.

4.4.1: Data Consistency Analysis Method

In order to provide a quantitative error estimate for the BTDR retrievals using the SSMIS data, we will analyze the self-consistency of the data. However, before applying a filter to the data, the retrieved path delays along coastlines need to be extracted. This is done by identifying all of the connected pixels of the BTDR retrieved image using a binary connectivity detection algorithm and then removing all connected pixels which have a length less than some threshold, in our case 20. The resulting connected pixels are then further filtered by their latitude and longitude to ensure that only coastlines are used for the comparison.

After identifying the valid coastlines and shorelines according to these criteria, we will decompose the retrieval into two portions, one representing the state of the atmosphere and another representing the noise in the measurement. This is accomplished by filtering the retrieval results along a coastline or shoreline with a low pass filter to obtain the portion of data

representing the atmosphere. Such spatial filtering techniques are used in Synthetic Aperture Radar (SAR) applications [30]. Behind this is the assumption that the atmospheric water vapor is geographically smooth on the scale of kilometers, a reasonable assumption since it is unlikely that the atmosphere would experience very large swings in the amount of vapor when considering the size of the SSMIS measurement spot size. The remainder of the signal, representing the high frequency content, will be assumed to be the collection of all errors in the measurement. An illustration of the spatial frequency representation of the coastline is given in Fig. 4-10.

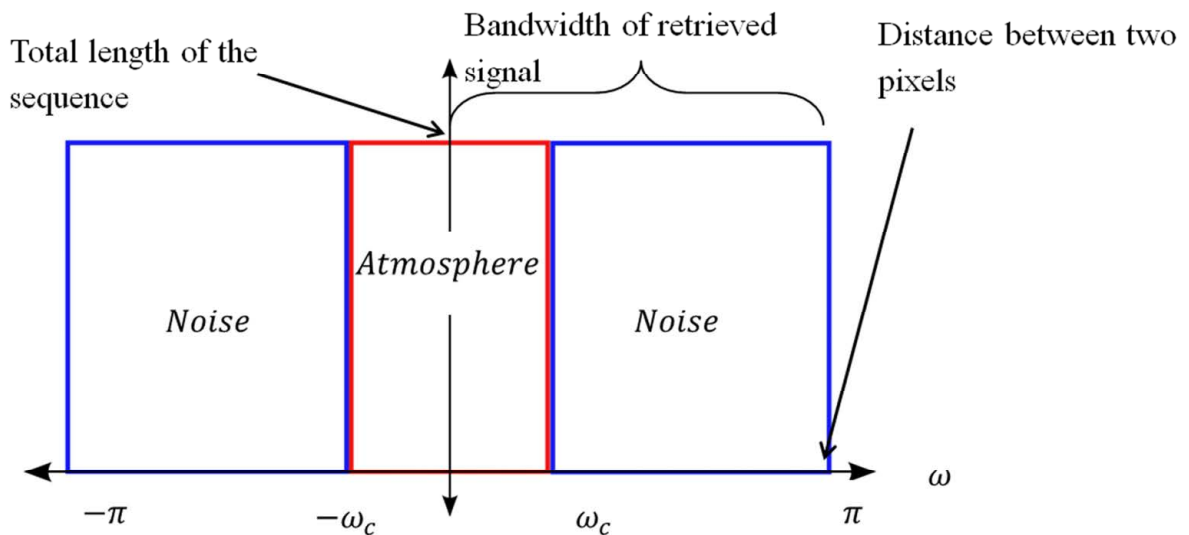


Fig. 4-10: Diagram showing the spatial frequency analysis concept for performing data consistency analysis on the coastlines identified using the BTDR retrieval algorithm. The ω axis is given in radians.

To perform this analysis, a choice for the cutoff frequency, ω_c . To establish an initial choice for the cutoff frequency, simulations were performed in which the retrieval noise with respect to the cutoff frequency was computed. As an example, Fig. 4-11 shows the results for each identified coastline from one of the 8 data files, to be discussed later in the section.

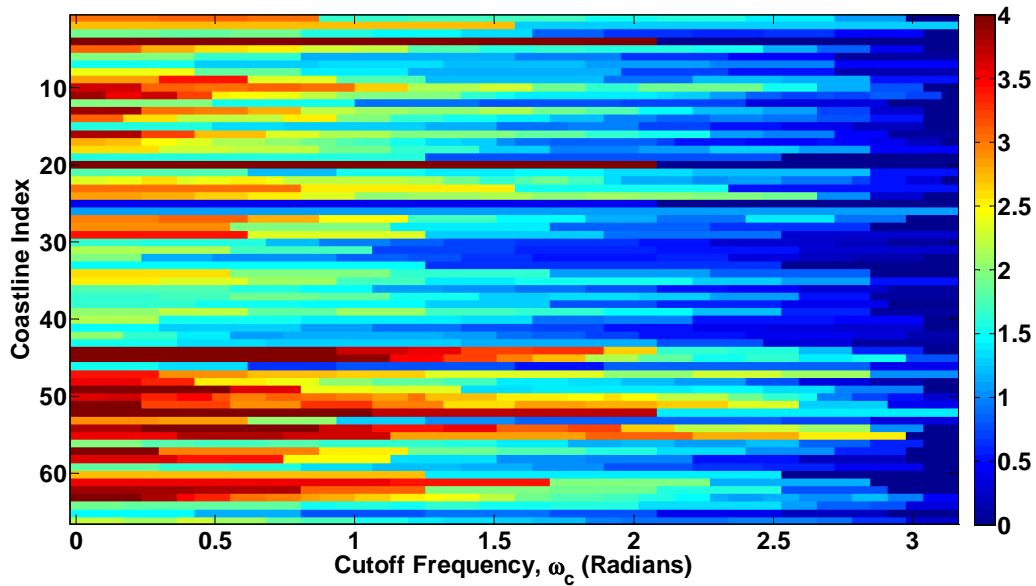


Fig. 4-11: Image showing retrieval noise with respect to cutoff frequency for several coastlines.

In this image, one can see that as the cutoff frequency increases, the retrieval uncertainty, corresponding to the standard deviation of the error contribution to the retrieval along the coastline, decreases. With that said, a filter cutoff at π would mean that the analyzed signal has no noise. Conversely if the cutoff is approximately 0, this means that the analyzed coastline is almost entirely noise. With that said, one could choose the cutoff frequency at a frequency where most errors appear to be saturated. In order to illustrate this, the mean of the retrieval uncertainties for the coastlines of Fig. 4-11 is given in Fig. 4-12

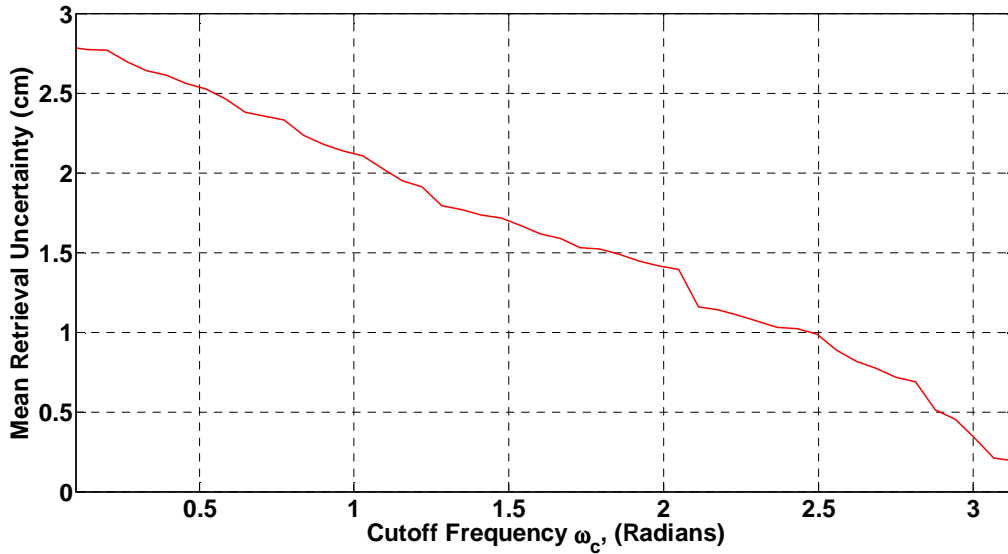


Fig. 4-12: Effect of cutoff frequency choice on mean retrieval uncertainty for the coastlines examined in Fig. 4-11

By examining the mean retrieval uncertainty for this coastline, one can see that the slope flattens slightly between 1.2 to 2 radians. This implies that there is not as significant of a change in this area as with those of other cutoff frequency choices. Furthermore, by choosing a cutoff frequency in this range, one can say that the retrieval along the coastline is between approximately 40% and 60% noise. With that said, the filter cutoff for the analysis shown in this section is chosen to be close to $\pi/2$ radians (roughly corresponding to $1/f_c \cong 75$ km).

After covering the specifics of the data consistency analysis for the SSMIS data, one can turn attention its application for analyzing the results. From here, one can compute the RMS error of each segment in order to provide an estimate of the error present in the retrieval. Additionally, this method allows for one to combine all of the statistics of the retrieved wet path delays into an aggregate data set. From the aggregate data, one can additionally draw conclusions about the average error of the retrieval for the SSMIS instrument when using the BTDR method, as will be shown in Section 4.4.2.

4.4.2: Analysis of Individual Coastlines of SSMIS Derived Wet Path Delays

By applying the analysis method covered in Section 4.4.1, one is able to provide an estimate of the error in the retrieval by way of measurement consistency. This method of analysis allows for one to estimate the error in the retrieval if one assumes that no bias is present. Before continuing to analyze the aggregate statistics of the SSMIS based retrievals, several examples of the data consistency analysis are presented as examples of individual coastlines. To start our analysis, we will choose two coastlines from the Caspian Sea retrievals and compute the RMS error based on our approach, as shown in Fig. 4-13.

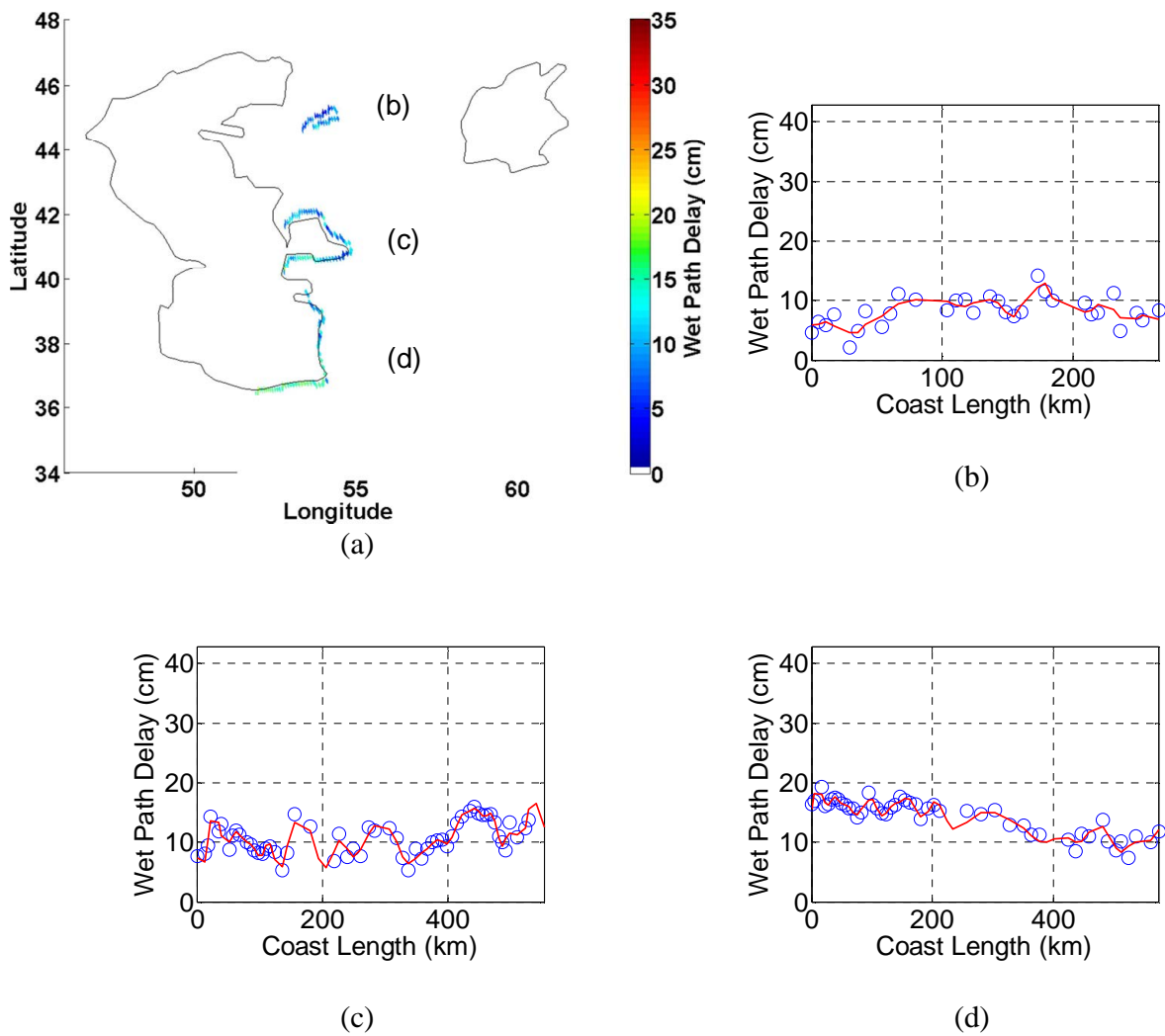


Fig. 4-13: Shown in (a) is a map showing three land water boundaries for which the retrieval consistency analysis was performed for the Caspian Sea Region. Data series of the coastlines are shown in (b), (c), and (d) and indicated on the map in (a).

To analyze individual coastlines, three are chosen from the Caspian Sea retrievals and the root mean square (RMS) of the retrieval noise is computed based on our approach, as shown in Fig. 4-13. The shoreline labeled (b) in Fig. 4-13 encircles a small lake, with a perimeter of approximately 300 km, between the Caspian and Aral Seas. The retrieved wet path delay around the small lake varies from 5 to 10 cm, and the RMS retrieval noise for this shoreline is 1.38 cm. Second, the portion of the shoreline of the Caspian Sea labeled (c) in Fig. 4-13 has retrieved wet

path delays from 5 to 15 cm and has an RMS error of 1.23 cm. Third, the portion of the Caspian Sea shoreline labeled (d) in Fig. 4-13 exhibits retrieved wet path delays between 10 and 17 cm over the 500 km shoreline and has an RMS error of 0.98 cm. In Fig. 4-14 a similar analysis is shown for the coastlines of Arabian Sea.

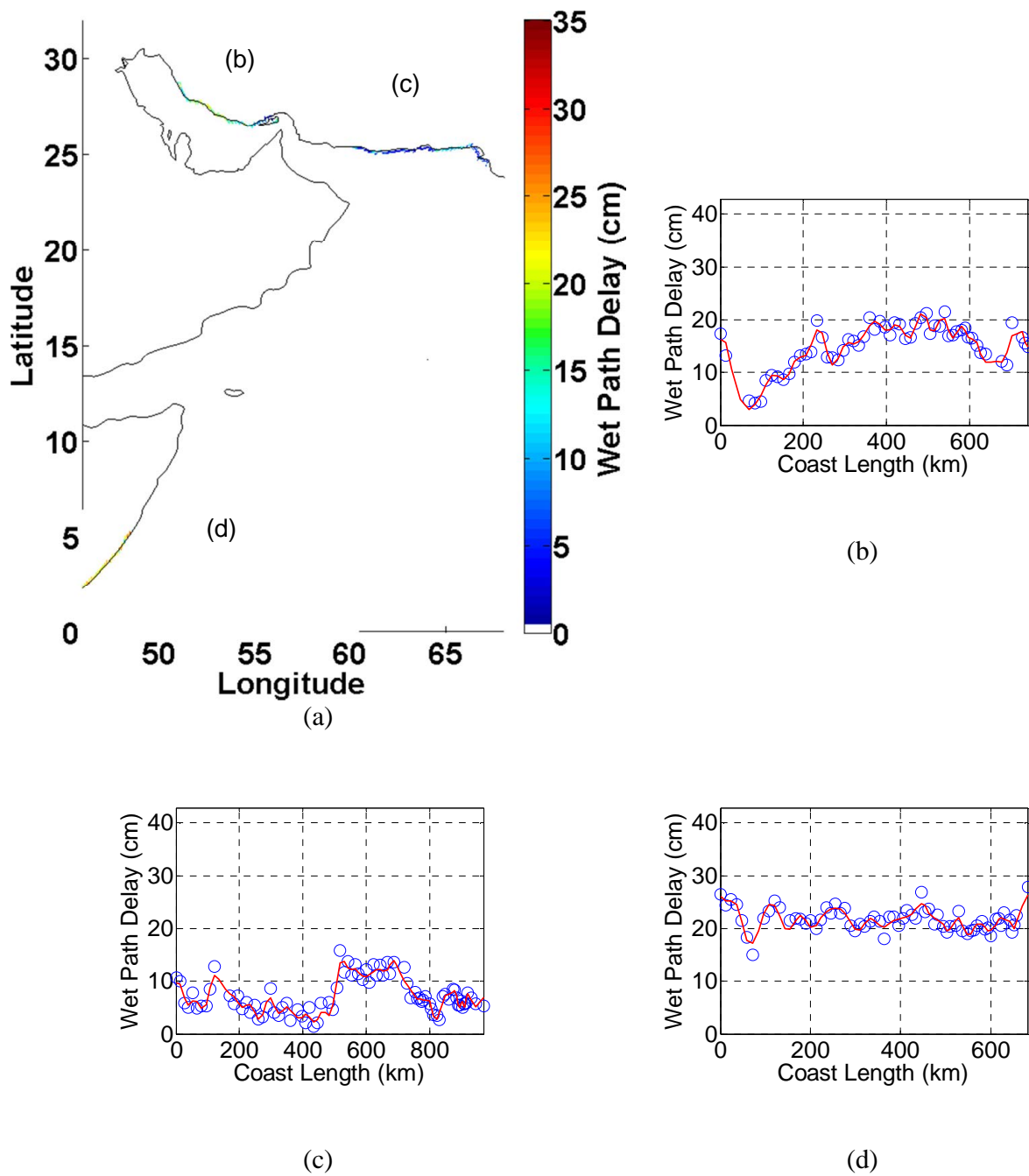


Fig. 4-14: Shown in (a) is a map showing three land water boundaries for which the retrieval consistency analysis was performed for the Arabian Sea Region. Data series of the coastlines are shown in (b), (c), and (d) and indicated on the map in (a).

In contrast with inland water shorelines, continental coastlines would be expected to exhibit a larger range of retrieved wet path delays due to their increased length. The northern coast of the Gulf of Oman, labeled (b) in Fig. 4-14, is approximately 750 km long. Retrieved wet path delays

along this coastline vary from 5 to 20 cm, and the RMS retrieval noise is 1.37 cm. The northern coast of the Arabian Sea, labeled (c) in Fig. 4-14 is approximately 950 km long. Retrieved wet path delays range from a few to 10 cm, and the RMS retrieval noise is 1.27 cm. The coast of Africa on the Arabian Sea, labeled (d) in Fig. 4-14, has relatively constant wet path delay between 20 and 25 cm, making it the region of highest wet path delay that has been studied so far in this section. This coastline has an RMS retrieval noise of 1.13 cm.

4.4.3: Analysis of Aggregate SSMIS Derived Wet Path Delay Retrievals

In addition to the specific examples presented in Section 4.4.2, it is useful to examine retrieval noise on a global basis. To do this, SSMIS data from a total of seven orbits of the DMSP F16, F17, and F18 satellites are used. These include one orbit from the DMSP F16, four from the DMSP F17, and two from the DMSP F18 satellites. The RMS retrieval noise from these orbits is shown in Fig. 4-15.

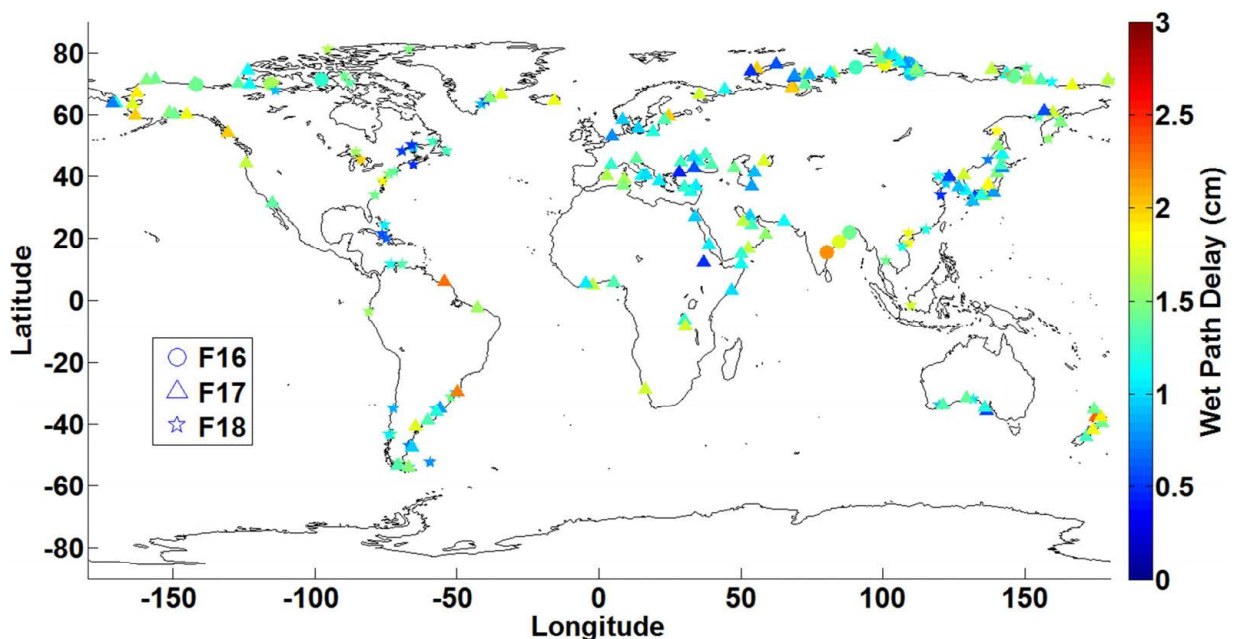


Fig. 4-15: Comparison of the RMS error of the retrievals with respect to the retrieval locations

This selection of orbits provides coverage of most mid-latitude coastlines, as can be seen by examining the error relative to location, there appears to be no geographic bias in the retrievals. Furthermore, errors between the three satellites are negligible, although this will be discussed in further detail later. In order to measure other relationships in the error, we continue to a second comparison of the RMS retrieval error and the range of wet path delay values in each coastline, as shown in Fig. 4-16.

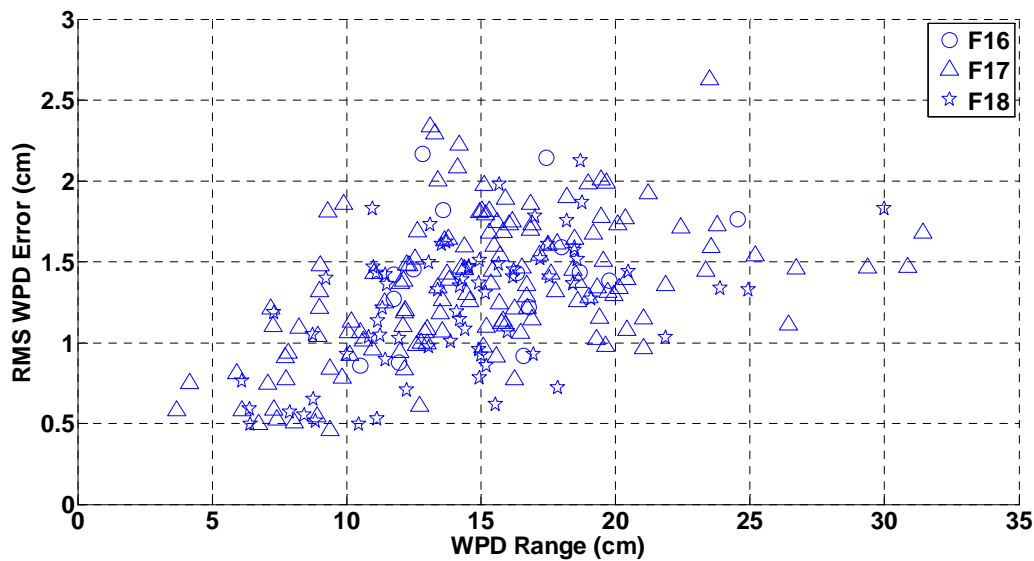


Fig. 4-16: Aggregate plot of the RMS error of the wet path delay for all identified coast and shorelines for the 3 SSMIS data sets of the F16, F17, and F18 satellites with respect to the wet path delay range of each coast/shoreline.

In Fig. 4-16 is a comparison of all RMS errors for every identified coastline plotted with respect to the range of the wet path delays measured within the land/water boundaries. After examining Fig. 4-16, one may note that a linear trend can be seen up to 20 cm. This implies that as the range of path delays in the measurement increases, the higher the retrieval noise will be. It is important to keep in mind that the length of each of the coastlines is typically less than 1000 km and a measurement range of more than 20 cm is unlikely. As an end result of the comparison, it can be seen that the BTDR method retrievals have on average 1.32 cm retrieval noise for the majority

measurement ranges. Next, we will examine the error behavior of the BTDR method with respect to the length of the individual coastline, as seen in Fig. 4-17.

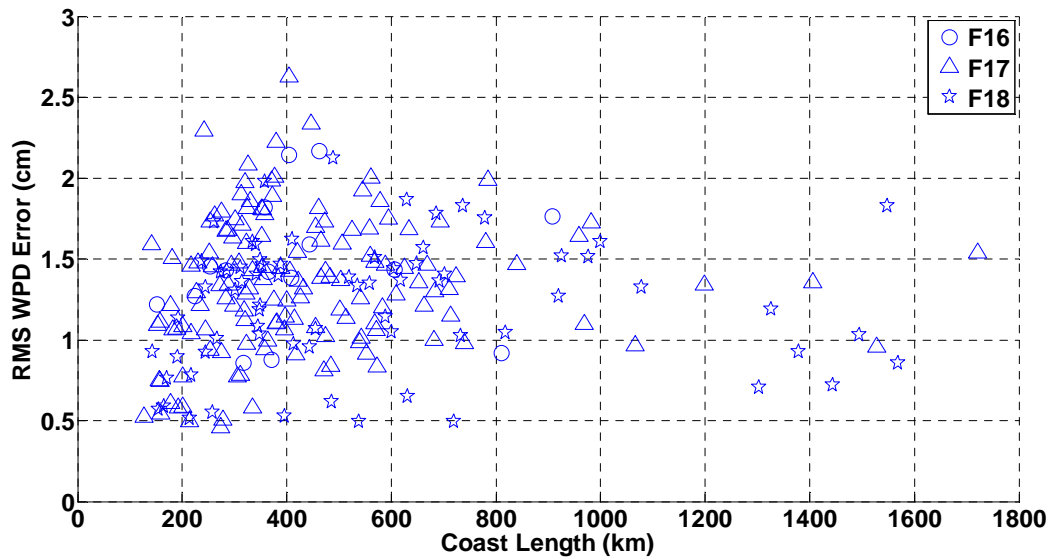


Fig. 4-17: Aggregate plot of the RMS error of the wet path delay for all identified coasts and shorelines for the 3 SSMIS data sets of the F16, F17, and F18 satellites with respect to the length, in km, of each coast/shoreline.

As mentioned previously, nearly all of the coastlines identified in the retrieval consistency study were less than 1000 km in length. There does not appear to be a relationship between the RMS retrieval noise and the length of the coastlines observed, however more data describing longer coastlines is needed to accurately make this assessment over 800 km. From Fig. 4-17, it can be inferred that the retrieval error is independent of coastline length for coastlines up to 800 km long. This is advantageous because it does not place a length restriction on the coastlines which are observed. As before, the average retrieval noise is 1.32 cm.

Following this analysis, we can be fairly sure that the RMS error of our retrieval is on average lower than 1.5 cm for most of the areas which the BTDR method could be used to retrieve the wet path delay. In comparison to the error estimated in simulation, this is a bit higher than was quoted (1 cm from Fig. 3-9). However, as a first attempt at retrieving wet path delay with the

BTDR method, this is a very promising result, as several factors could be accounted for to provide improved retrieval noise; specifically those addressed in Section 5.3. Furthermore, in order to validate that the retrieval bias is within acceptable limits, a collocated and co-synchronous external validation is needed which is derived independently from the same set of measurements. As a concluding remark, it seems as though coastal and inland water retrievals using the BTDR method is a feasible approach to extend retrievals from current open ocean algorithms up to the coastline with an average 1.32 cm RMS error and requiring no *a priori* measurements to perform the retrieval.

Chapter 5: Closing Remarks

This thesis has covered the use of a new retrieval algorithm based on brightness temperature deflection ratios to retrieve the wet path delay above surface targets. It relies on contrast from the background scenes in order to perform the retrievals without the use of *a priori* data. In this chapter, a brief summary of the work in this thesis is presented as well as several general conclusions which can be drawn from the results of simulation and measurement based retrievals. Finally, several future uses and improvements on the algorithm are highlighted, alluding to the promise of the use of BTDR method retrievals for continued study.

5.1: Summary

In this work, a method for retrieving the wet path delay based on calculated deflection ratios is presented. Chapter 1 presents the required background knowledge to develop the BTDR algorithm. The concept of black body radiation is introduced and a derivation of the observed brightness temperature and antenna temperatures is provided. Additionally, the theory of radiative transfer is described and definitions for relevant atmospheric parameters, such as the transmissivity, are given. Following this, a general description of radiometer types is given and the concept of radiometric resolution is introduced. A general overview of prior retrieval algorithms is given to provide a context to the retrieval algorithm's purpose. It is important to note that many of these retrieval algorithms depend upon prior statistical information of the scene that is being observed, whereas the BTDR method in general does not.

In Chapter 2, the brightness temperature deflection ratio is developed from a theoretical standpoint starting with a non-scattering radiative transfer model for an atmosphere. A model deflection ratio is established as a function of the atmospheric transmissivity and a lumped parameter to account for un-modeled effects. This sum of squared errors between the model deflection ratio and a measured deflection ratio is optimized as a two-dimensional function of the transmissivity due to water vapor and the lumped parameter. Next, it is possible to map the

transmissivity to a corresponding wet path delay value using established atmospheric absorption models to computationally relate the two terms. After developing the theory behind the BTDR method, Chapter 2 explains several functional aspects of the algorithm. In this chapter, the theory behind the Rosenkranz absorption model is detailed, as well as the use of edge detection algorithms that are pertinent to the use of the BTDR algorithm on measured data. Following this explanation, a description of the MATLAB implementation of the BTDR algorithm is given and several of the testing procedures are described.

In order to demonstrate the concept of the BTDR method as a retrieval algorithm, several simulated retrievals are presented in Chapter 3. The purpose of the simulated retrievals was to characterize the behavior of the BTDR algorithm such that the results from measured data could be interpreted more easily. The first of the simulations presented is a series of simulations to determine the number of channels required to retrieve wet path delay values. According to these simulations, the number of channels required to perform the retrieval was dependent which frequency channels were chosen. It was decided that, following results from these simulations, three frequency channels would be used and these choices are justified by an Eigen analysis of the brightness temperature differences and deflection ratios which can be formed from them. Following the three frequency choice, further simulations were performed to determine which three frequency sets could be the most useful in retrieving the wet path delay by the BTDR method. Several bands of the 40-200 GHz spectrum were identified in this analysis and are discussed. A contour analysis using several frequency sets is presented which highlights the behavior of the minimization space for the two-dimensional cost function relating the modeled and measured deflection ratios. From the contour analysis, several conclusions about how the BTDR retrievals perform under varying atmospheric changes are made and a feel for its immunity to un-modeled changes is given. In order to further understand how the BTDR algorithm performs in the presence of noise, a statistical noise simulation is presented in which Gaussian distributed noise is added to the simulated brightness temperatures before retrieval.

This is done for several noise levels and frequency sets. To conclude the chapter, the effects of bandwidth and radiometric resolution are including and the behavior of the BTDR method is evaluated for frequency channels from the HAMSR and SSMIS instruments.

In Chapter 4, measured retrieval results are presented. Before discussing the retrievals from the HAMSR and SSMIS instruments, a listing of errors found in measured data is given. The types of error are discussed as well as possible ways to mitigate various types of errors. Following this, a proof of concept based on measurements taken by HAMSR aboard the NASA Global Hawk aircraft over the Saint John's River in Florida, USA are examined. These retrievals are compared to converted wet path delay values from the NOAA NOMADS forecast database and provide close agreement. From here, the BTDR method is applied to measured brightness temperatures from SSMIS for January 1, 2010. Multiple orbits from the F16, F17, and F18 DMSP satellites are used for the retrievals. The BTDR retrieved wet path delay values are compared to converted TPW products from the GPROF 2010 algorithm using measurements from TMI, AMSR-E, and SSMIS. These retrievals include both inland water and coastal areas and can be thought of as a way to "fill the gaps" in areas where the coast prohibits conventional wet path delay retrieval. Additionally, an aggregate statistical analysis of the consistency of the BTDR retrieved wet path delays is given and an average RMS error of approximately 1.3 cm is seen.

5.2: Conclusions

To meet the objectives proposed by satellite altimetry missions such as SWOT, the development of improved wet path delay retrieval algorithms is required. Additionally, to enable the measurement of surface water bodies other than the ocean algorithms and instruments using higher frequency channels are needed. The BTDR method described in this paper allows for retrieval of wet path delay when contrast in the ground scenes is present, i.e. at land-water interfaces. To indicate potential frequency channels which could be used with the BTDR method, a frequency selection study is presented in order to highlight the best candidates which

could be used to retrieve wet path delay over inland bodies of water and investigate the level of noise immunity when using such sets. Additionally, retrievals were performed using calibrated brightness temperature measurements from the SSMIS instrument for several locations around the globe with varying amounts of wet path delay in order to demonstrate the algorithms capabilities when used with measured brightness temperatures from a spaceborne radiometer. The general agreement of these retrievals with two independently retrieved sources of wet path delay shows that the BTDR method is a feasible means by which to provide scientists with greater information of the amount and behavior of atmospheric water vapor along coastlines and rivers. However, to perform these retrievals, a sufficiently transparent channel (such as the 91.655 GHz channel from SSMIS) is beneficial in that it allows more accurate detection of coastlines, bodies of water, and anomalies than would a channel closer to an absorption region. Also, an inherent advantage of the BTDR method over past retrieval algorithms is that it requires no *a priori* data in order to discern the state of the atmosphere so long as sufficient contrast in the background scenes can be detected. Furthermore, the retrievals performed using SSMIS measured brightness temperatures yielded an average RMS error of approximately 1.3 cm. This error is likely instrument dependent as the BTDR method functions based on contrast between measured brightness temperatures of adjacent pixels in a brightness temperature image. With this in mind, it seems that using the BTDR method to provide wet path delay information from brightness temperature measurements of either current instruments, such as SSMIS, or future instruments, such as those under development for the SWOT mission, is feasible and worth further exploration.

5.3: Future Work

Throughout this work, several different aspects of the BTDR method have been explored. In Section 5.1 the content of this Master's thesis was briefly summarized and in Section 5.2 conclusions about the usefulness of the BTDR algorithm. However, to this point the focus of the discussion has been on prior work. Now, it is convenient to turn attention to future areas of work

for retrievals with the BTDR algorithm. In this section several areas of improvement, further validation methods, or potentials for products other than water vapor are discussed.

The first topic of discussion in this section will highlight ways in which the current BTDR method could be improved to be more robust or provide more accurate retrievals. In order to increase the robustness of the algorithm, models which accounted for the presence of clouds could be introduced. Clouds in the atmosphere can create a change in the emissivity of the surface which is viewed, resulting in a different brightness temperature measurement than might be seen if no clouds were present. This step could likely be taken as a modification of the existing emissivity models and could be introduced as a correction factor for the calculated emissivity. In situations where clouds were present, typically provided as a flag in the measurement data from radiometric instruments, the correction factor could be used and when no clouds were present it could be omitted.

Another possible area of improvement for the current BTDR algorithm is to explore the use of different numbers of frequency channels more thoroughly. This implies an extended eigenvalue study, such as that presented in Section 3.1 of Chapter 3. Based on the analysis of Section 3.1, using more than 3 frequency channels in the set of retrieval frequencies could potentially be useful if the channels were chosen carefully. This could be initially determined by a study similar to three point selection criteria presented in Section 3.2. Furthermore, rather than exploring the use of more than 3 frequency channels in the retrieval set, one could perform a series of retrievals in which increasingly opaque channels were included, i.e. atmospheric profiling. In this way, it could be possible to retrieve the distribution of water vapor in the column above the measurement scene. A careful selection of frequency channels which allow for profiling yet still enable partial visibility of the contributions from the land would need to be included in order to use the current BTDR algorithm. In addition, it could be possible to reformulate the model deflection ratio in terms of a partial contribution from the atmosphere. Both of these methods

imply an increase in the number of retrievals for a specific pixel and would require an instrument which can provide measurements from radiometric channels at which the opacity is steadily changing, i.e. on the wings of absorption bands.

In addition, other validation methods besides those from GPROF 2010 retrievals could be used. For example, one could compare the BTDR retrieved wet path delays with those from either radiosonde launches along the coast of wet path delay retrievals from coastal GPS measurements. These point comparisons could be considered as a way to check whether the retrieval in a specific area made sense and was coherent. However, the comparison to these data sources presents two problems. First of all, the comparisons would only be valid for a very small amount of locations, as there are very few radiosonde launch and GPS stations around the globe compared to the number of pixels retrieved by the BTDR method. Furthermore, radiosonde wet path delay measurements have errors typically around 5-7% and can vary spatially over tens of kilometers [31, 32, 33]. With that said, it is likely that the use of GPS wet path delay retrievals would provide a more consistent independent point validation than radiosondes. Now that several ways to improve the existing BTDR algorithm have been mentioned, one can turn attention to new products and uses which could benefit from applying a general approach of deflection ratio measurements.

To continue the discussion, it is natural to turn attention to new areas to which the BTDR method could be applied. An assumption of the BTDR method, as mentioned in Chapter 2, is that contrast in the two scenes is required in order to perform a retrieval. The focus of this Master's thesis has been to retrieve the wet path delay along land water interfaces; meaning the sources of contrast come from the differing emissivities of land and water. However, this contrast can also be found in the brightness temperature imagery of oceanic storms. Shown in Fig. 5- is an illustration of measured brightness temperatures at 91.655 GHz from the SSMIS instrument.

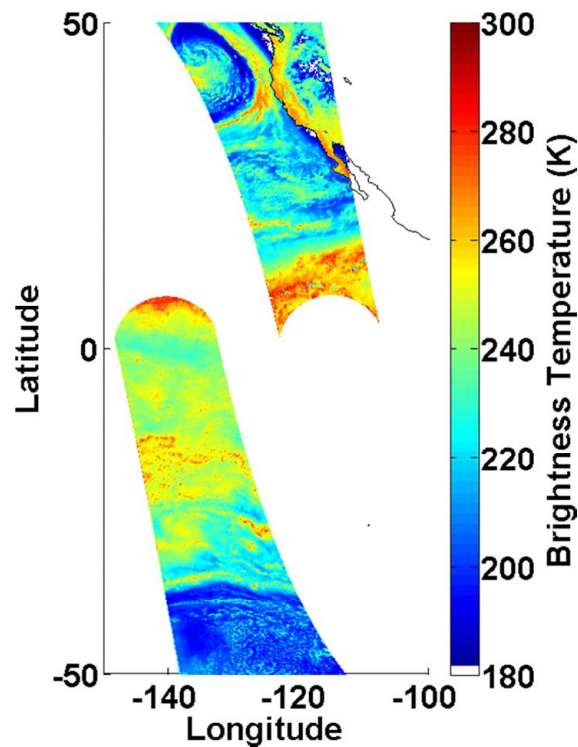


Fig. 5-1: Brightness temperature imagery for a portion of the Pacific Ocean measured by the 91.655 GHz SSMIS channel

As can be seen in Fig. 5- There is a clear distinction in brightness temperatures due to the cloud and oceanic scene. This implies that these contrasting areas could be used to retrieve wet path delay with the BTDR method in a very similar manner to the way that land/water scenes are treated. As a potential first step, one could replace the land emissivity model with a similar emissivity model for clouds, however further complications with this could arise. Specifically, the presence of ice particles could provide further sources of error for the retrievals unless accounted for in some way. Additionally, window channels which can see the contribution from the ocean surface, as well as those from the atmospheric water vapor, would be required as in the BTDR approach described in this thesis. As a preliminary step, the land/water BTDR retrieval algorithm was applied to the oceanic scene shown in Fig. 5-1. The results of this retrieval, as well as the GPROF 2010 open ocean retrievals from SSMIS, are shown in Fig. 5-2.

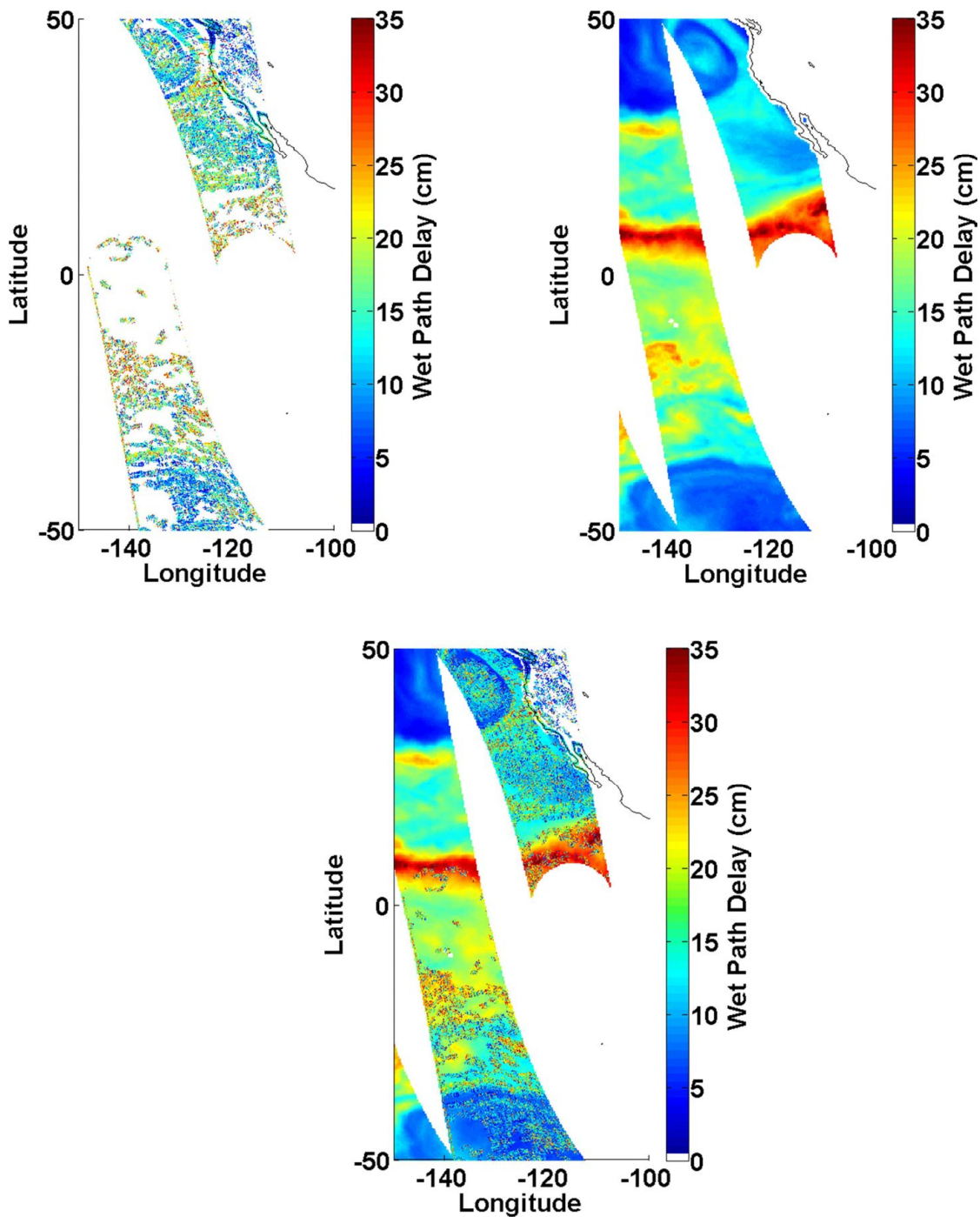
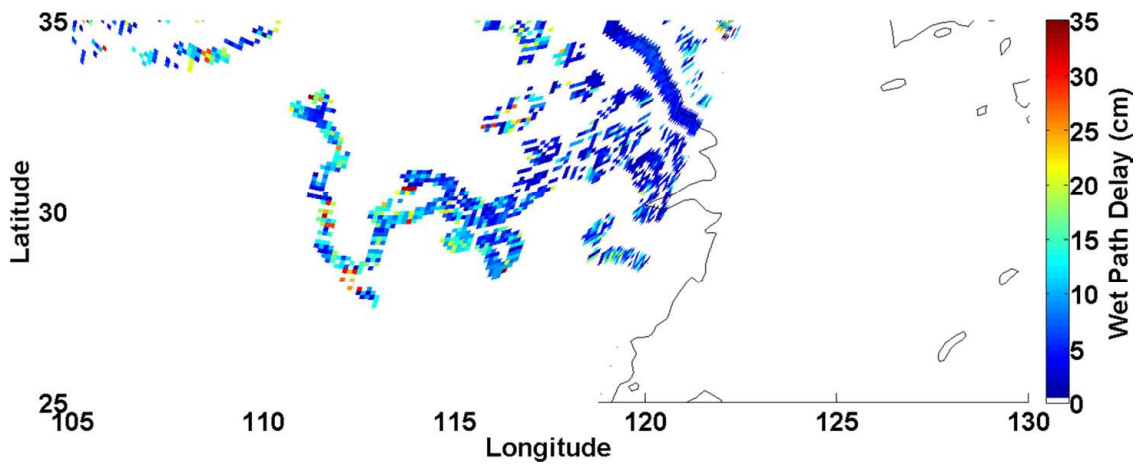


Fig. 5-2: Retrieval results for a portion of the Pacific Ocean using (a) the BTDR method and (b) the GPROF 2010 algorithm. Shown in (c) is an overlay of the two retrievals for comparison.

As can be comparison of the BTDR and GPROF 2010 retrievals in Fig. 5-2, there exists some agreement between the wet path delay values. However, the BTDR retrievals seem quite noisy and have considerable bias in some cases. This is likely because the algorithm is currently

specialized to work along coastlines with assumed land and water emissivity models. The noise levels and bias could likely be reduced, implied that one could use the BTDR method to retrieve open ocean wet path delays when oceanic storms and cloud formations were present. The advantage of doing this would be to provide cross-check information for currently available products as the BTDR retrievals do not rely on *a priori* information and would represent contributions from only the time of the measurements which were taken.

Furthermore, as the BTDR algorithm uses edge detection to identify areas of contrast in the brightness temperature images, it is possible that, using a more sensitive detector such as the Canny detector explained in Chapter 2, one could retrieve wet path delays in features which are quite small. For example, a portion of the Yangtze River in China, which runs from Shanghai to approximately Wuhan, was identified by the Canny detector and wet path delay retrievals were performed. Additionally, several smaller features were identified between Changde, near 27° N, 105° W, and Xiangyang, near 33° N, 105° W as well as lakes near 33° N, 117° W. Preliminary retrieval results for these retrievals are shown in Fig. 5-3 with a map to aid in tracing the features.



(a)



(b)

Fig. 5-3: Map of the (a) retrieved wet path delays using the BTDR algorithm and (b) geography of the retrieval area to aid in feature identification.

As can be seen from the figures, the BTDR retrievals seem to trace along the path of the Yangtze River which can clearly be seen in the map shown in Fig. 5-3 b. This shows promise as an area for future work and could provide the scientific community with satellite based wet path delay measurements which are not currently available. For independent verification, it could be

possible to compare these retrievals to radiosonde or GPS based wet path delay retrievals in the area.

As was previously mentioned, the presence of ice in the atmosphere could have negative effects on the retrieval results from either the oceanic or land/water retrievals. However, this presents another possible opportunity to apply the BTDR method as well. By introducing a new model deflection ratio, it might be possible to determine the presence or amount of ice in the atmosphere. This implies that a new radiative transfer model would be needed which had terms accounting for the presence of ice, as well as the surface emissivities and temperatures. This likely means a relaxation of the scattering assumption made in Chapter 2 and an increase in the dimension of the optimization space.

Finally, since the BTDR method relies on contrast in the scenes, it could be possible to perform retrievals using pairs of horizontal and vertical polarized frequency channels. In this case, a new model deflection ratio would need to be derived to account for differences in scene temperatures due to polarization rather than surface conditions. Of the potential areas of future work in this section, the use of mixed polarization in the BTDR retrievals is likely the most extensive with respect to changes to the algorithm as presented in this thesis. As such, this concept is left as a speculation and is not further explored.

With the aforementioned points in mind, one can surmise that the BTDR method provides a considerable flexibility in its applications and uses. With that said, pursuing it as a future method of retrieval algorithm formulation seems promising. Furthermore, since the retrievals are not based on *a priori* data, they could be more indicative of the current state of the atmosphere at the time of the measurement than those based on other methods which rely on historical data.

REFERENCES

- [1] Space Studies Board, "Earth Science and Applications from Space: National Imperatives for the Next Decade and Beyond," *National Research Council*, p. 81, Jan. 2007.
- [2] M. Durand, L.-L. Fu, D. P. Lettenmaier, D. E. Alsdorf, E. Rodriguez and E.-F. D., "The Surface Water and Ocean Topography Mission: Observing Terrestrial Surface Water and Oceanic Submesoscale Eddies," *Proc. IEEE*, vol. 5, no. 98, pp. 766-779, May 2010.
- [3] S. P. Neeck and P. V. Vaze, "The Ocean Surface Topography Mission (OSTM)," *Proc. of SPIE*, vol. 7106, no. 710603, pp. 1-11, 2008.
- [4] S. C. Reising, P. Kangaslahti, S. T. Brown, D. E. Dawson, A. Lee, D. Albers, O. Montes, T. C. Gaier, D. J. Hoppe and B. Khayatian, "InP HEMT Low-Noise Amplifier-based Millimeter-wave Radiometers from 90 to 180 GHz with Internal Calibration for Remote Sensing of Atmospheric Wet-Path Delay," in *Proc. IEEE Int'l Microwave Symp. '12*, Montreal, QC, Canada, June 2012.
- [5] S. T. Brown, "A Novel Near-Land Radiometer Wet Path-Delay Retrieval Algorithm," *IEEE Trans. Geosci. Remote Sensing*, vol. 48, no. 4, pp. 1986-1992, Apr. 2010.
- [6] R. Bennartz, "On the Use of SSM/I Measurements in Coastal Regions," *Journal of Atmospheric and Oceanic Technology*, vol. 16, pp. 417-431, Apr 1999.
- [7] A. S. Jones, J. M. Forsythe and T. H. Vonder Haar, "Retrieval of Global Microwave Surface Emissivity Over Land," in *13th Conference on Satellite Meteorology and Oceanography*, Norfolk, VA, Sept. 2004.
- [8] F. T. Ulaby, R. K. Moore and A. K. Fung, "Microwave Remote Sensing: Active and

- Passive," Norwood, MA, Artech House, 1981, pp. 344-429.
- [9] P. W. Rosenkranz, "Water vapor microwave continuum absorption: A comparison of measurements and models," *Radio Sci.*, vol. 33, no. 4, pp. 919-928, Jul.-Aug. 1998.
- [10] J. H. Van Vleck and D. L. Huber, "Absorption, emission, and linebreadths: A semihistorical perspective," *Review of Modern Physics*, vol. 49, no. 4, pp. 939-959, Oct 1977.
- [11] C. Mätzler and P. W. Rosenkranz, "Dependence of Microwave Brightness Temperature on Bistatic Surface Scattering: Model Functions and Application to AMSU-A," *IEEE Trans. on Geosci. and Rem. Sens.*, vol. 45, no. 7, pp. 2130-2138, July 2007.
- [12] J. Randa, J. Lahtinen, A. Camps, A. J. Gasiewski, M. Hallikainen, D. M. Le Vine, M. Martin-Neira, J. Piepmeier, P. W. Rosenkranz, C. S. Ruf, J. Shiue and N. Skou, "Recommended Terminology for Microwave Radiometry," National Institute of Standards and Technology, Washington D.C., Aug. 2008.
- [13] N. Skou and D. Le Vine, *Microwave Radiometer Systems*, Norwood, MA: Artech House, 2006.
- [14] V. H. Payne, J. S. Delamere, K. E. Cady-Pereira, R. R. Gamache, J.-L. Moncet, E. J. Mlawer and S. A. Clough, "Air-broadened halfwidths of the 22 GHz and 183 GHz water vapor lines," *IEEE Trans. Geosci. Remote Sensing*, vol. 46, no. 11, pp. 3601-3617, Nov. 2008.
- [15] V. H. Payne, E. J. Mlawer, K. E. Cady-Pereira and J.-L. Moncet, "Water vapor continuum absorption in the microwave," *IEEE Trans. Geosci. Remote Sensing*, vol. 49, no. 6, pp. 2194-2208, 2011.

- [16] T. J. Hewison, "Airborne Measurements of Forest and Agricultural Land Surface Emissivity at Millimeter Wavelengths," *IEEE Trans. Geosci. Remote Sensing*, vol. 39, no. 2, pp. 393-400, Feb. 2001.
- [17] T. Meissner and F. J. Wentz, "The Complex Dielectric Constant of Pure and Sea Water from Microwave Satellite Observations," *IEEE Trans. Geosci. Remote Sensing*, vol. 42, no. 9, pp. 1836-1849, Sep. 2004.
- [18] L. S. Rothman, I. E. Gordon, A. Barbe, D. C. Benner, P. F. Bernath, M. Birk, V. Boudon, L. R. Brown, A. Campargue, J.-P. Champion, K. Chance, L. H. Coudert, V. Dana, V. M. Devi, C. Fally, J.-M. Flaud, R. R. Gamache, A. Goldman, D. Jacquemart, I. Kleiner, N. Lacome, W. J. Lafferty, J.-Y. Mandin, S. T. Massie, S. N. Mikhailenko, C. E. Miller, N. Moazzen-Ahmadi, O. V. Naumenko, A. V. Nikitin, J. Ophal, V. I. Perevalov, A. Perrin, A. Predoi-Cross, C. P. Rinsland, M. Rotget, M. Simeckova, M. A. H. Smith, K. Sung, S. A. Tashkun, J. Tennyson, R. A. Toth, A. C. Vandaele and J. Vander Auwera, "The HITRAN 2008 molecular spectroscopic database," *Journal of Quantitative Spectroscopy and Radiative Transfer*, vol. 110, pp. 533-572, Feb. 2009.
- [19] R. C. Gonzalez and R. E. Woods, *Digital Image Processing*, Upper Saddle River, NJ: Pearson Prentice Hall, 2008.
- [20] J. Canny, "A Computational Approach to Edge Detection," *IEEE Trans on Pattern Analysis and Machine Intelligence*, Vols. PAMI-8, no. 6, pp. 679-698, 1986.
- [21] P. Stum, P. Sicard, L. Carrere and J. Lambin, "Using Objective Analysis of Scanning Radiometer Measurements to Compute the Water Vapor Path Delay for Altimetry," *IEEE Trans. Geosci. Remote Sensing*, vol. 49, no. 9, pp. 3211-3223, Sep. 2011.

- [22] "U.S. Standard Atmosphere, 1976," U.S. Government Printing Office, Washington, DC., 1976.
- [23] S. T. Brown, B. Lambrigsten, R. F. Denning, T. Gaier, P. Kangaslahti, B. H. Lim, J. M. Tanabe and A. B. Tanner, "The High-Altitude MMIC Sounding Radiometer for the Global Hawk Unmanned Aerial Vehicle: Instrument Description and Performance," *IEEE Trans. Geosci. Remote Sensing*, vol. 49, no. 9, pp. 3291-3301, Sep. 2011.
- [24] D. B. Kunkee, G. A. Poe, D. J. Boucher, S. D. Swadley, Y. Hong, J. E. Wessel and E. A. Uliana, "Design and Evaluation of the First Special Sensitive Microwave Imager/Sounder," *IEEE Trans. Geosci. Remote Sensing*, vol. 46, no. 4, pp. 863-883, Apr. 2008.
- [25] NOAA, 13 Aug. 2012. [Online]. Available: <http://nomads.ncdc.noaa.gov/data.php>. [Accessed 30 Oct. 2012].
- [26] C. Kummerow, W. Barnes, T. Kozu, J. Shiue and J. Simpson, "The Tropical Rainfall Measuring Mission (TRMM) Sensor Package," *J. Atmos. Oceanic Technol.*, vol. 15, no. 3, pp. 809-817, Jun. 1998.
- [27] T. Kawanishi, T. Sezai, Y. Ito, K. Imaoka, T. Takeshima, Y. Ishido, A. Shibata, M. Miura, H. Inahata and R. W. Spencer, "The Advanced Microwave Scanning Radiometer for the Earth Observing System (AMSR-E), NASDA's contribution to the EOS for global energy and water cycle studies," *IEEE Trans. Geosci. Remote Sensing*, vol. 41, no. 2, pp. 181-194, Feb. 2003.
- [28] C. Kummerow, Y. Hong, W. S. Olson, S. Yang, R. F. Adler, J. McCollum, R. Ferraro, G. Petty, D.-B. Shin and T. T. Wilheit, "The Evolution of the Goddard Profiling Algorithm (GPROF) for Rainfall Estimation from Passive Microwave Sensors," *J. Appl. Meteor.*, vol.

- 40, pp. 1801-1820, Jun. 2001.
- [29] H. Masanuga and C. Kummerow, "Combined Radar and Radiometer Analysis of Precipitation Profiles for a Parametric Retrieval Algorithm," *J. Appl. Meteor.*, vol. 22, pp. 909-929, Jul. 2005.
- [30] Z. Li, J.-P. Muller, P. Cross and E. J. Fielding, "Interferometric synthetic aperture radar (InSAR) atmospheric correction: GPS, Moderate Resolution Image Spectroradiometer (MODIS), and InSAR integration," *Journal of Geophysical Research*, vol. 110, no. B03410, pp. 1-10, 2005.
- [31] J. Wang and L. Zhangs, "Systematic Errors in Global Radiosonde Precipitable Water Data from Comparisons with Ground-Based GPS Measurements," *J. of Climate*, vol. 21, pp. 2218-2238, 2008.
- [32] J. K. Luers, "Temperature Error of the Vaisala RS90 Radiosonde," *J. Atmos. Oceanic Technol.*, vol. 19, pp. 1521-1532, 1997.
- [33] S. Padmanabhan, S. C. Reising, J. Vivekanandan and F. Iturbide-Sanchez, "Retrieval of Atmospheric Water Vapor Density With Fine Spatial Resolution Using Three-Dimensional Tomographic Inversion of Microwave Brightness Temperatures Measured by a Network of Scanning Compact Radiometers," *IEEE Trans. Geosci. and Remote Sens.*, vol. 47, no. 11, pp. 3708-3721, Nov 2009.

LIST OF ABBREVIATIONS

AMR – Advanced Microwave Radiometer

AMSU – Advanced Microwave Sounding Unit

AMSR-E – Advanced Microwave Sounding Radiometer for EOS

BTDR – Brightness Temperature Deflection Ratio

DMSF – Defense Meteorological Satellite Program

EOS – Earth Observing System

GRIP – Genesis and Rapid Intensification Project

GPROF – Goddard PROFiling

HAMSR – High Altitude MMIC Sounding Radiometer

HITRAN – High Resolution TRANsmision

JMR – Jason Microwave Radiometer

JPL – Jet Propulsion Laboratory

KaRIn – Ka band Radar Interferometer

LAS – Lower Atmospheric Sounding

MMIC – Monolithic Microwave Integrated Circuit

NASA – National Aeronautics and Space Administration

NOAA – National Oceanic and Atmospheric Administration

NOMADS – National Operational Model Archive Distribution System

TMI – TOPEX Microwave Imager

TMR – TOPEX Microwave Radiometer

TOPEX – TOPography Experiment

TRMM – Tropical Rainforest Measuring Mission

TPW – Total Precipitable Water

UAV – Unmanned Aerial Vehicle

USA – United States of America

RMS – Root Mean Square

SRSS – Service Records and Retention System

SSMIS – Special Sensor Microwave Imager/Sounder

SWOT – Surface Water and Ocean Topography